



UNIVERSIDAD NACIONAL AUTÓNOMA DE MEXICO
POSGRADO EN CIENCIAS FÍSICAS

**NON-DESTRUCTIVE AND HIGH RESOLUTION IMAGING TECHNIQUES
FOR STUDYING ULTRACOLD QUANTUM GASES**

TESIS
QUE PARA OPTAR POR EL GRADO DE:
MAESTRO EN CIENCIAS (FÍSICA)

PRESENTA:
DIEGO HERNÁNDEZ RAJKOV

DIRECTOR DE INVESTIGACIÓN:
DR. JORGE AMIN SEMAN HARUTINIAN
IF-UNAM

COMITÉ ASESOR:
DR. ASAF PARIS MANDOKI
IF-UNAM
DR. SANTIAGO FRANCISCO CABALLERO BENITEZ
IF-UNAM

CIUDAD UNIVERSITARIA, CD.MX., MAYO, 2021



Universidad Nacional
Autónoma de México

Dirección General de Bibliotecas de la UNAM

Biblioteca Central



UNAM – Dirección General de Bibliotecas
Tesis Digitales
Restricciones de uso

DERECHOS RESERVADOS ©
PROHIBIDA SU REPRODUCCIÓN TOTAL O PARCIAL

Todo el material contenido en esta tesis esta protegido por la Ley Federal del Derecho de Autor (LFDA) de los Estados Unidos Mexicanos (México).

El uso de imágenes, fragmentos de videos, y demás material que sea objeto de protección de los derechos de autor, será exclusivamente para fines educativos e informativos y deberá citar la fuente donde la obtuvo mencionando el autor o autores. Cualquier uso distinto como el lucro, reproducción, edición o modificación, será perseguido y sancionado por el respectivo titular de los Derechos de Autor.

1. Datos del alumno

- Diego Hernández Rajkov
- dhernandezrjk@ciencias.unam.mx

2. Datos del tutor

- Dr. Jorge Amin Seman Harutinian

3. Datos del sinodal 1

- Dr. José Ignacio Jiménez Mier y Terán

4. Datos del sinodal 2

- Dra. Citlali Sánchez Aké

5. Datos del sinodal 3

- Dra. Rocio Jáuregui Renaud

6. Datos del sinodal 4

- Dr. Eduardo Gómez

7. Datos del sinodal 5

- Dr. Jorge Amin Seman Harutinian

Abstract

Este proyecto se centró en la implementación y caracterización de técnicas de imagen destructivas y no destructivas en gases cuánticos ultrafríos de ${}^6\text{Li}$. Implementé un arreglo óptico capaz de obtener imágenes de alta resolución de la nube atómica ($\approx 2\mu\text{m}$), desarrollé las herramientas necesarias para la correcta determinación de las propiedades de las nubes mediante la técnica de imagen por absorción, y establecí un método para obtener las constantes de calibración de esta técnica de imagen.

Además, implementé la técnica de imagen no destructiva conocida como contraste de fase; esta técnica mide la densidad atómica relacionando la fase inducida en el haz de prueba con la densidad de la nube. El sistema óptico es capaz de realizar múltiples imágenes de alta resolución de la misma muestra, lo que permite estudiar las propiedades dinámicas de los gases cuánticos.

Finalmente, para aumentar la calidad de los perfiles de densidad adquiridos, desarrollé un algoritmo capaz de eliminar artefactos de alta frecuencia en las imágenes adquiridas, sin alterar la distribución del perfil de densidad y aumentando la señal a ruido.

This project is centered on the experimental implementation and characterization of both destructive and non-destructive imaging techniques for ultracold quantum gases of ${}^6\text{Li}$. I developed a new optical setup capable of imaging the atoms with high-resolution ($\approx 2\mu\text{m}$). I developed the tools necessary for the correct determination of the cloud properties using absorption imaging. I established a method to obtain the calibration constants along both imaging axes.

Additionally, I implemented the non-destructive phase-contrast imaging technique. This technique measures the atomic density by connecting the induced phase on the probe beam to the cloud's density. The optical system is suitable for performing multiple high-resolution images of the same atomic sample, allowing studying the dynamic properties of quantum gases.

Finally, to further increase the quality of the acquired density profiles, I developed an algorithm capable of removing high-frequency artifacts from the images without altering the density profile. Hence, increasing the signal-to-noise ratio a factor of two.

Contents

Abstract	II
Agradecimientos	IV
1. Introduction	2
2. Theory of ultracold atoms	5
2.1. Ideal quantum gases in a harmonic trap	5
2.2. Interacting quantum gases	7
2.2.1. Tuning the interaction: Feshbach Resonances	8
2.2.2. The BEC-BCS crossover	9
2.3. Lithium in the presence of magnetic fields	11
3. Experimental Setup and Procedure	15
3.1. Experimental setup	15
3.1.1. Ultra-high vacuum system	15
3.1.2. Laser system	16
3.1.3. Science chamber	21
3.2. Imaging setup	22
3.2.1. Imaging AOM setup	22
3.2.2. Horizontal imaging setup	25
3.2.3. Vertical high-resolution imaging setup	26
3.2.4. Imaging resolution	32
3.3. Cooling to degeneracy	32
3.3.1. Optical cooling	34
3.3.2. The optical-magnetic potential	36
4. Imaging procedure and calibration	41
4.1. Semi-classical light-matter interaction	41

4.2. Absorption imaging technique	45
4.2.1. Optical density calculation	46
4.2.2. Low Intensity approximation	47
4.2.3. High intensity regime	49
4.3. Image quality enhancement	59
4.3.1. Focusing using shadowgraphy	59
4.3.2. Post-processing: Fringe Removal Algorithm	63
4.4. Phase contrast imaging	67
4.4.1. Imaging the phase	68
4.4.2. Large phase distortions	75
4.4.3. How non-destructive is this imaging technique?	76
5. Conclusions and perspective	80
5.1. Conclusions	80
5.2. Future perspectives	81
A. ${}^6\text{Li}$ D-lines properties	86
Bibliography	87

Agradecimientos

A Luza, quien desde el inicio me apoyó a lo largo de, por aguantarme todo este tiempo y por darme las ganas de seguir adelante sin importar que se presente. You're my person.

A mi familia.

A Jorge Seman, a quien agradezco profundamente por darme la oportunidad de trabajar con él. Ha sido, y seguirá siendo una gran experiencia trabajar con alguien tan entusiasmado por la ciencia.

A Giacomo Roati, por sus grandes aportaciones al laboratorio, que jugaron un papel muy importante en el desarrollo de este trabajo.

A mis compañeros de laboratorio Jackson, Eduardo y Andrés. A Carlos, Rodrigo, Maira principales encargados del área de electrónica, y a quienes se han requerido de manera recurrente en el laboratorio.

El desarrollo de esta tesis ha sido financiado por diferentes proyectos de investigación:

- Beca de maestría por parte de CONACyT del programa 000306 - MAESTRÍA EN CIENCIAS FÍSICA
- Los siguientes proyectos de DGAPA-PAPIIT (UNAM):
 - IA101716, IN111516, IN107014, IN103818 IN109021 y IN109619
- Los siguientes proyectos del Instituto de Física (UNAM): PIIF-8 and PIIF-9.
- Apoyo de la Coordinación de la Investigación Científica (CIC-UNAM) No. LANMAC-2019.
- Los siguientes proyectos de CONACyT
 - Redes Temáticas "Tecnología Cuántica".
 - Ciencia Básica grants 255573, 254942 y A1-S-39242
 - CIC-UNAM y CONACyT, a través del programa de Laboratorios Nacionales: LN232652, LN260704, LN271322, LN280181, LN293471 y LN299057.
 - CONACyT - 314860, "Mantenimiento de infraestructura del Laboratorio Nacional de Materia Cuántica: Materia Ultrafría e Información Cuántica"

Chapter 1

Introduction

Weakly interacting Bose-Einstein condensates and strongly interacting Fermi systems have been realized experimentally in ultracold gases for more than two decades [1, 2]. This kind of experiment allowed the creation of a new paradigm for studying condensed matter systems. Indeed, both theoretical and experimental effort has brought a deep understanding of the physics underlying complex systems and phenomena such as high T_c -superconductivity and superfluidity [1, 3]. Even today, fundamental aspects of the topic are still under active research.

Throughout the two decades of research in the area, there have been multiple improvements in the imaging methods [2]. The most relevant one being the use of CCD cameras instead of single fluorescence detectors. The basis of these imaging techniques relies on the interaction between light and matter. Various imaging techniques depend on distinct atomic responses, the most common being the absorption signal [2], accompanied by the induced phase shift on the probe beam [2, 4-6]. The most used and simple technique to implement is the resonant one, known as absorption imaging.

Resonant imaging can be classified into two categories depending on the probe's intensity [7, 8]. The low-intensity regime is more robust since it requires the least number of calibration parameters, at most one. This feature allows for a high signal-to-noise ratio in low magnification setups when dealing with atomic clouds with relatively low optical densities. However, this imaging technique is useless for high magnification setups due to the low signal registered into the CCD sensors. Additionally, the absorption signal saturates for high-density samples, causing distortion effects on the density profiles. Solving this issue requires increasing the probe's intensity, entering the high-intensity regime. In this regime, the number of calibration

parameters increases [7, 8], making it more susceptible to calibration errors.

The absorption imaging technique is most convenient wherever static properties are needed to be measured. Nevertheless, it is still possible to extract dynamic properties using absorption imaging. Though, the number of experimental runs required increases significantly. Such measurements are time-consuming and susceptible to run-to-run fluctuations and drifts in the experimental apparatus, causing a higher dispersion in the data. This problem appears because this type of imaging technique destroys the sample after probing. One way to overcome this problem is to use a non-destructive imaging techniques [2]. This type of imaging has the advantage that reduces the heating induced by the probe beam employing non-resonant light [5].

Non-destructive imaging techniques are becoming more commonly used in recent years [5, 6, 9, 10]. These techniques allowed a close examination of the superfluid transition [6] and the propagation of excitations in the gas by measuring the same sample at various times [10–13]. These techniques can be separated into groups depending on the measured effect. Dispersive imaging techniques measure the phase shift in the probe beam caused by the atomic index of refraction, for instance, phase-contrast [13], diffraction contrast [14], and holographic imaging [10]. Polarization-dependent methods measure the Faraday rotation on the probe polarization as a function of the gas density [5, 9]. Partial-transfer absorption imaging consists of transferring a small fraction of the gas into a different state and imaging it using absorption imaging [15, 16].

In this context, the Laboratory for Ultracold Matter at UNAM (LMU) aims to produce and study diverse superfluid phenomena in strongly correlated Fermi gases [17]. This kind of system is of particular interest due to its complexity to describe theoretically, and a complete theory still needs to be developed [1, 3]. A central aspect of these systems is the possibility to explore very distinct interacting regimes depending on the gas inter-atomic interactions. If the inter-atomic interactions are attractive, it is possible to form a gas of Cooper-like pairs described by the Bardeen-Cooper-Schrieffer (BCS) theory. On the contrary, if the inter-atomic interactions are repulsive, it is possible to create tightly bound pairs of atoms having bosonic statistics. In this interaction regime, the system can undergo a phase transition into a Bose-Einstein condensate (BEC) of molecules [1, 3]. Ultracold atom experiments offer the possibility to explore a whole range of interaction regimes employing Feshbach resonances. In particular, it is possible to continuously change the system's interaction

traversing the so-called BEC-BCS crossover. Notably, the LMU works with gases of fermionic lithium. This specific isotope of lithium has the advantage of having a broad and experimentally accessible magnetic Feshbach resonance [18], allowing studying diverse superfluid phenomena in these strongly correlated systems [19–21].

In this thesis, we aimed to implement a high-resolution, high-magnification imaging setup capable of acquiring images using both absorption and phase-contrast imaging. In this approach, we first focus on the implementation of the high-magnification imaging setup. Next, we thoroughly characterized the high-intensity absorption imaging regime. Alongside the characterization, we developed an algorithm capable of improving the signal-to-noise ratio of the measured density profiles. Lastly, we focused on the implementation of the phase-contrast imaging technique, enabling us to further study the dynamic properties of multiple collective modes.

Chapter 2

Theory of ultracold atoms

In this chapter, I will discuss the concept of interacting atomic gases. In particular, I'll start describing the density distribution of a trapped ideal Fermi gas in the quantum degenerate regime. Then, I'll consider the case of interacting particles analyzing the two-body scattering problem. In ultracold quantum gases, the scattering properties can be manipulated using magnetic Feshbach resonances, allowing the study of different interacting regimes, particularly the BEC-BCS crossover. Finally, I will discuss the atomic properties of lithium in the presence of magnetic fields.

2.1. Ideal quantum gases in a harmonic trap

In ultracold quantum gas experiments, trapping potentials confine the gases spatially. In most cases, as in ours, the trapping potential can be approximated as harmonic near their minimum [3]:

$$V(x, y, z) = \frac{1}{2}m (\omega_x^2 x^2 + \omega_y^2 y^2 + \omega_z^2 z^2), \quad (2.1)$$

where m is the mass of the atoms being confined, and ω_i the trap frequencies along the i 'th direction. For now, we'll consider the system as ideal, meaning the particles does not interact with each other. When the thermal energy, $k_B T$, is larger than the harmonic potential energy levels, $\hbar\omega_i$, the occupation probability of the state with position \mathbf{r} , and momentum \mathbf{p} is given by [3]:

$$f(\mathbf{r}, \mathbf{p}) = \frac{1}{e^{(p^2/2m+V(\mathbf{r})-\mu)/k_B T} \pm 1}, \quad (2.2)$$

where $p^2 = \mathbf{p} \cdot \mathbf{p}$, μ is the chemical potential, and $V(\mathbf{r})$ is the external potential, in our case the harmonic one. The \pm sign corresponds to the quantum statistic distributions. For fermions, the sign is positive leading to the Fermi-Dirac distribution, while negative for bosons leading to the Bose-Einstein distribution. Integrating (2.2) in momentum space, we obtain the density distribution [3]:

$$n(\mathbf{r}) = \frac{1}{(2\pi\hbar)^3} \int f(\mathbf{r}, \mathbf{p}) d\mathbf{p} = \mp \frac{1}{\lambda_{DB}^3} \text{Li}_{3/2}(\mp e^{(\mu-V(\mathbf{r}))/k_B T}), \quad (2.3)$$

where $\text{Li}_{3/2}(z)$ is the polylogarithmic function of order 3/2, defined as:

$$\text{Li}_\nu(z) = \sum_{k=1}^{\infty} \frac{z^k}{k^\nu}. \quad (2.4)$$

In the high-temperature regime, the effects of the particles statistics become negligible, recovering the classical limit. In this limit, the density distribution can be approximated as a gaussian function of the form:

$$n_{cl}(\mathbf{r}) = \frac{N}{\pi^{3/2} \sigma_x \sigma_y \sigma_z} e^{-\sum_i \left(\frac{x_i}{\sigma_i}\right)^2}, \quad (2.5)$$

where $\sigma_i = \frac{2k_B T}{m\omega_i}$ for $i = x, y, z$, and N the total number of atoms in the gas.

In the low-temperature regime, the quantum effects dominate. In this regime, the density distribution for bosons and fermions have very distinct profiles. Fermions repel from each other due to the Pauli exclusion principle. For bosons, this Pauli repulsion doesn't exist leading to a more compressed density profile. For fermions in the zero temperature limit, the states with energy less than the Fermi energy, E_F , are occupied, while the rest are not. In this limit, the Fermi-Dirac distribution becomes:

$$f(\mathbf{r}, \mathbf{p}) = \begin{cases} 1 & \text{if } p^2/2m + V(\mathbf{r}) < E_F \\ 0 & \text{if } p^2/2m + V(\mathbf{r}) > E_F. \end{cases} \quad (2.6)$$

At $T = 0$, the chemical potential coincides with the Fermi energy. Using the harmonic potential, the density distribution in the zero temperature limit is [3]:

$$n_\sigma(\mathbf{r}) = \frac{8}{\pi} \frac{N_\sigma}{R_{F_x} R_{F_y} R_{F_z}} \left\{ \max \left[0, 1 - \sum_i \left(\frac{x_i}{R_{F_{x_i}}} \right)^2 \right] \right\}^{3/2}, \quad (2.7)$$

with $R_{F_{x_i}} = \sqrt{2E_F^{ho}/m\omega_i^2}$ are the Fermi radii, N_σ is the number of atoms in the σ spin component, and $\bar{\omega} = (\omega_x\omega_y\omega_z)^{1/3}$ the geometrical average trap frequency. For finite temperatures, the density profiles can be calculated using (2.3). Qualitatively the profiles changes smoothly from the gaussian distribution to the Thomas-Fermi limit (2.7). To calculate the Fermi energy, we integrate both in space and momentum the Fermi-Dirac distribution at $T = 0$ [3]:

$$N_\sigma = \frac{1}{(2\pi\hbar)^3} \int \int f(\mathbf{r}, \mathbf{p}) d\mathbf{p} d\mathbf{r} = \int_0^{E_F} \frac{g(\epsilon) d\epsilon}{e^{(\epsilon-\mu)/k_B T} + 1}, \quad (2.8)$$

where $g(\epsilon)$ is the density of states. For the harmonic potential $g^{ho}(\epsilon) = \epsilon^2/2(\hbar\bar{\omega})^3$. Therefore,

$$N_\sigma = \frac{1}{2(\hbar\bar{\omega})^3} \int_0^{E_F^{ho}} \epsilon^2 d\epsilon \rightarrow E_F^{ho} = \hbar\bar{\omega}(6N_\sigma)^{1/3} \quad (2.9)$$

Besides the Fermi energy, it is convenient to define the Fermi temperature, $T_F = E_F/k_B$, and the Fermi momentum, $k_F = \sqrt{2mE_F/\hbar^2}$.

2.2. Interacting quantum gases

For dilute gases, the many-body interactions are precisely described by a small number of parameters [3, 22]. Those parameters emerge from the two-body collision analysis. In the regime of low temperatures and long mean interparticle distance, the system scattering properties are considerably simpler.

The analysis of the two-body scattering process requires solving the Schrödinger equation in the relative coordinates system. A crucial step when solving this problem is to expand the solution into partial waves with different angular momenta. Higher angular momenta components correspond to higher energy states. Hence, in the low temperature and low energy regime, the scattering processes are essentially described by the $l = 0$ (s-wave) and $l = 1$ (p-wave) angular momenta components. An additional constraint we need to contemplate is the antisymmetry of the wave function for identical fermions. The wave function antisymmetric nature implies that identical fermions don't interact through s-wave scattering but through p-wave scattering. For sufficiently low temperatures, scattering through p-wave is suppressed for identical fermions [23], producing an almost ideal single-component Fermi gas. For this reason,

we'll consider the problem of a mixture of fermions with two spin components. In this case, the scattering between the same spin component is suppressed, while the scattering among distinct spin components isn't. In fact, for different spin components, the interaction is characterized by the s-wave scattering properties, in particular, the s-wave scattering length [24].

2.2.1. Tuning the interaction: Feshbach Resonances

In addition to the two spin mixture, we need to consider the atom's internal structure. Due to the hyperfine coupling interaction, the collision process drastically changes, giving rise to the so-called Feshbach resonance [24, 25]. The presence of these resonances allows us to manipulate the s-wave scattering length employing an external magnetic field (figure 2.1b). Feshbach resonances can be exploited to tune from attractive to repulsive, from weak to strongly interacting regimes. Notably, lithium has the broadest Feshbach resonances, making it the most used species to explore these interaction regimes [24].

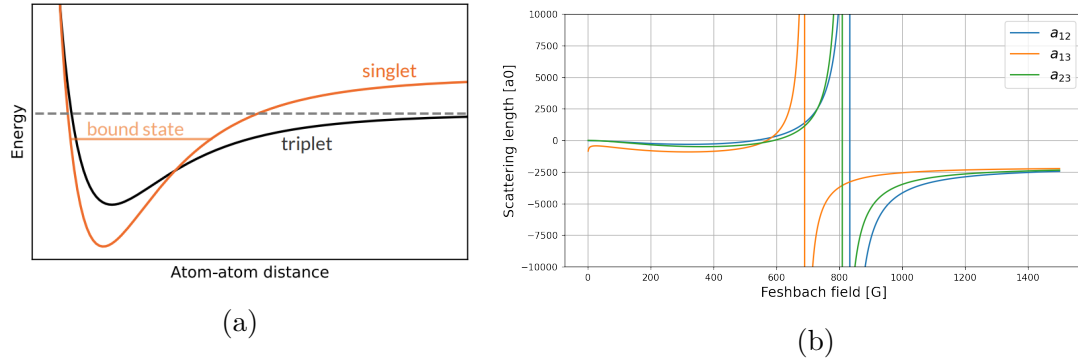


Figure 2.1: a) Triplet (open channel) and singlet (closed channel) scattering potential for two colliding atoms. The singlet scattering potential energy can be shifted by applying a bias magnetic field. The Feshbach resonance occurs when the bound state energy coincides with the collision energy (dashed line). b) Feshbach resonances between the three lowest hyperfine states of ${}^6\text{Li}$, see figure 2.4.

For single valence electrons atoms, the Feshbach resonance requires the presence of two different scattering potentials or channels, known as open and closed channels. In this case, the singlet and triplet configuration of the electron spin (see figure 2.1a). These potentials are coupled by the hyperfine interaction [25]. Consequently, the energy separation between both potentials can be manipulated employing an external

bias magnetic field (because of their different magnetic moments).

Whenever the closed channel has a bound state close to the collision energy (corresponding to the open channel energy) the coupling between both channels becomes significantly greater [25]. Indeed, the crossing of the closed channel bound state and the collision's energy gives rise to a Feshbach resonance. Close to the Feshbach resonance, the scattering length is well approximated by [26]:

$$a_s(B) = a_{bg} \left(1 - \frac{\Delta}{B - B_0} \right), \quad (2.10)$$

where Δ is the magnetic resonance width, B_0 is the magnetic field where the crossing occurs (the center of the resonance), and a_{bg} is the off-resonance background scattering length. The Feshbach resonances between the three lowest hyperfine states of ${}^6\text{Li}$ are shown in Figure 2.1b. These resonances have an extremely large width ($\Delta \approx 300\text{G}$ [18]) compared with other atomic species [24].

2.2.2. The BEC-BCS crossover

The possibility of changing the inter-atomic interaction by varying an external bias magnetic field makes ultracold atoms the perfect system for studying multiple many-body physics such as superfluidity and high-Tc superconductors [1, 2, 26]. Moreover, the BEC-BCS crossover allows the possibility of tuning the underlying quantum statistics. From the BEC side, having bosonic statistics to the BCS side with fermionic statistics.

To describe the distinct interaction regimes, it is essential to parametrize the interaction coupling within the system using a single parameter. The two main parameters describing the interaction strength are the system's density and the s-wave scattering length. With these parameters, it is possible to construct the dimensionless parameter $1/k_F a_s$, where k_F is the density-dependent Fermi momentum, and a_s the s-wave scattering length.

For temperatures below the Fermi temperature, it is possible to distinguish between three distinct regimes:

- $1/k_F a_s \gg 1$: In this regime, atoms with different spin states can couple together and form tightly bound molecules. The system behaves like a bosonic one and can undergo a phase transition into a Bose-Einstein condensate (BEC) when

the temperature is below the critical temperature.

- $1/k_F a_s > 1$: In this regime, atoms with different spin states can couple together and form bound molecules. The system can undergo a phase transition into a BEC when the temperature is below the critical temperature. However, quantum depletion effects modify the behavior of the condensed fraction as a function of the temperature [26].
- $1/k_F a_s \ll -1$: In this regime, the atoms form long-range Cooper pairs-like described by the Bardeen-Cooper-Schrieffer (BCS) theory. In principle, the system can undergo a superfluid transition when the temperature is below the critical temperature. In this regime, the Cooper pairs have a characteristic size larger than the inter-particle spacing of the gas.
- $-1 < 1/k_F a_s < 1$: This regime is known as the BEC-BCS crossover, meaning it's an intermediate regime between BEC and BCS. Like the BCS regime, it is characterized by the formation of Cooper pairs but the Cooper pair size is comparable with the inter-particle spacing.

A more complex representation of the different phases of the BCS to BEC crossover is shown in figure 2.2 [26].

One of the main differences between all the regimes is the superfluid critical temperature shown in figure 2.2 as the line delimiting the yellow region. On the BEC side, the critical temperature tends to the one of a gas of molecules with twice the atomic mass. On the BCS side, the critical temperature decreases exponentially with $1/k_F |a_s|$.

In this work, we'll mainly focus on the BEC side of the resonance. The main reason being the cloud's density. As previously mentioned, at low temperatures, the bosonic gas density is always higher than that of a fermionic gas. This is exemplified in section 3.3.2, particularly in figure 3.20. The higher the density is, the higher the distortion effects of the imaging techniques, especially in the absorption imaging technique, see section 4.2.

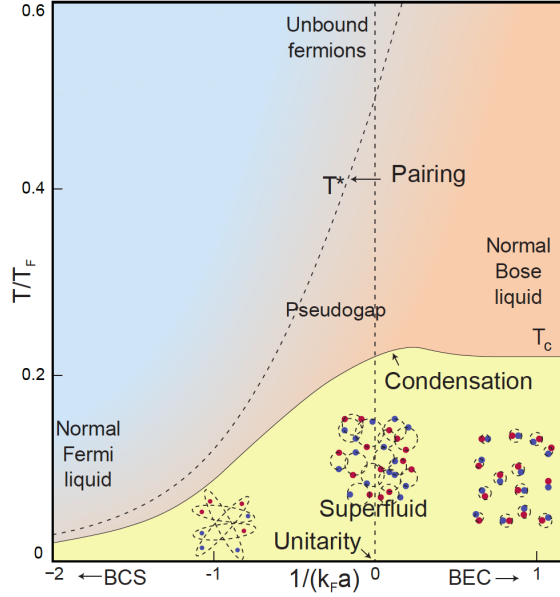


Figure 2.2: Qualitative phase diagram of the BCS to BEC crossover [27] as a function of the temperature T/T_F and the dimensionless coupling $1/k_F a_s$. Figure from [26].

2.3. Lithium in the presence of magnetic fields

The fermionic isotope of lithium has in its ground state, $2^2S_{1/2}$, a single valence electron with total angular momentum $\hat{J} = \hat{L} + \hat{S} = 0 + 1/2 = 1/2$. The first two excited states corresponds to the $2^2P_{1/2}$ and $2^2P_{3/2}$ states, with $\hat{J} = 1/2$ and $\hat{J} = 3/2$ respectively. The optical transitions between the $2^2S_{1/2}$ state to the $2^2P_{1/2}$ and $2^2P_{3/2}$ states are respectively known as D1 and D2. Figure 2.3 sketches the fine structure of the ${}^6\text{Li}$ atom, along with the relevant optical transitions [28].

To model the effect of both the hyperfine splitting and the external magnetic we'll consider the following hamiltonian [29]:

$$H = H_0 + H_{HF} + H_B = H_0 + A\mathbf{I} \cdot \mathbf{J} - (\mu_B g_J \mathbf{J} + \mu_N g_I \mathbf{I}) \cdot \mathbf{B}, \quad (2.11)$$

where H_0 describe the fine structure hamiltonian of an atom, H_{FH} the hyperfine hamiltonian, and H_B the magnetic interaction hamiltonian. The constants g_J and g_I are the electronic and nuclear Landé factors respectively. Table 2.1 shows the specific values of the Landé g-factors for the different electronic and nuclear states of fermionic lithium. The hyperfine structure of the atom is describe by the total angular

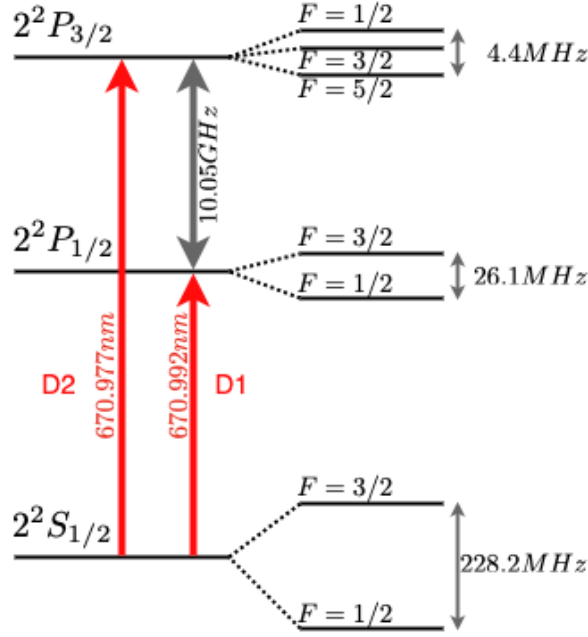


Figure 2.3: ${}^6\text{Li}$ fine and hyperfine structure at zero external magnetic field. The two relevant optical transitions used in the experiment are the D1 and D2 lines. Both optical transitions have the same linewidth $\Gamma = 2\pi \times 5.87$ MHz [28]. Note that the fine splitting of the $2^2P_{3/2}$ level is lower than the transition linewidth.

momentum of the outermost electron \mathbf{J} and the nuclear spin \mathbf{I} . The hyperfine shift as a function of the external magnetic field is given by [29]:

$$\frac{1}{\hbar}\Delta E = a\mathbf{I} \cdot \mathbf{J} - \frac{1}{\hbar}(\mu_B g_J \mathbf{J} + \mu_N g_I \mathbf{I}) \cdot \mathbf{B}, \quad (2.12)$$

where a is the hyperfine constant expressed in units of Hz. Considering a constant bias magnetic field of the form $\mathbf{B} = B_z \hat{z}$, then the energy shift is given by:

Symbol	Value	a [MHz]
g_I	-0.0004476540	
$g_J(2^2S_{1/2})$	2.0023010	152.1368407
$g_J(2^2P_{1/2})$	0.6668	17.4
$g_J(2^2P_{3/2})$	1.335	-1.1

Table 2.1: Landé factors for ${}^6\text{Li}$ [28].

$$\frac{1}{\hbar}\Delta E = aI_z J_z + \frac{a}{2}(J_+ I_- + J_- I_+) + \left(\frac{\mu_B g_J}{\hbar} J_z + \frac{\mu_N g_I}{\hbar} I_z\right) B_z, \quad (2.13)$$

where J_{\pm} are the raising and lowering operators respectively. The hamiltonian contri-

bution shown in (2.13) can be solved analytically for $J = 1/2$, known as the Breit-Rabi solution. The energy splitting is given by [29, 30]:

$$\frac{1}{h}\Delta E_{F=I\pm\frac{1}{2}} = -\frac{(I+1/2)}{2(2I+1)}a + \frac{\mu_N g_I m_F B}{h} \pm \frac{(I+1/2)}{2}a\sqrt{1 + \frac{2m_F}{I+1/2}x + x^2}, \quad (2.14)$$

where $x = \left(\frac{\mu_B g_J - \mu_N g_I}{ah(I+1/2)}\right) B$. For the $J \neq 1/2$ the solution to (2.13) must be obtained numerically. Figure 2.4 show the energy shifts of the $2^2S_{1/2}$, $2^2P_{1/2}$ and $2^2P_{3/2}$ states of ${}^6\text{Li}$ as a function of the external magnetic field.

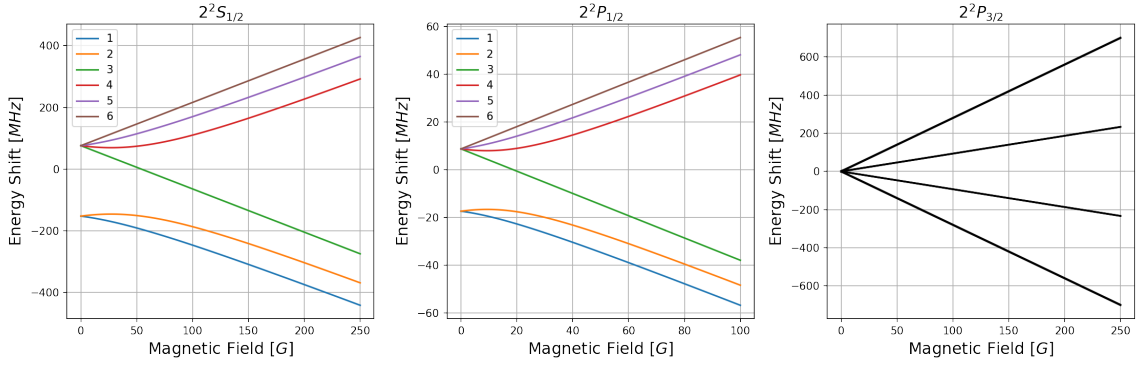


Figure 2.4: Hyperfine splitting as a function of the external magnetic field for the states $2^2S_{1/2}$, $2^2P_{1/2}$ and $2^2P_{3/2}$ of ${}^6\text{Li}$. For the former two states, we use the Breit-Rabi formula (2.14), meanwhile for the state $2^2P_{3/2}$ we must solve numerically (2.13).

At zero external magnetic field, the ground state $2^2S_{1/2}$ splits in two hyperfine levels: $|2^2S_{1/2}, F = 1/2\rangle$ and $|2^2S_{1/2}, F = 3/2\rangle$ separated by 228.2 MHz. The state $2^2P_{3/2}$ hyperfine splitting is unresolved, meaning the separation between the states with $F = 1/2$ and $F = 5/2$ is less than the transition natural linewidth, as shown in Figure 2.3.

For low magnetic fields ($B \lesssim 30$ G for ${}^6\text{Li}$) the Zeeman effect is a weak perturbation to the hyperfine structure, producing the expected linear Zeeman effect. In this regime, the description using the $|F, m_F\rangle$ is still valid. For higher magnetic fields, this is not the case [29]. At higher fields, the Zeeman effect dominates over the hyperfine structure, causing the electron and nuclear spin to decouple. This regime is also known as the Paschen-Back regime. In this regime, the F description is no longer valid requiring the electronic and nuclear spin projections, m_J and m_I , to describe the states correctly. In the Paschen-Back regime, the hyperfine splitting between states

with the same m_J quantum number remains almost constant, as shown in figure 2.4. This is key for the implementation of optical and radio-frequency transitions between these states.

Chapter 3

Experimental Setup and Procedure

In this chapter, we present the ultra-high vacuum system and the optical setup for cooling and trapping an atomic cloud of ${}^6\text{Li}$. Additionally, we describe the imaging setup we implemented to image the atoms across different interaction regimes. Finally, we describe the experimental procedure for the production of such ultracold quantum gases.

3.1. Experimental setup

In this section, we will outline the experimental setup for the production of ultracold quantum gases. We will describe the vacuum and laser system for optically cooling the atoms.

3.1.1. Ultra-high vacuum system

The vacuum system, sketched in figure 3.1, consists of an oven, a differential pumping stage, a Zeeman slower, and the science chamber where all experiments are performed [17]. Inside the oven, there is a 50/50 mixture of enriched samples of ${}^6\text{Li}$ and ${}^7\text{Li}$, although, for the rest of this thesis, we will focus only on the fermionic isotope: ${}^6\text{Li}$. The oven is heated to 450°C to produce sufficient vapor pressure inside the vacuum system to generate an atomic beam that is later collimated using a 4 mm diameter nozzle and by a copper cold finger [31]. The atomic beam then passes through the differential pumping stage, consisting of two narrow aligned tubes separated by 25 mm from each other. The differential pumping stage is designed to

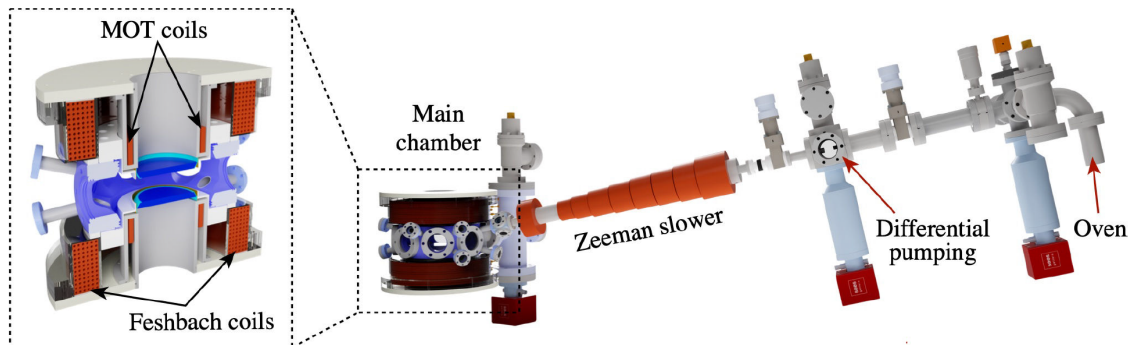


Figure 3.1: Sketch of the Ultra-High vacuum system, image taken from [17].

keep a pressure difference between the oven and the science chamber to up to five orders of magnitude. In this way, the pressure in the main chamber always remains below 10^{-11} Torr while the oven pressure varies from below 10^{-11} Torr when the oven is below 100°C (overnight or standby mode) to 10^{-9} Torr when the oven is at a temperature of 450°C (actively running the experiment).

After the atomic beam passes through the differential pumping stage, it enters the Zeeman slower. In this section, the atoms are decelerated from velocities in the order of 960 m/s down to velocities below 60 m/s [32]. Finally, the *slow* atomic beam enters the science chamber, where they are confined in a magneto-optical trap (MOT) and further cooled to degeneracy see section 3.3 for more details.

3.1.2. Laser system

Two different laser systems are required for the production and study of ultracold atoms: the first one is for laser cooling and imaging the atoms using light close to the D optical transitions, while the second one is to create a trapping potential using light very far detuned from any transition.

Laser cooling system

The optical transitions involved in the laser cooling stage are the D1 and D2 transitions of ${}^6\text{Li}$, see figure 3.2a. The D2 line is used for standard Doppler-limited laser cooling techniques, while the D1 is needed to achieve sub-Doppler temperatures [33], see section 3.3 for more details.

For the standard laser cooling techniques using the D2 transition, we use the

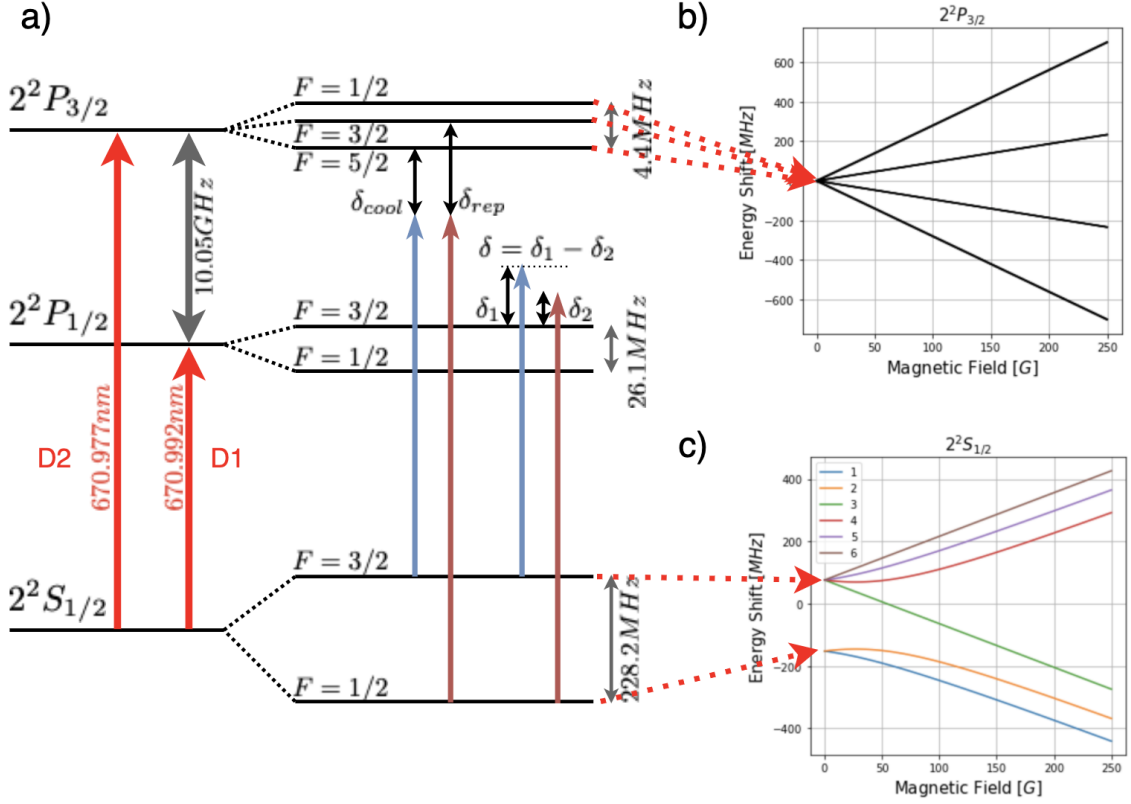


Figure 3.2: a) Hyperfine structure of ${}^6\text{Li}$, showing the D2 and D1 transitions at zero external magnetic field. b) and c) Hyperfine splitting in the presence of a external magnetic field of the $2^2P_{3/2}$ and $2^2S_{1/2}$ respectively.

$2^2S_{1/2} F = 3/2 \rightarrow 2^2P_{3/2} F = 5/2$ transition as the cooling transition while the $2^2S_{1/2} F = 1/2 \rightarrow 2^2P_{3/2} F = 3/2$ transition as the repumper transition. The frequency difference between both transitions is approximately the hyperfine splitting of the $2^2S_{1/2}$ manifold, about 228.2 MHz. Since the frequency difference is small, it is possible to create both frequencies from a unique laser source and a combination of acousto-optic modulators (AOM's), see figure 3.4.

To generate the D2 frequencies, we use an extended cavity diode laser in cat-eye configuration¹, from which we obtain 30 mW of power. The linewidth of this laser is below 100 kHz, well beneath the natural linewidth of the D2 transition (5.8 MHz). The laser output is divided into two beams: one going to the saturated absorption spectroscopy (SAS) setup to stabilize and lock the laser frequency using an atomic reference (see figure 3.3b). The other beam is amplified ten times by a Tapered

¹Model CEL002 from MOGLabs.

Amplifier (TA)² and further split into two beams using a 50:50 beam splitter. These beams will then become the cooling and repumper transitions after controlling their frequency using two AOM's in a double-pass configuration. Next, the two beams are amplified by a TA and later recombined using a 50:50 beam splitter. In this way, we produce two beams with both frequencies. These beams will serve first as the light for the MOT beams, and the other as Zeeman slower and imaging light. The details of the laser setup can be found in [17, 33] and in figure 3.4 (The imaging AOM's system will be detailed in section 3.2).

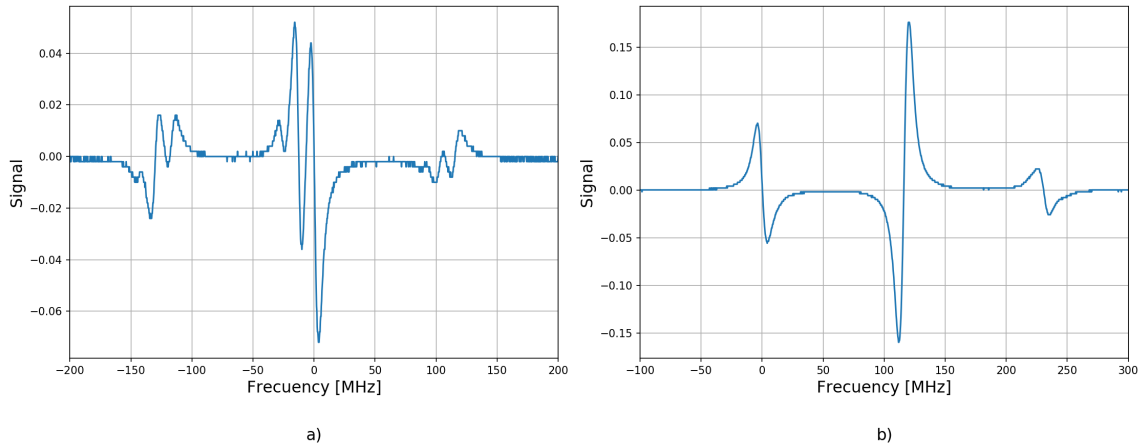


Figure 3.3: Saturated absorption spectroscopy error signal of the a) D1 and b) D2 transitions, the zero frequency is the locking position of the lasers.

To generate the D1 frequencies, we use a second extended cavity diode laser in cat-eye configuration, the same model as the D2 laser source. Just as in the case of the D2, the laser is locked to an atomic reference using a SAS scheme see figure 3.3a. To implement the D1 sub-Doppler cooling stage, we require two frequencies: $2^2S_{1/2} F = 3/2 \rightarrow 2^2P_{1/2} F = 3/2$ and $2^2S_{1/2} F = 3/2 \rightarrow 2^2P_{1/2} F = 3/2$, see figure 3.2, separated by the hyperfine splitting of the $2^2S_{1/2}$ manifold, about 228.2 MHz, same as for the D2 frequencies. For this reason, before the first TA amplification stage of the D2, we mix both the D2 and D1 lasers beams using a polarizing beam splitter. This setup allows us to use the same laser system already in place for the D2 frequencies to generate the required D1 frequencies.

²Model MOA002 from MOGLabs.

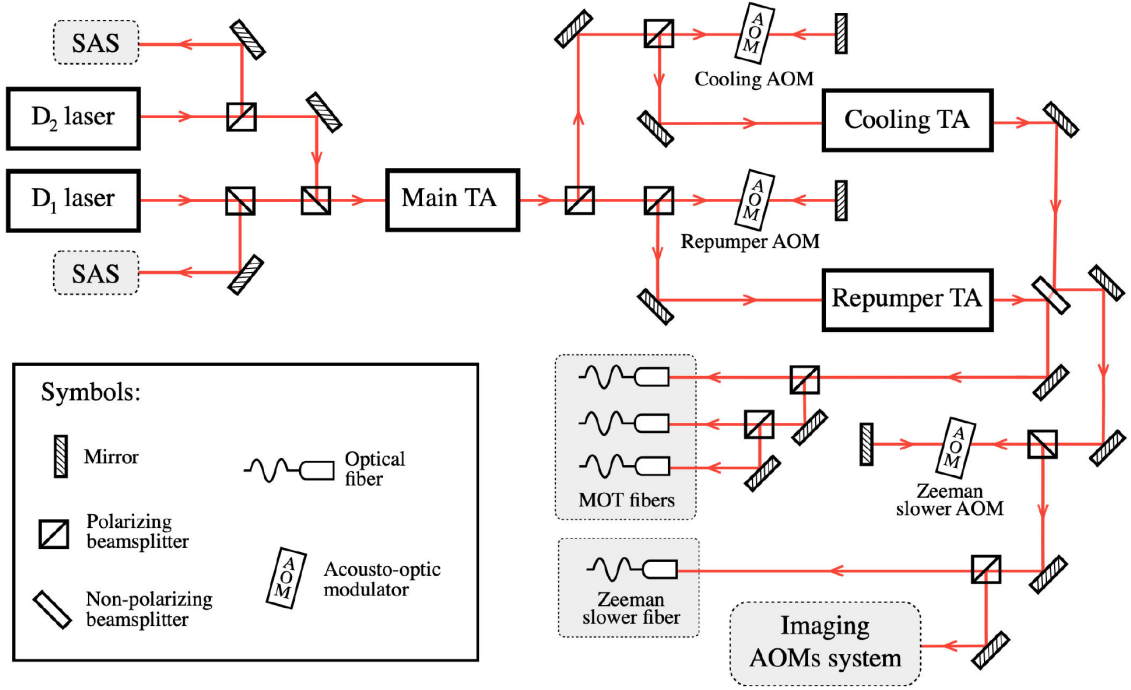


Figure 3.4: Simplified scheme of the laser cooling setup showing the main features of the system, taken from [17].

Optical Dipole Trap

We employ a high power infrared beam to generate the conservative optical potential. The infrared beam originates from a 1070 nm multi-mode ytterbium fiber laser from IPG Photonics, with a maximum power output of 200 W. We control the laser power arriving at the science chamber in two different ways. First, from 170 to 10 W, we control it by changing the power output of the IPG laser itself. For lower intensities, we control the efficiency of the diffracted order of an AOM, see figure 3.5. This last method allows us to stabilize the power arriving at the science chamber via a PID feedback loop. The efficiency of the AOM is regulated using a PID controller³. The reference setpoint is fixed by an external analog signal coming from our control system, while the measured value is obtained from the signal of a photo-diode measuring the light from a transmission leak of a mirror in the laser path, see figure 3.5.

In addition to controlling the laser power arriving at the science chamber, we can dynamically modify the laser cross-section using a particular input signal to the RF-

³Model SRS SIM960.

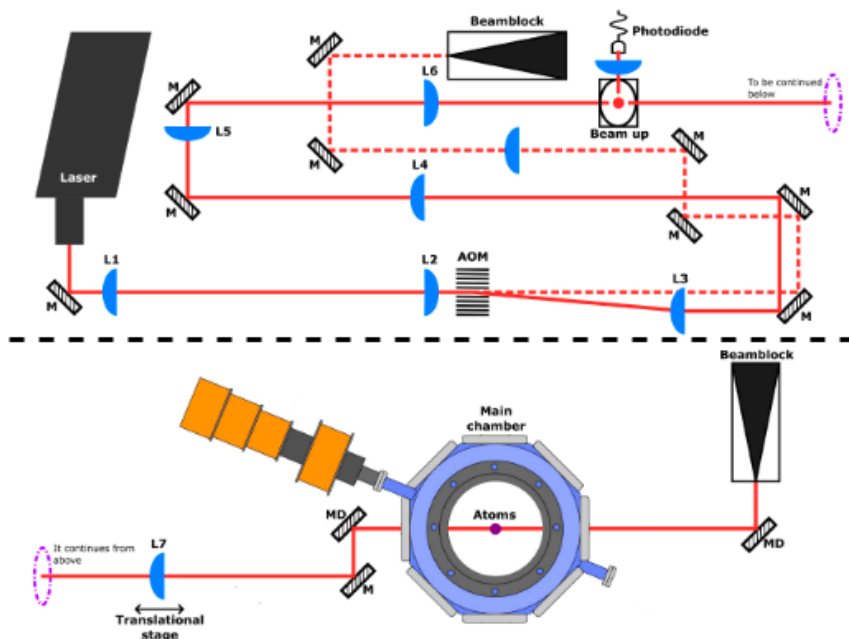


Figure 3.5: Detailed ODT laser setup. The upper section shows the required setup to generate the ODT beam with the required power and shape. After the AOM, the 0th order is denoted by a dashed line while the first order by a continuous line. The beam up shown is necessary to adjust the height of the ODT beam. The lower section shows its arrangement in the science chamber. Image taken from [34].

frequency channel of the AOM. In this way, we can change the potential's transverse position and shape, as shown in figure 3.6a. For more details about the ODT setup implementation see [34, 35].

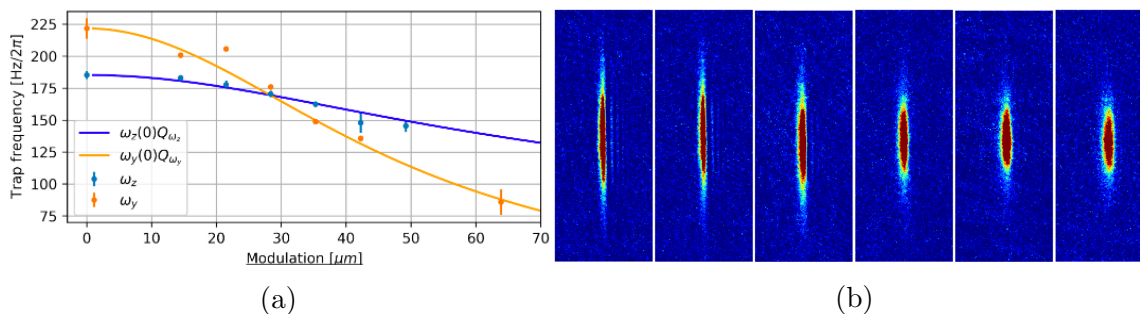


Figure 3.6: a) ODT beam waists as a function of the beam's modulation amplitude. b) Effect of increasing (from left to right) the ODT beam waist on the atomic cloud. Images taken from [34].

3.1.3. Science chamber

The science chamber is a custom-made octagonal stainless-steel cell from Kimball Physics [31]. As sketched in figure 3.7a, along its vertical axis it has two large re-entrant view-ports providing proximity to the sample, therefore, granting the opportunity for a high-resolution imaging system, see section 3.2.

Two sets of coils are mounted around the science chamber, the MOT coils, and the Feshbach coils, see figure 3.7a. The MOT coils consist of two small sets of coils of 6×4 windings connected in anti-Helmholtz configuration and produce a quadrupole magnetic field whose gradient around the chamber's center can be adjusted from 0 to 45.3 G/cm [33]. The Feshbach coils consist of two sets of coils of 12×6 windings connected in quasi-Helmholtz configuration and produces at the center an essentially constant vertical magnetic field varying from 0 up to 1000 G. The deviation from the Helmholtz configuration was chosen to create a slight curvature in the magnetic field at the center of the chamber. This curvature will let us confine the ultracold atoms into a conservative hybrid optical-magnetic trap, as discussed in section 3.3.

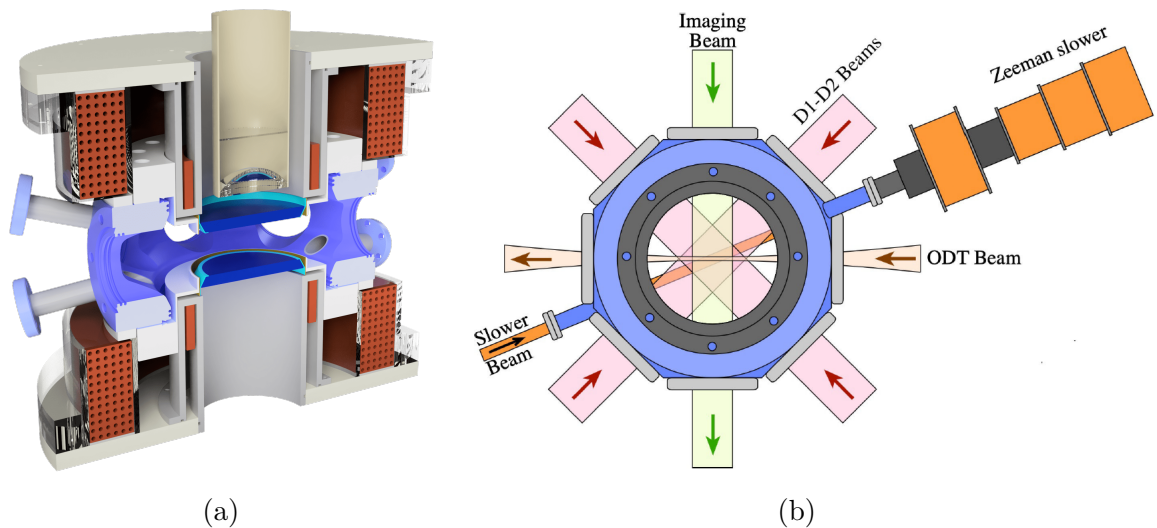


Figure 3.7: a) Cross-section sketch of the science chamber. b) Principal optical beams across the science chamber view from above.

Figure 3.7b sketches the principal optical beams arrangement around the science chamber in the horizontal direction: the two MOT beams, an imaging beam, and the ODT. We omitted the vertical direction beams for clarity reasons but shown in figure 3.11c.

3.2. Imaging setup

In this section, we will outline the experimental setup implemented for acquiring images of the atomic clouds. We start by describing the imaging AOM setup necessary to compensate for the Zeeman shift of the atomic resonant frequency for different magnetic fields ranging from 0 to 1000 G. Then, we describe the two different imaging setups we use in the experiment. First, we describe the imaging setup along the horizontal axis of the science chamber. This imaging system was employed to analyze the different cooling stages from the MOT and optical molasses using low magnification while following the evaporation process using a magnified setup. Finally, we describe the high-resolution and high magnification setup along the vertical axis.

3.2.1. Imaging AOM setup

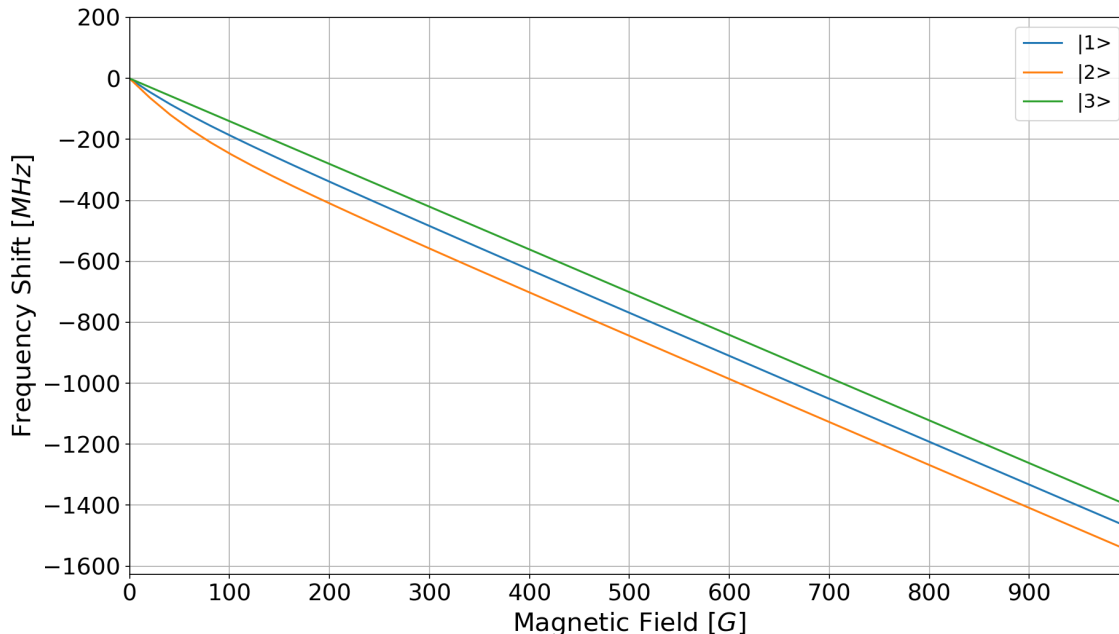


Figure 3.8: Frequency shift of the transitions $|1\rangle$, $|2\rangle$ and $|3\rangle$ to the excited state in $m_{J'} = -3/2$ of the state $2^2P_{3/2}$.

The atomic resonance frequency of a given transition, in this case, the D2 transition, depends on the external magnetic field due to Zeeman induced shifts in both the ground state and the excited state. In particular, during all the experimental sequences, we'll work with different hyperfine ground states: $|1\rangle$, $|2\rangle$ and $|3\rangle$, see figure 3.2b and c, but only one excited state for the imaging process: the $m_{J'} = -3/2$

branch of the $2^2P_{3/2}$ (The energy difference between the excited states is small, a few MHz, compared to the transition shift of the whole branch, $10^2 - 10^3$ MHz).

To drive the imaging transition at a magnetic field, we need to determine the frequency shift of the transition. This is achieved by taking the difference between the ground and excited Zeeman shifts as:

$$\begin{aligned}\Delta_g(B) &= \nu_B^g - \nu_0^g, \\ \Delta_e(B) &= \nu_B^e - \nu_0^e, \\ \Delta_{eff}(B) &= \Delta_e(B) - \Delta_g(B),\end{aligned}\tag{3.1}$$

where ν_B^g (ν_B^e) describes the energy of the ground (excited) state at a given magnetic field B , see section 2.3, and $\Delta_{eff}(B)$ is the effective frequency shift of the D2 transition shown in figure 3.8 for all three ground states. These values are large compared to the operating frequencies of a single AOM. For this reason, we need to distribute the whole range of frequencies shifts into several sections controlled by different AOM configurations. Such AOM setup is sketched in figure 3.9.

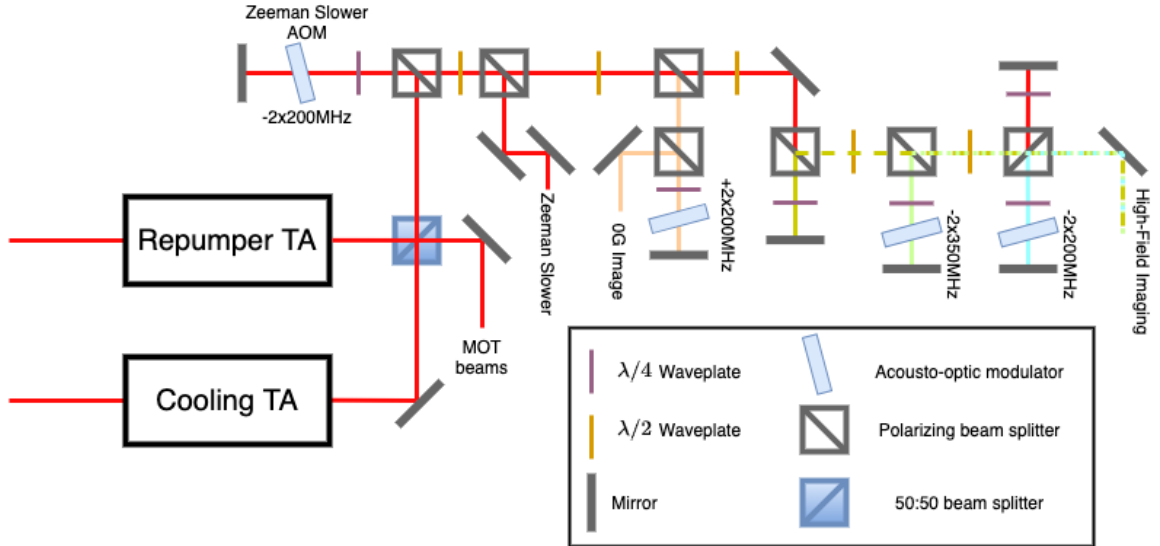


Figure 3.9: Simplified scheme of the imaging AOM setup.

The AOM setup is split into three sections allowing imaging in five different magnetic field intervals:

- The first imaging interval corresponds to zero external magnetic field (or low intensity fields up to 50 G): this imaging interval uses one 200 MHz AOM

in double-pass configuration to compensate for the Zeeman slower light shift, creating an effective zero frequency shift. Orange path in figure 3.9

- The second interval corresponds to magnetic fields ranging from 200 up to 400 G is reached without changing the light frequency arriving at the imaging setup, already shifted -400 ± 20 MHz. Yellow path in figure 3.9.
- The third interval corresponds to values around 520 G, which corresponds to the Feshbach resonance zero-crossing. To image in that range, we need to increase the frequency shift using a 200 MHz AOM in double-pass configuration, creating an effective frequency shift of -800 ± 50 MHz. Blue path in figure 3.9.
- The fourth interval corresponds to magnetic field from 650 to 890 G, corresponding to the BEC-BCS crossover. To image in this region, we need to increase the frequency shift using a single 350 MHz AOM in double-pass configuration, creating an effective frequency shift of -1100 ± 50 MHz. Green path in figure 3.9.
- Finally, for higher magnetic fields around 1000 G, we need to combine both the 200 MHz AOM and the 350 MHz AOM already mentioned: both in double-pass configuration to increase the frequency shift of -1500 ± 100 MHz. Combining the green and blue paths from figure 3.9.

The AOM setup allows us to select the imaging interval by changing the orientation of the $\lambda/2$ wave plates along the optical path, see figure 3.9. In this way, we can direct the imaging beam to the corresponding AOMs and optical fibers to generate the desired frequency shift. This setup allows us to probe the atoms in presence of magnetic fields ranging from 200 G to 1000 G. and near the vicinity of zero external magnetic field.

To drive the imaging transition in the presence of a constant external magnetic field, we need to match both the transition frequency and the light's polarization. Along the vertical direction, the light must have σ^- polarization to drive the imaging transition. While along the horizontal axis, the light must have linear polarization orthogonal to the magnetic field. The only inconvenience for imaging along the horizontal direction is that the atom-photon cross-section is half its value along the vertical axis, reducing the atomic signal, see section 4.2.

3.2.2. Horizontal imaging setup

To image along the horizontal axis, we implemented a two telescope system with magnifications ≈ 0.37 and ≈ 2.11 , see figure 3.10. Both telescopes use the same first lens, with focal length $f_1 = 200\text{mm}$, located at a focal distance from the center of the science chamber. Then, to select among the two imaging systems, we place a flipping mirror to change the optical path, either passing through the second lens of the telescope of focal lengths $f_2 = 75\text{mm}$ or $f_3 = 400\text{mm}$. Finally, the probe beam arrives at the CCD camera, model Manta from Allied Vision Technologies.

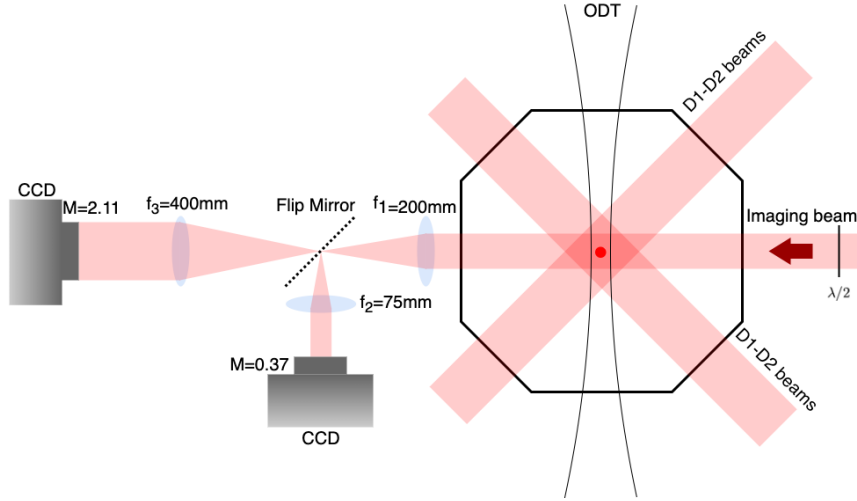


Figure 3.10: Simplified scheme of the horizontal imaging setup around the science chamber.

The probe's light frequency originates from the imaging AOM setup, and its value depends on the magnetic field region we are interested in. The imaging light's polarization is fixed to be orthogonal to the magnetic field. Along this imaging axis, the scattering cross-section of the atoms is reduced by a factor of two because only half of the light can drive the transition, see section 4.2. Linear polarization orthogonal to the magnetic field can be expressed as a linear combination of σ^- and σ^+ polarization in the atoms frame of reference. Only the σ^- component drives the transition to the $m_J = -3/2$ excited state, while the σ^+ component is so far detuned from the $m_J = 1/2$ excited state that does not interact with the atomic cloud. Although the optical density is reduced, this imaging setup is crucial since it allows us to follow the different stages of the cooling process from the ODT transfer to the formation of a degenerate gas, see section 3.3.

3.2.3. Vertical high-resolution imaging setup

The high resolution and high magnification vertical imaging setup is different from the horizontal imaging setup for multiple reasons, the main reason being its proximity to the atomic sample. The main aspheric lens⁴ of the microscope objective has an effective focal length of 32mm, in contrast to the horizontal setup where the first lens is located 200mm from the sample. The proximity to the sample lets us have a high numerical aperture (NA), which is key to access higher resolutions. Another difference is the depth of field (DOF) of the imaging setup. A shorter focal length with higher NA implies a shorter DOF, $DOF \approx \lambda \frac{\sqrt{1-NA^2}}{NA^2}$ [36]. Hence we require higher control during the alignment process of this imaging setup.

Design and mounting of the objective

The design of the objective is inspired by the one at LENS [37]. This design considers the experimental requirements concerning the different laser beams necessary for cooling, imaging, and controlling the atomic sample along the vertical axis: we need two MOT light beams, an imaging beam, and the possibility to add a green laser beam to tailor repulsive optical potentials.

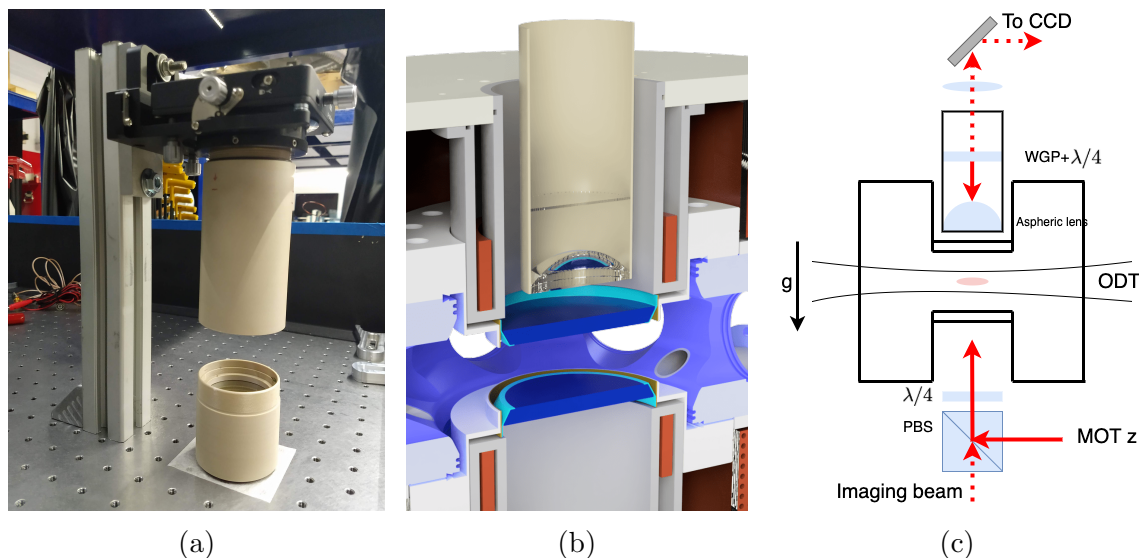


Figure 3.11: a) Photography of the mounted objective. b) Cross-section sketch of the science chamber and the objective. c) Simplified scheme of the vertical imaging setup.

⁴Model AL4532-A of Thorlabs.

In Figures 3.11b and 3.11c, we depict the objective's placement as well as a sketch of the laser beams involved along the vertical direction. Before arriving at the science chamber, the MOT z and imaging beams are mixed into a polarizing beam splitter and sent through the bottom vertical re-entrant window. After passing the chamber, both beams are separated using a combination of $\lambda/4$ wave plate and a wire-grid polarizer (WGP). This combination allows us to retro-reflect the MOT beam while transmitting the imaging beam since they have orthogonal polarization. Nonetheless, both beams pass through the aspheric lens and nearly focused on the $\lambda/4$ wave plate and WGP. We cannot place the optics exactly at the effective focal length of the aspheric lens because of the damage threshold of the WGP. This misalignment causes the retro-reflected MOT z beam to be slightly diverging. However, this does not significantly affect the MOT loading stage.

To retro-reflect the MOT beam, while transmitting the imaging beam, we need to fix the orientation of the WGP with respect to the $\lambda/4$ wave plate. To accomplish this, we minimize the transmission of the MOT z beam through the optical setup. Once at the lowest intensity, we fix both elements using retaining rings located inside the optical tube, see the bottom tube in figure 3.11a. To check the setup's efficiency, we verify that the imaging beam passes through with almost no power reduction. This section is screwed into an extension tube shown in figure 3.11a. To precisely position the aspheric lens, the optical tube is mounted into a five-axis translational stage: XYZ translation, tilt along XZ and YZ planes, as shown in figure 3.11a.

Magnification calibration

To complete the vertical telescope, we use the second lens of focal length $f = 250$ mm located outside of the optical tube holding the aspheric lens. We added a second 1 : 1 telescope to extend the imaging setup, as shown in figure 3.12a. This extension lets us use the Andor Fast Kinetic Series acquisition mode, as we will discuss later. Additionally, this setup allows us to implement the non-destructive imaging technique we are interested in: phase-contrast imaging, see section 4.4.

The sequence of lenses focal lengths are $f_1 = 32$ mm, $f_2 = 250$ mm, forming the first telescope, and $f_3 = 150$ mm and $f_4 = 150$ mm forming the second one, as shown in figure 3.12a. With these sequence we estimate the final theoretical magnification of the optical system to be $M_{teo} = \left(\frac{250}{32}\right) \left(\frac{150}{150}\right) \approx 7.8$. However, it is preferable to measure the truth magnification of the imaging system.

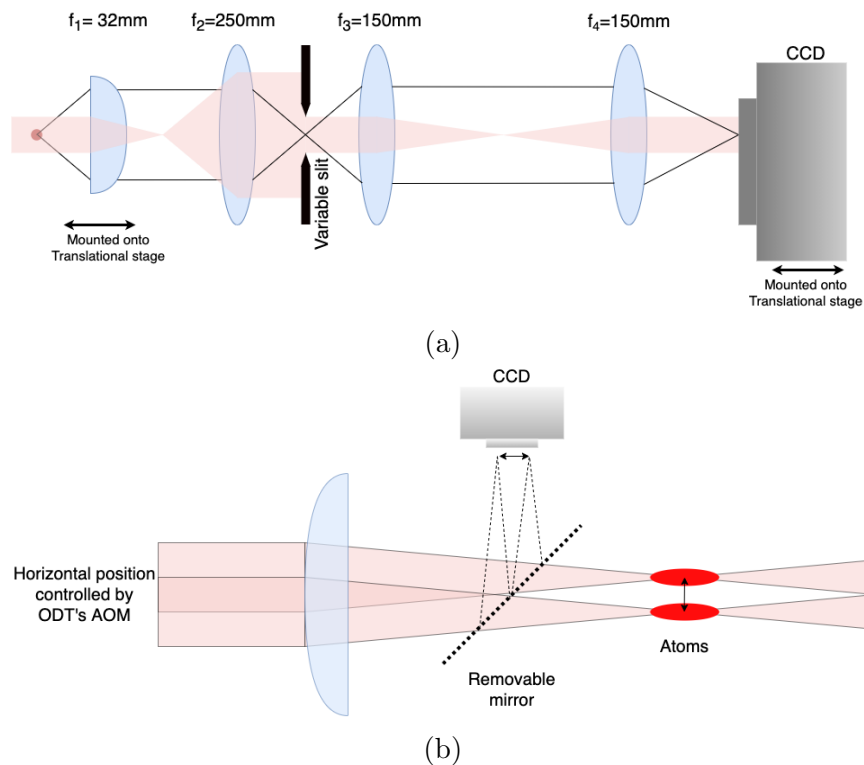


Figure 3.12: a) Simplified scheme of the vertical imaging setup around the science chamber. b) Sketch of the magnification measurement along the vertical imaging setup.

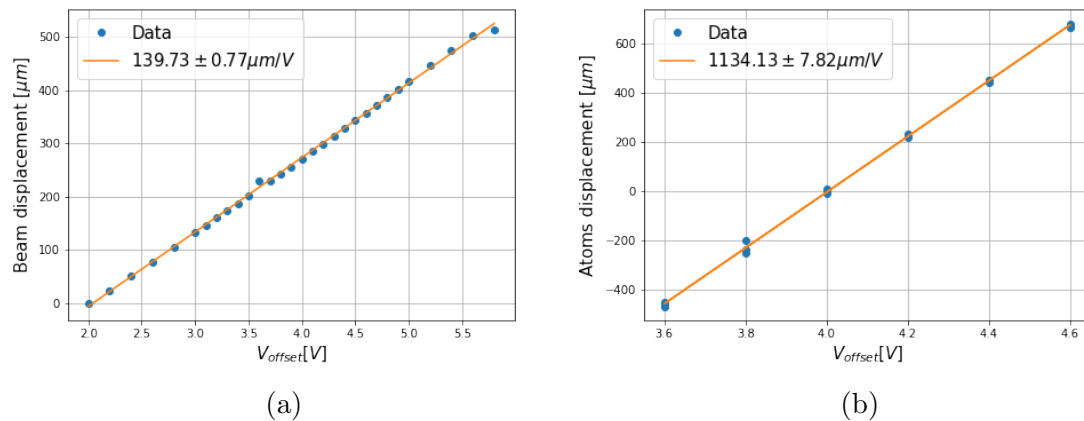


Figure 3.13: a) ODT beam and b) atom's center of mass positions as a function of the RF-frequency input voltage of the AOM. The ratio between the measured displacements determines the magnification of the imaging setup: $M \approx 8.12 \pm 0.01$. The errorbars are smaller than the data symbol.

To measure the magnification of the imaging setup, we use the fact that we can control the cloud's position by displacing the trapping potential by a known amount. In our case, the cloud's location is at the ODT focus, section 1. We can change the ODT focus using the AOM in the ODT setup, section 3.1.2, through the RF-frequency input voltage of the AOM.

To precisely determine the displacement of the cloud's position, we calibrated the displacement of the ODT beam focus as a function of the RF-frequency. Using a removable mirror placed in front of the last lens of the ODT setup, we deflected and focused the beam into a CCD camera, figure 3.12b. Then, we recorded the ODT's focus transverse position as a function of the RF-frequency input voltage of the AOM, figure 3.13a. Using a linear fit to the data, we measured displacement to be $139.7 \pm 0.8 \mu\text{m}/V_{RF}$.

Later, we repeated the measurement removing the mirror and imaging the atom's position. We measured the cloud's center of mass displacement as a function of the RF-frequency input voltage of the AOM, as shown in figure 3.13b. Using a linear fit to the data, we measured the displacement to be $1134 \pm 8 \mu\text{m}/V_{RF}$. Ultimately, the magnification factor of our imaging system is $M = \frac{1134 \pm 8}{139.7 \pm 0.8} \approx 8.12 \pm 0.01$. This result is consistent with the theoretical value $M_{teo} \approx 7.8$. The difference between both values comes from the lenses separation, not being exactly $f_1 + f_2$.

Andor and Fast Kinetic Series

The principal imaging technique we are going to use is absorption imaging, section 4.2. For this type of imaging, it is crucial to have a short time between the multiple acquired images. These image are: an image of probe beam after interacting with the atoms, an image of the beam itself, lastly, an image of the background noise level. To see further details go to section section 4.2. The delay time between acquisitions must be short related to the time scale of power fluctuations in the probe's beam and of any form of mechanical vibration of the experimental setup. It is crucial to consider this to avoid the formation of fringe-like patterns during the optical density calculation, section 4.3.2. These fringe-like patterns arise from small position shift or intensity variations of objects in the first and second images. However, we can reduce the fringes effect by applying a fringe removal algorithm as discussed in section 4.3.2.

In practice, the most severe limitation in the time delay is the repetition rate of the CCD camera. For example, along the horizontal setup, the Manta CCD takes

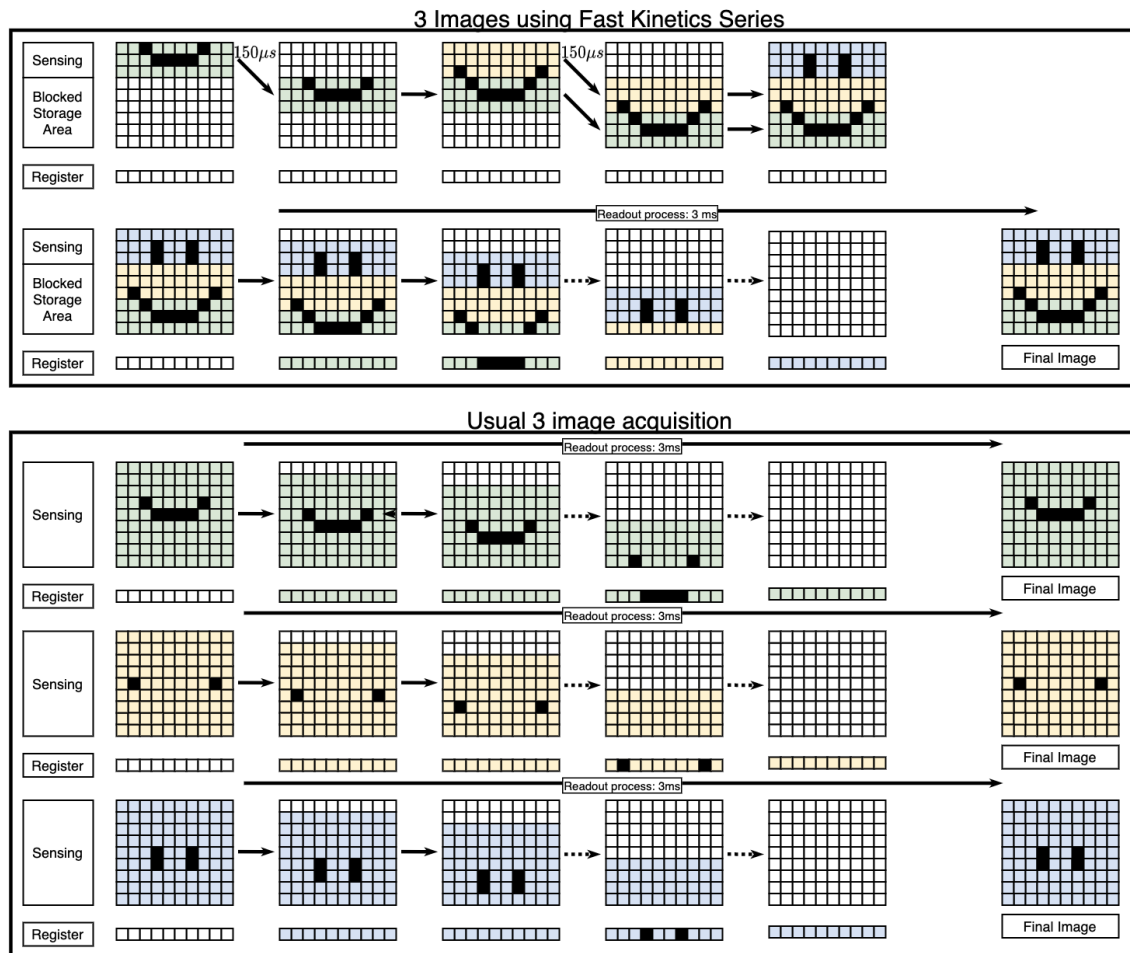


Figure 3.14: Comparison between the FKS acquisition mode (top) and the usual acquisition mode (bottom). The FKS mode uses part of the sensor as storage while the rest is used to the actual acquisition. After the first acquisition, the sensor pixels are shifted vertically to the storage area leaving the sensing area exposed for the next acquisition. Once the full sensor is used, the "slow" readout process begins reading one row at a time. For the usual acquisition mode the readout process must be repeated for each image, making the time delay between images longer than with the FKS mode.

around 150 ms to read a full 1388×1038 pixel image. In contrast, along the vertical axis we use an Andor EMCCD camera, model Andor iXon Ultra 888. To read a full 1024×1024 pixel image of the Andor takes around 50 ms. This time is too long for the experimental requirements since frequencies above 10 Hz may induce fringe-like patterns in the optical density. However, the Andor camera provides a simple solution to this problem using a Frame Transfer mode called Fast Kinetic Series (FSK) [38]. This acquisition mode allows us to decrease the time delay between images at the

expense of the final image pixel height.

Figure 3.14, shows the FKS acquisition mode working principle. This technique uses only a small section of the EMCCD sensor for the actual acquisition while using the remaining area as storage. After exposing the acquisition area, the EMCCD shift the image to the storage area, leaving the acquisition area ready to be exposed again. The process repeats until the entire sensor is exposed, and finally, the last reading process transfers the data to the computer. The method's advantage is that shifting a row of pixels vertically is very fast, a few μs . In our case, we can fix the vertical readout speed to 4.3, 2.2, 1.13, or 0.6 $\mu\text{s}/\text{vertical pixel}$, although, we set it to 2.2 $\mu\text{s}/\text{vertical pixel}$ to reduce counting errors in the final image; using a height of 255 pixels then the overall vertical readout time is 561 μs . By contrast, both the horizontal shift and the readout time are the slowest steps of the readout process, leading the 50ms repetition cycle. This technique reduces the time delay between images by at least a factor of 100. Figure 3.15 sketches the absorption imaging procedure employing the FKS acquisition mode. The first image acquired corresponds to the atom's absorption with the probe beam, the second being only the probe beam, and finally, the last one is the background noise level.

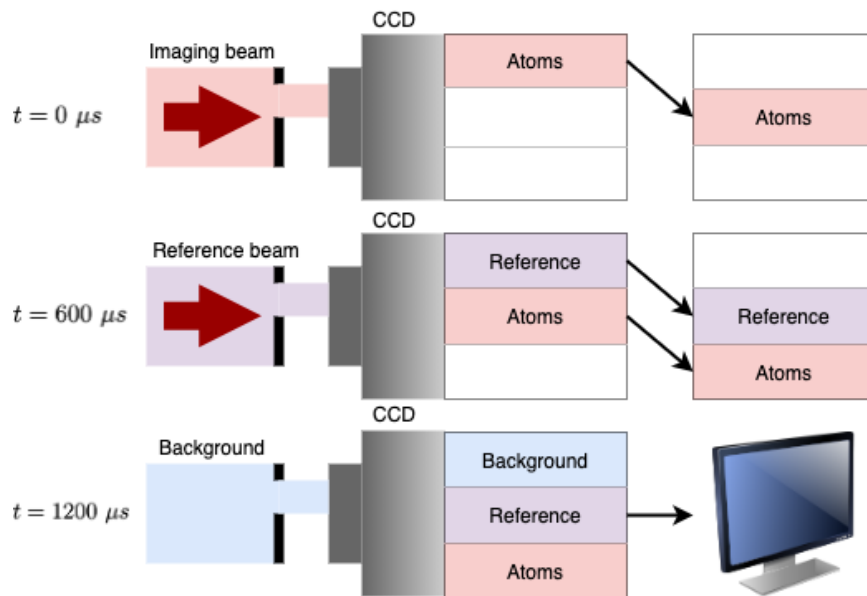


Figure 3.15: Using the FKS mode applied to absorption imaging: the first image corresponds to the atoms absorption signal with the probe beam, the second being only the probe beam, and finally, the last section is the background noise level.

The downside to this technique is that we need to cover the storage area of the

CCD physically because the full CCD sensor is still active and could accumulate undesired counts. To solve this problem, we placed a 3 mm slit in the atom's focal plane, see figure 3.12a. In principle, we could position the slit right in front of the CCD sensor. However, diffraction effects from the slit may introduce distortion effects in the acquired image. Placing the slit far from the CCD sensor reduces these effects significantly.

3.2.4. Imaging resolution

A crude estimation of our imaging system's resolution can be performed using the Rayleigh resolution criterion. This limit considers the diffraction limit of the aspheric lens, which collects the imaging beam after the vacuum chamber, see figure 3.11b. The minimum resolvable separation is the radius of the Airy disc pattern given by [36]:

$$\delta = \frac{0.61\lambda}{\text{NA}}, \quad (3.2)$$

where λ is the wavelength of the imaging light and NA the numerical aperture of the imaging setup. The lens we employ is a plano-convex lens with a NA of ≈ 0.61 . Then the theoretical resolution would be $\delta \approx 670\text{nm}$. In practice, one should consider various defects arising from the imaging beam's finite size, and more significantly, misalignment and optical aberrations. In comparison, with the objective at LENS, they were able to measure the resolution for a similar objective setup and estimated their resolution to be $\delta \approx 1.5\mu\text{m}$ [37]. We estimate to have a resolution comparable to the LENS experiment of $\delta \approx 2\mu\text{m}$.

3.3. Cooling to degeneracy

In this section, we will outline the experimental sequence followed for the production of a degenerate quantum gas of ${}^6\text{Li}$. The techniques involved in the cooling process start with the slowdown of an atomic beam in the Zeeman Slower, see [17, 33]. The next stage consists of trapping the atoms in a magneto-optical trap. Next, to reduce the cloud's temperature, close to the Doppler limit, we apply the standard optical molasses. To further cool the cloud, we use a gray molasses stage to achieve sub-Doppler temperatures. This step transfers most of the atoms into the $F = 1/2$

state. Later, we confine them into a conservative potential consisting of a single-beam ODT. There, we perform runaway evaporative cooling to reach the quantum degenerate regime. Finally, by changing the atom's interaction through the Feshbach resonance, we can form a molecular Bose-Einstein condensate (mBEC) of tightly bound atoms, a strongly interacting Fermi gas (UFG), or a Bardeen-Cooper-Schiffer (BCS) gas of loosely Cooper-pairs-like states [17].

The magneto-optical trap (MOT) is the first stage towards quantum degeneracy. At this stage, we confine the atoms arriving from the Zeeman slower. The MOT consists of two main elements [29]: the first one being three retro-reflected intersecting orthogonal pairs of laser beams in $\sigma^+ - \sigma^-$ polarization configuration, secondly, a magnetic field gradient along with the three orthogonal directions, such that at the intersection of the retro-reflected beams there is a zero magnetic field. Generating such a field is straight forward using a pair of coils in the anti-Helmholtz configuration.

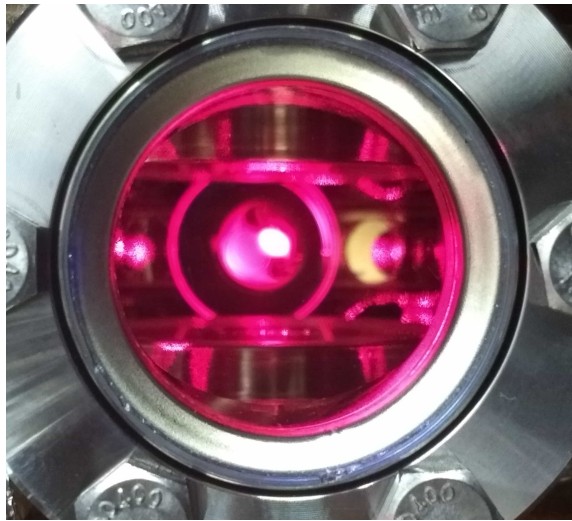


Figure 3.16: Photography of a lithium MOT, viewing via one of the science chamber's viewports.

The laser beam configuration is necessary to cool the atoms through the standard optical cooling techniques, meaning that the atoms are confined in momentum-space but not in physical space. The magnetic field gradient is required to capture the atoms spatially, introducing a spatial Zeeman shift dependence. The Zeeman shift produces an additional detuning, making it more likely to scatter photons further within the trapping region. The gradient of the number of scattered photons generates a net attractive force towards the zero magnetic field region. Farther from the trap's center, the Zeeman shift causes a reduction of the number of scattered photons, canceling

the attractive force and delimiting the trapping region.

The interaction between a two-level system and the magneto-optical configuration just described is modeled using a semi-classical approach [29, 30]. The total force is expressed as:

$$\vec{F}_{total} = \frac{\hbar k s_0}{2} \left(\frac{16\delta_0(kv + \frac{\Delta\mu bz}{\hbar})/\Gamma}{(1+s_0)^2 + \frac{8}{\Gamma^2}(1+s_0)(\delta_0^2 - (k + \frac{\Delta\mu bz}{\hbar})^2) + \frac{16}{\Gamma^4}(\delta_0^2 + (kv + \frac{\Delta\mu bz}{\hbar})^2)^2} \right). \quad (3.3)$$

Taking the limit close to the center of the trap ($|\frac{\Delta\mu bz}{\hbar}| \ll \Gamma$), and for small velocities ($|kv| \ll \Gamma$), then the total force on the atoms is:

$$\vec{F}_{total} \approx 4\hbar k s_0 \left(\frac{2\delta_0/\Gamma}{(1+s_0)^2 + 8(1+s_0)(\delta_0/\Gamma)^2 + 16(\delta_0/\Gamma)^4} \right) \left(k\vec{v} + \frac{\Delta\mu b}{\hbar}\vec{z} \right). \quad (3.4)$$

This expression can be simplify as $F_{tot}^{\vec{v}} = -\alpha\vec{v} - \beta\vec{z}$, where $\beta = \frac{\Delta\mu b}{\hbar k}\alpha$, and with

$$\alpha = \frac{\hbar k^2 s_0}{2} \left(\frac{16|\delta_0|/\Gamma}{(1+s_0)^2 + 8(1+s_0)(\delta_0/\Gamma)^2 + 16(\delta_0/\Gamma)^4} \right). \quad (3.5)$$

Usually, the equation (3.5) is written in the low intensity approximation, *i.e.* $s_0 = I/I_{sat} \ll 1$:

$$\alpha = 4\hbar k^2 s_0 \left(\frac{2|\delta_0|/\Gamma}{(1+(2\delta_0/\Gamma)^2)^2} \right). \quad (3.6)$$

A more detailed description of this model, including the experimental optimization of the optical cooling stages described in this section, can be found in [29, 30, 33].

3.3.1. Optical cooling

Briefly, we will describe the optical cooling stages. We perform the MOT using the D2 cooling and repumper transitions described in section 3.1.2. After the MOT's loading, we can capture about $N = 5 \times 10^9$ atoms at a temperature of $T = 7\text{mK}$ [17]. At this point, the cloud's temperature is 50 times higher than the Doppler limit. This limit is the lowest attainable temperature using the optical cooling techniques, $T_D^{\text{Li}} = 141\mu\text{K}$ for lithium.

For this reason, we perform a second cooling stage. We turn off any magnetic field present in the experiment, and we reduce the intensity and the detuning of both cooling and the repumper lights, bringing them closer to resonance. In these conditions, we reach $N = 6 \times 10^8$ atoms at a temperature of $T = 500 \mu\text{K}$ [17], close to the Doppler limit, see figure 3.17a.

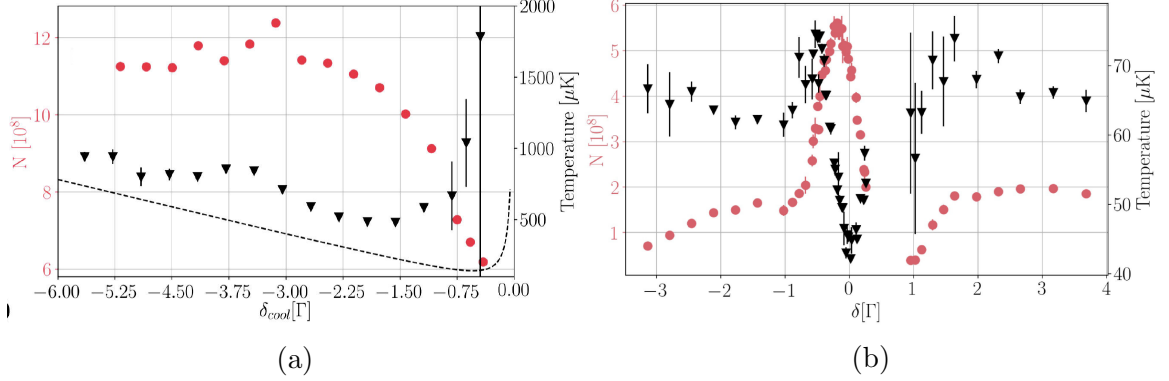


Figure 3.17: Number of atoms (red circles) and temperature (black triangles) of a) the D2 optical molasses as a function of the cooling detuning; and b) the D1 gray molasses as a function of the relative detuning between cooling and repumper. The dashed line in a) corresponds to the Doppler limited temperature as a function of the detuning. Images from [17].

To further decrease the cloud's temperature, we can no longer use the D2 optical transition. Instead, we perform a gray molasses scheme using the D1 transition [39]. This cooling mechanism is modeled by the interaction of a three-level system in Λ configuration, with two semi-classical electromagnetic (EM) fields, see figure 3.2. In particular, it combines two different phenomena: Sisyphus cooling and Velocity Selective Coherent Population Trapping (VSCPT). Briefly, the Hamiltonian of the Λ configuration with the coherent EM-fields has two eigenstates, conveniently called bright and dark states, where only the bright state interacts with the light fields [39, 40]. The cooling process occurs when the atoms in the bright state (with higher potential energy) are transferred to a lower energy dark state, similar to the Sisyphus cooling mechanism. The cooling cycle repeats due to the non zero probability of transferring a dark state into a bright one. The key point is that probability depends on the square of the atom's momentum. Consequently, there is an accumulation of slower atoms in the dark state. This cooling mechanism is therefore said to be velocity selective. This mechanism protects the slowest atoms from light-assisted heating.

To perform the D1 gray molasses, we need to change the light frequency in the

optical table setup, see section 3.1.2. In this case, we need both cooling and repumper frequencies to be blue detuned from their respective transitions, see figure 3.2. The most important parameter in this cooling mechanism is not the overall detuning of both cooling and repumper frequencies [39], δ_1 and δ_2 , but rather the relative detuning between the both frequencies $\delta = \delta_1 - \delta_2$. In figure 3.17b, we report the so-called Fano-like profile characteristic of this gray molasses [17, 39].

The minimum attainable temperature using this cooling scheme is $42\mu\text{K}$, reached at the Raman condition ($\delta = 0$). At the Raman condition, the number of atoms remaining after the cooling process is lower than the maximum achievable number using this scheme at $\delta \approx -0.25\Gamma$. At this relative detuning, the temperature of the sample is in the order of $60\mu\text{K}$. In practice, after the D1 gray molasses, we end up with 4×10^8 atoms at a temperature of $T \approx 60\mu\text{K}$. After the gray molasses is applied, we perform an optical pumping stage to transfer the atoms to the state $2^2S_{1/2}$ with $F = 1/2$. This stage is crucial to exploit the lithium Feshbach resonances in the evaporation process.

3.3.2. The optical-magnetic potential

When an electromagnetic field, very far detuned from any electronic transition, interacts with an atom, its electric field induces an electric dipole moment in the atoms. The induced electric dipole moment is $\mathbf{d} = \alpha\mathbf{E}$, where α is the atom's polarizability. Therefore, the effective dipole potential is written as [41]:

$$U_{dip} = -\frac{1}{2}\mathbf{d} \cdot \mathbf{E}. \quad (3.7)$$

After performing a rotating frame of reference approximation in the optical potential's calculation, we can rewrite U_{dip} as follows:

$$U_{dip}(\mathbf{r}) = -\frac{1}{2\epsilon_0 c} \text{Re}[\alpha(\omega)] I(\mathbf{r}), \quad (3.8)$$

where $I(\mathbf{r}) = \frac{\epsilon_0 c}{2}|E_0|^2$ is the intensity profile of the electromagnetic field. Considering the far detuned limit, defining the detuning as $\Delta = \omega - \omega_0$, where the incoming field frequency is ω , and the transition frequency is ω_0 . The dipole potential reads [41]:

$$U_{dip}(\mathbf{r}) = \frac{3\pi c^2 \Gamma}{2\omega_0^3 \Delta} I(\mathbf{r}). \quad (3.9)$$

The intensity profile of the ODT is the one of a focused gaussian beam:

$$I_{ODT}(x, y, z) = \frac{2P}{\pi w_x(z)w_y(z)} \exp\left(-2\frac{x^2}{w_x(z)^2} - 2\frac{y^2}{w_y(z)^2}\right), \quad (3.10)$$

where the $1/e^2$ waists of the beam are $w_x(z) = w_{x0}\sqrt{1 + \left(\frac{z}{z_R}\right)^2}$, and $w_y(z) = w_{y0}\sqrt{1 + \left(\frac{z}{z_R}\right)^2}$. The value of the waists at the focus are w_{x0} , and w_{y0} . Since the gaussian beam is focused, the beam's waists depends on the propagation distance z . The Rayleigh length is defined as $z_R = \pi w_{x0}w_{y0}/\lambda$. Using this convention, the focus point is located at $\mathbf{r} = 0$.

Near the focus of the gaussian beam the dipole potential is approximated by:

$$U_{dip} \approx -U_0 \left[1 - \left(\frac{z}{z_R}\right)^2 - 2\left(\frac{x}{w_{x0}}\right)^2 - 2\left(\frac{y}{w_{y0}}\right)^2 \right], \quad (3.11)$$

where the corresponding harmonic oscillator potential with frequencies are:

$$\omega_{zODT} = \sqrt{\frac{2U_0}{mz_R^2}}, \quad \omega_{xODT} = \sqrt{\frac{4U_0}{mw_{x0}^2}}, \quad \omega_{yODT} = \sqrt{\frac{4U_0}{mw_{y0}^2}}, \quad (3.12)$$

and the potential depth is:

$$U_0 = \frac{3\pi c^2 \Gamma}{2\omega_0^3 \Delta} \frac{2P}{\pi w_{x0} w_{y0}}. \quad (3.13)$$

The ODT provides weak confinement along the beam's propagation direction while providing tight confinement in its transverse direction. For this reason, the magnetic curvature of the quasi-Helmholtz configuration of the Feshbach field, see section 3.1.3, is necessary. This curvature provides the confinement along the ODT propagation direction. The magnetic potential is expressed as:

$$U_{mag}(x, y, z) \approx \frac{1}{2}m \left[\omega_{zmag}^2 z^2 - \omega_{rmag}^2 (x^2 + y^2) \right], \quad (3.14)$$

where $\omega_{zmag}^2 = \frac{\mu}{m} \partial_{zz} B_z(0)$, $\omega_{rmag}^2 = \frac{\mu}{m} \partial_{rr} B_r(0)$, and the atom's magnetic dipole mo-

ment is μ .

The net optical-magnetic potential can be expressed as the superposition of both optical (3.11) and (3.14) potential:

$$U_{opt-mag}(x, y, z) = \frac{1}{2}m [\omega_z^2 z^2 + \omega_x^2 x^2 + \omega_y^2 y^2], \quad (3.15)$$

where

$$\omega_z = \sqrt{\omega_{zODT}^2 + \omega_{zmag}^2}, \quad \omega_x = \sqrt{\omega_{xODT}^2 - \omega_{rmag}^2}, \quad \omega_y = \sqrt{\omega_{yODT}^2 - \omega_{rmag}^2}. \quad (3.16)$$

Following the optical molasses, without any magnetic field present, the cloud is expanding freely. For this reason, before the gray molasses ends, we turn on the ODT's power to confine the coldest atoms into the conservative potential. At this stage, the ODT's power is 180W, and it focuses on a waist of $50\mu\text{m}$ in both transversal directions in the center of the cloud, as shown in figure 3.18a.

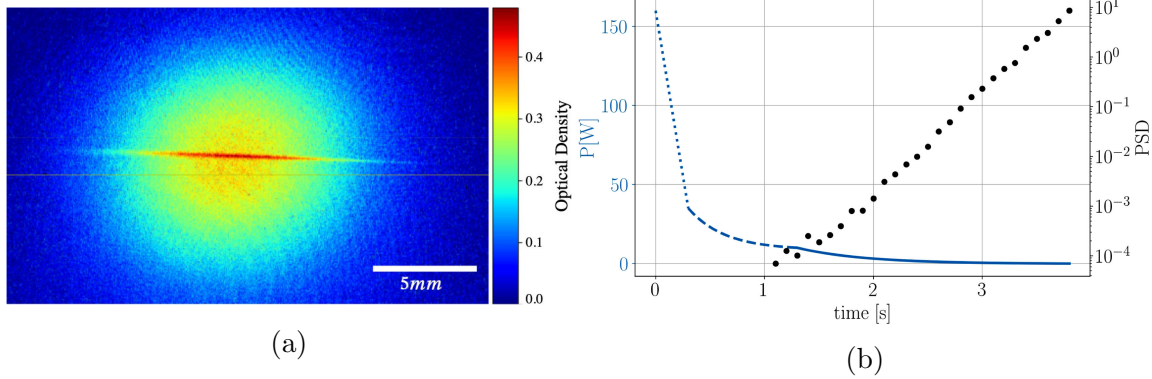


Figure 3.18: a) Image of the ODT transfer stage: we see the expanding cloud after the gray molasses stage in the back, the sudden increase in density corresponds to the atoms captured by the ODT. b) Evaporation curve (blue lines), and phase-space density (black dots) of the cloud as a function of the evaporation time.

At this stage, the confinement along both the axial and radial directions is purely coming from the ODT. After loading the atoms into the ODT, we ramp the Feshbach field from 0 up to 832G in 32ms. The magnetic field's ramp is such to create an almost 50:50 mixture of states with $m_F = 1/2$ and $m_F = -1/2$ in the state $F = 1/2$. This combination of states is required to exploit the Feshbach resonance to perform efficient runaway evaporation.

To carry out the evaporative cooling, we decrease the ODT power following the

curve in figure 3.18b. We perform three ramps until reaching degeneracy. The first two ramps of the evaporation (dotted and dashed lines in figure 3.18b) occur by decreasing the power output of the IPG laser from 180W up to 10W. After this point, we control the ODT power adjusting the efficiency of the AOM in the optical setup in figure 3.5. During this last step, it is crucial to reduce as much as possible any source of electronic noise that may convert into power noise in the ODT, therefore a heating mechanism for the atoms. For this reason, we control the AOM's efficiency using a PID controller.

To quantify the evaporation efficiency, we calculate the phase space density (PSD) of the cloud as a function of the evaporation time. When $PSD \ll 1$, we can consider the atomic cloud to be in the classical regime. When the PSD reaches one or higher, the cloud begins to reach the quantum degenerate regime, see figure 3.18b.

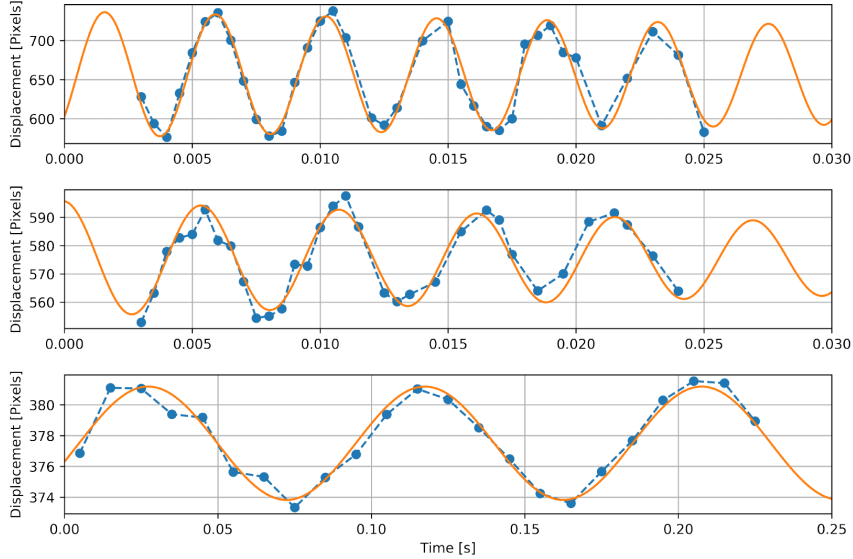


Figure 3.19: Center of mass position along the x, y and z directions after exciting the dipole mode. The measured frequencies are: $\omega_x = 2\pi \times 185.33$ Hz, $\omega_y = 2\pi \times 223.95$ Hz, and $\omega_z = 2\pi \times 10.754$ Hz.

At the end of the evaporation, we produce a superfluid containing about $N = 5 \times 10^4$ atomic pairs at a temperature of $T/T_F = 0.1$ (20 nK). The trap frequencies are $\omega_r = 2\pi \times 163$ Hz, and $\omega_z = 2\pi \times 10.754$ Hz, meaning a cigar-shaped geometry with an aspect ratio of the order of 1:15. To measure the potential's frequencies, we excite the cloud inducing a center of mass oscillation, known as the dipole mode. This excitation consists of displacing the cloud center of mass and let the atoms evolve. By measuring the position of the cloud as a function of time, we estimate

the trap frequencies. To amplify the oscillation's signal, we let the cloud evolve a variable time, and then we perform a time-of-flight measurement. An example of those measurements are shown in figure 3.19. More details can be found in [34].

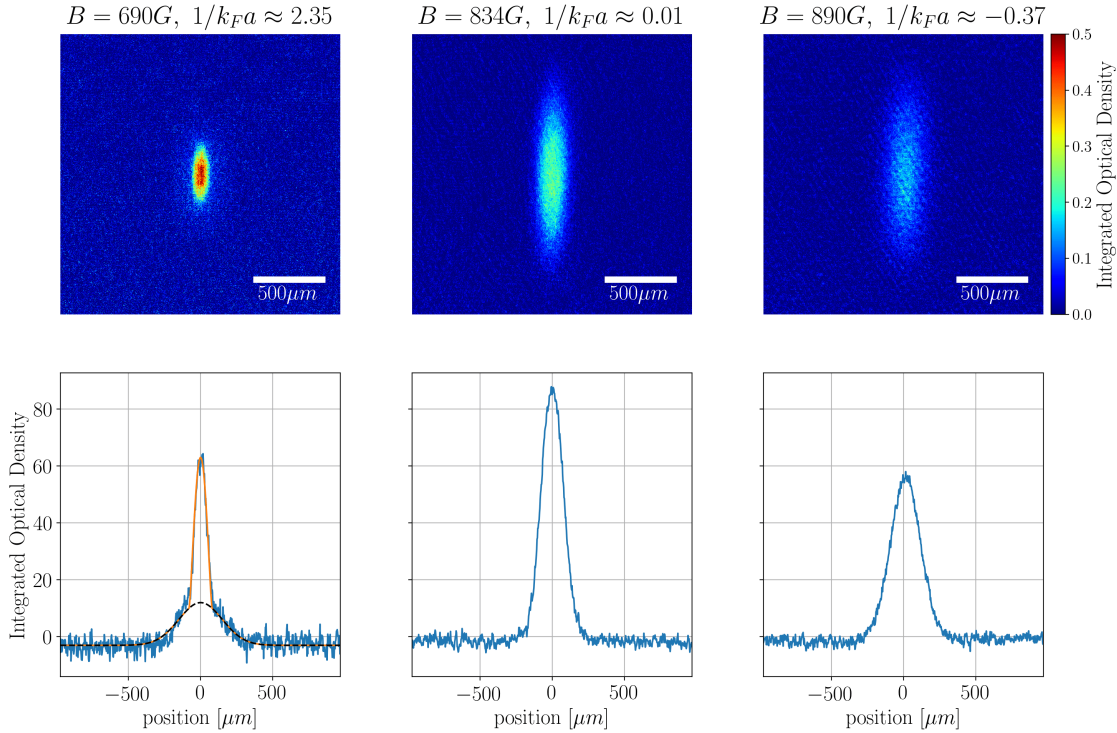


Figure 3.20: Absorption images of quantum degenerate atomic samples (upper pictures) and their corresponding integrated density profile (lower graphs). Left panels: Bose-Einstein condensate of molecules at $1/k_F a \approx 2.35$. Middle panels: superfluid gas at unitarity at $1/k_F a \approx 0.01$. Right panels: ultracold gas at the BCS side of the Feshbach resonance at $1/k_F a \approx -0.37$. All pictures were taken after 20 ms of time-of-flight.

At the end of the evaporation, we adiabatically ramp the Feshbach field to the desired value to produce a sample in any desired interaction regime across the Feshbach resonance. We can switch between a Bardeen-Cooper-Schrieffer (BCS) type superfluid and a Bose-Einstein condensate (BEC) of tightly bound molecules through the BEC-BCS crossover [22]. At the crossover, we create a strongly interacting superfluid known as unitary fermi gas (UFG).

To explore the different superfluid regimes, we syntonize the magnetic field to 690, 832, and 890 G creating an mBEC, a UFG, and a BCS superfluid, respectively. Figure 3.20 shows the density profile of the cloud after 20ms time-of-flight.

Chapter 4

Imaging procedure and calibration

In this chapter, we present different types of imaging techniques. We start by describing the conventional absorption imaging in two distinct regimes: the low and high-intensity regimes. Lastly, we describe one non-destructive imaging technique called phase-contrast imaging. The low-intensity absorption imaging is very convenient due to its simplicity and lack of prior calibration. Nonetheless, this regime is not suitable for high magnification imaging setups. For this reason, we implement high-intensity absorption imaging, although, needs to be calibrated. For non-destructive imaging, we implemented phase-contrast imaging, allowing us to record multiple times the same atomic sample.

4.1. Semi-classical light-matter interaction

In this section, we briefly describe the light-matter interaction between a two-level system and monochromatic light.

At the basis of the light-matter interaction, light is scattered off the atoms in cycles of absorption and spontaneous emission events at a rate described by the light and atomic properties. Using a semi-classical description of the light-matter interaction we arrive to the optical Bloch equations (OBE) [42]. The OBE describes both the coherent dynamics and the dissipative processes due to spontaneous emission. In the simple case of a two-level system interacting with single frequency light, the time evolution for the atomic density matrix ρ reads [42]:

$$\begin{aligned}
\frac{\partial \rho_{gg}}{\partial t} &= -i \frac{\Omega}{2} (\rho_{eg} - \rho_{ge}) + \Gamma \rho_{ee}, \\
\frac{\partial \rho_{ee}}{\partial t} &= i \frac{\Omega}{2} (\rho_{eg} - \rho_{ge}) - \Gamma \rho_{ee}, \\
\frac{\partial \rho_{ge}}{\partial t} &= - \left(i\Delta + \frac{\Gamma}{2} \right) \rho_{ge} - i \frac{\Omega}{2} (\rho_{ee} - \rho_{gg}), \\
\frac{\partial \rho_{eg}}{\partial t} &= \left(i\Delta - \frac{\Gamma}{2} \right) \rho_{eg} + i \frac{\Omega}{2} (\rho_{ee} - \rho_{gg}),
\end{aligned} \tag{4.1}$$

where $\Omega = -\frac{1}{\hbar} \langle g | \mathbf{d} | e \rangle E_0$ is the Rabi frequency, \mathbf{d} is the electric dipole moment operator, E_0 the amplitude of the light electric field, $\Delta = \omega - \omega_0$ is the detuning from the resonant frequency ω_0 , and Γ the natural linewidth of the transition between the ground, $|g\rangle$, and excited state, $|e\rangle$. The time evolution equations (4.1), arises after the rotating wave approximation (RWA) has been carried out [42].

To solve (4.1), we'll consider the case when the light-matter interaction is longer than the emission rate $1/\Gamma$, meaning the atoms interact with light in a steady-state regime. This approximation reduces (4.1) to:

$$\begin{aligned}
\rho_{gg}^{st} + \rho_{ee}^{st} &= 1, \quad \rho_{ee}^{st} = i \frac{\Omega}{2\Gamma} (\rho_{eg}^{st} - \rho_{ge}^{st}), \\
i \frac{\Omega}{2} (\rho_{ee}^{st} - \rho_{gg}^{st}) &= - \left(i\Delta + \frac{\Gamma}{2} \right) \rho_{ge}^{st}, \\
i \frac{\Omega}{2} (\rho_{ee}^{st} - \rho_{gg}^{st}) &= - \left(i\Delta - \frac{\Gamma}{2} \right) \rho_{eg}^{st}.
\end{aligned} \tag{4.2}$$

After solving this set of equations, we obtain:

$$\rho_{gg}^{st} = \frac{1 + \left(\frac{\Omega}{\Gamma}\right)^2 + \left(\frac{2\Delta}{\Gamma}\right)^2}{1 + 2 \left(\frac{\Omega}{\Gamma}\right)^2 + \left(\frac{2\Delta}{\Gamma}\right)^2}, \quad \rho_{ee}^{st} = \frac{\left(\frac{\Omega}{\Gamma}\right)^2}{1 + 2 \left(\frac{\Omega}{\Gamma}\right)^2 + \left(\frac{2\Delta}{\Gamma}\right)^2}, \tag{4.3}$$

$$\rho_{ge}^{st} = \frac{-(-i + 2\frac{\Delta}{\Gamma}) \frac{\Omega}{\Gamma}}{1 + 2 \left(\frac{\Omega}{\Gamma}\right)^2 + \left(\frac{2\Delta}{\Gamma}\right)^2}, \quad \rho_{eg}^{st} = \frac{-(i + 2\frac{\Delta}{\Gamma}) \frac{\Omega}{\Gamma}}{1 + 2 \left(\frac{\Omega}{\Gamma}\right)^2 + \left(\frac{2\Delta}{\Gamma}\right)^2}. \tag{4.4}$$

The average excited state population in the steady state regime is defined as the

light scattering rate:

$$R_{ee}^{st} = \Gamma \rho_{ee}^{st} = \frac{\Gamma}{2} \frac{s_0}{1 + s_0 + \left(\frac{2\Delta}{\Gamma}\right)^2}, \quad (4.5)$$

where we defined the saturation parameter as $s_0 = 2 \left(\frac{\Omega}{\Gamma}\right)^2$. A more convenient form to express the saturation parameter is $s_0 = I/I_{sat}$, where I is the intensity of the light, and $I_{sat} = \hbar\omega_0^3\Gamma/12\pi c^2$ is the saturation intensity of the transition.

Figure 4.1, shows the numeric integration of the complete set of OBE, equation (4.3). Firstly, we notice that for times longer than $t_c \approx 10\Gamma^{-1}$, the system reaches the steady-state solution. In the case of lithium, $\Gamma = 2\pi \times 5.87\text{MHz}$, meaning $t_c^{Li} \approx 0.27\mu\text{s}$. This timescale is shorter than our experimental time-resolution of $1\mu\text{s}$, justifying the use of the steady-state solutions. Additionally, the analytical values obtained in (4.3) are in agreement with the numerical ones.

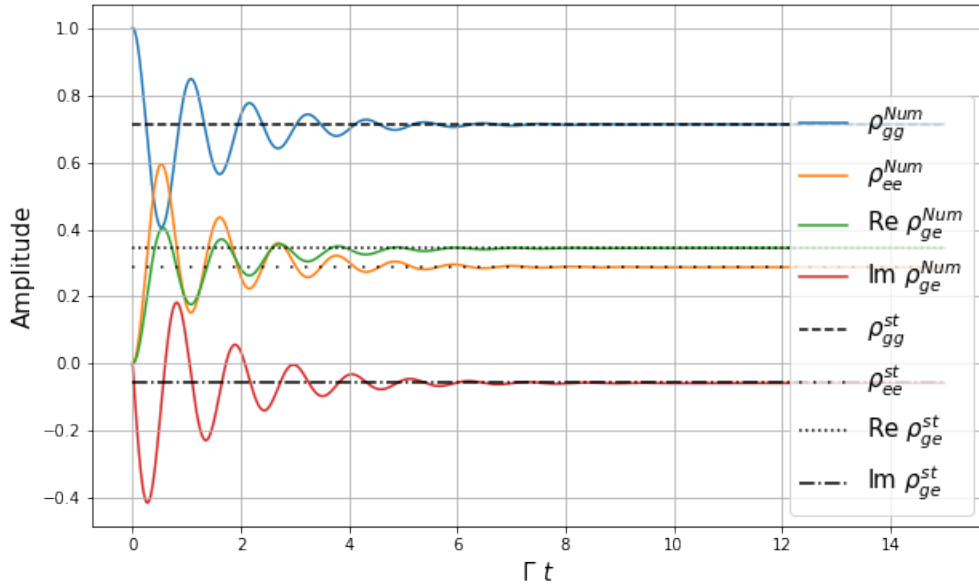


Figure 4.1: Numeric integration of (4.1), with $\Omega = 5\Gamma$ and $\Delta = -3\Gamma$. The steady state regime is achieved after $t_c \approx 10\Gamma^{-1}$.

In the case of a multilevel atom, the OBE should cover all the possible couplings depending on the light's polarization and the atomic structure [7, 43, 44]. The scattering rate should be the sum over all steady-state populations of all the excited states, $R = \sum_e \Gamma_e \rho_{ee}$.

When the probe's polarization is perfectly circular, and the driven transition oc-

curs between the extrema hyperfine sublevels (*e.g.* $|1/2, \pm 1/2\rangle$ to $|3/2, \pm 3/2\rangle$), then the two-level atom description is a good approximation. Nonetheless, when the polarization is not perfectly polarized circularly, the additional hyperfine sublevels will be populated. For this and other experimental imperfections, it is convenient to define an effective saturation parameter [7, 43, 44], $s_0^{eff} = s_0/\alpha$, where α is a parameter taking into account such experimental imperfections. For this reason, we'll consider the following scattering rate:

$$R_\alpha = \frac{\Gamma}{2} \frac{s_0/\alpha}{1 + s_0/\alpha + (2\Delta/\Gamma)^2}. \quad (4.6)$$

The average power absorbed by the two-level atoms over an optical period can be calculated through the average work done by the electric field per unit time [42]:

$$\left\langle \frac{dW}{dt} \right\rangle_{st} = \hbar\Omega\omega \frac{\Omega/\Gamma}{1 + 2\left(\frac{\Omega}{\Gamma}\right)^2 + \left(\frac{2\Delta}{\Gamma}\right)^2}. \quad (4.7)$$

To estimate the average number of photons absorbed per unit of time, we divide the average power absorbed by the photon's energy, $\hbar\omega$:

$$\left\langle \frac{dN}{dt} \right\rangle_{st} = \frac{1}{\hbar\omega} \left\langle \frac{dW}{dt} \right\rangle_{st} = \frac{\Omega^2/\Gamma}{1 + 2\left(\frac{\Omega}{\Gamma}\right)^2 + \left(\frac{2\Delta}{\Gamma}\right)^2} = \Gamma\rho_{ee}^{st} = R_{ee}^{st} \rightarrow R_\alpha. \quad (4.8)$$

Following the absorption-emission process, an effective energy transfer happens. The energy increase per unit of time depends on the number of photons scattered and the atom's recoil energy when absorbing or emitting a photon:

$$\left\langle \frac{dE}{dt} \right\rangle_{st} = 2E_{rec} \left\langle \frac{dN}{dt} \right\rangle_{st} = 2E_{rec} R_{ee}^{st} \rightarrow 2E_{rec} R_\alpha. \quad (4.9)$$

where $E_{rec} = \hbar^2 k^2 / 2m$ is the recoil energy, with $k = \omega/c$.

During the imaging procedure, we probe the atoms for some time τ . If we want the imaging procedure to be non-destructive, we need to consider the probe's effect on the cloud. For this reason, we propose that the increase of the cloud's temperature is simply $k_B \langle \frac{\Delta T}{\Delta t} \rangle_{st} = \langle \frac{dE}{dt} \rangle_{st}$. Therefore:

$$\langle \Delta T \rangle_{st} = 2\tau T_{rec} R_{ee}^{st} \rightarrow 2\tau T_{rec} R_\alpha, \quad (4.10)$$

where, we defined the recoil temperature as $T_{rec} = E_{rec}/k_B$. Figure 4.2 shows the increase of the cloud's temperature per unit time as a function of the probe's detuning.

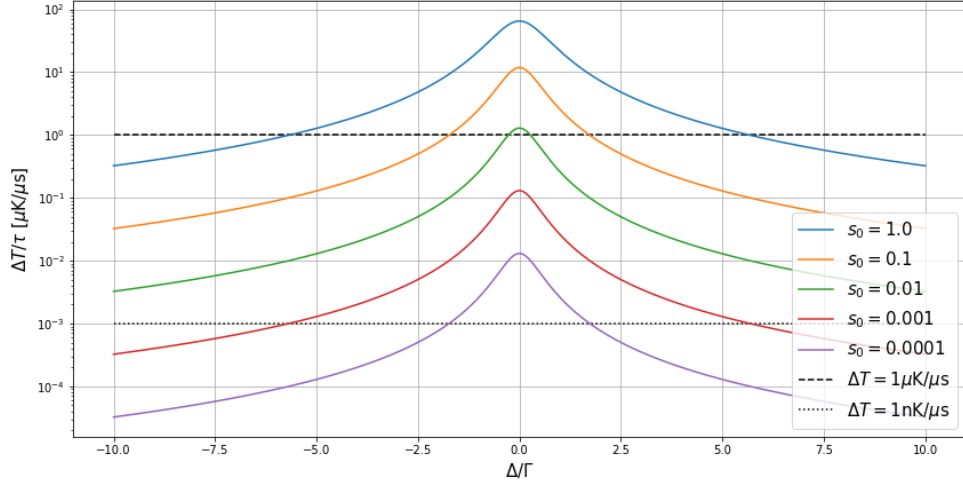


Figure 4.2: Increase of the cloud's temperature per unit of time of a two-level system as a function of the probe's detuning, with $T_{rec}^{Li} = 3.53\mu\text{K}$, see appendix A.

This simple model will help us determine the best parameters to perform non-destructive imaging. We may perform imaging using very low intensity and very far-detuned, but this will result in a low signal-to-noise ratio, as we'll discuss in section 4.2.3. We'll return to this model at the end of the chapter when describing the phase-contrast non-destructive imaging.

4.2. Absorption imaging technique

In this section, we will describe the absorption imaging technique. In particular, we discuss the imaging technique calibration process in the high-intensity regime using two different methods. Additionally, we discuss how we can enhance the image quality: focusing the imaging setup using the shadowgraphy technique and using a fringe removal algorithm to reduce the induced noise in the imaging process. Finally, we discuss the phase-contrast imaging technique, showing its non-destructive nature.

4.2.1. Optical density calculation

Absorption imaging consists of imaging the shadow produced by an atomic cloud illuminated by resonant light. The atoms absorb part of the incoming radiation reducing the transmitted intensity. To model this process, we'll consider the two-level system coupled with a uniform monochromatic radiation field of the imaging light, see section 4.1. Experimentally this is realized using a near collimated gaussian beam profile with a waist well above the characteristic sizes of the atomic sample. We model the propagation of light in the atomic medium by a Beer-Lambert law [29]:

$$\begin{aligned} \frac{dI}{dz}(x, y, z) &= -n_{3D}(x, y, z)\sigma(I(x, y)) \\ \frac{dI}{dz}(x, y, z) &= -n_{3D}\sigma_0 I_{sat} \frac{s_0(x, y, z)/\alpha}{1 + s_0(x, y, z)/\alpha + (2\Delta/\Gamma)^2}, \end{aligned} \quad (4.11)$$

where $\sigma(I) = \sigma_0 I_{sat} R_\alpha$ is the effective cross-section as a function of the intensity, and $\sigma_0 = 3\lambda^2/2\pi$ is the resonant cross-section for a two-level atom. Fortunately, we can solve equation (4.11) for the optical density defined as: $OD = \sigma_0 n_c$, where $n_c(x, y) = \int_{-\infty}^{\infty} n_{3D}(x, y, z) dz$ is the column density. After solving equation (4.11) we get:

$$OD(x, y) = -\alpha \left(1 + \left(\frac{2\Delta}{\Gamma} \right)^2 \right) \ln \left(\frac{I_{z=\infty}(x, y)}{I_{z=-\infty}(x, y)} \right) + \frac{I_{z=-\infty}(x, y) - I_{z=\infty}(x, y)}{I_{sat}}. \quad (4.12)$$

In the cold atoms imaging context, $I_{z=-\infty}(x, y) = I_{probe}$, is the probe beam intensity profile without any atomic absorption, and $I_{z=\infty}(x, y) = I_{atoms}$, is the probe beam intensity profile after the interaction with the atoms. Rewriting (4.12) we get:

$$OD(x, y) = -\alpha \left(1 + \left(\frac{2\Delta}{\Gamma} \right)^2 \right) \ln \left(\frac{I_{atoms}(x, y)}{I_{probe}(x, y)} \right) + \frac{I_{probe}(x, y) - I_{atoms}(x, y)}{I_{sat}}. \quad (4.13)$$

Experimentally, we record the intensity profiles using a CCD camera. This process records the intensity profiles as images in a matrix of pixels. The pixel counts are proportional to the integrated light transmitted from a specific location on the object

plane over the probing time. After a probing time, τ , the pixel count at position (i, j) in the matrix image is related to the intensity profile as [8]:

$$C_{ij} = \eta GT \left(\frac{l_{pixel}}{M} \right)^2 \int_0^\tau \frac{I(x_i, y_j; t)}{\hbar\omega} dt \approx \chi_{sat} \frac{\langle I(x_i, y_j) \rangle}{I_{sat}} \tau, \quad (4.14)$$

where η is the quantum efficiency of the CCD sensor, G is the Analog-to-Digital conversion gain, T the transmission coefficient of the imaging setup, l_{pixel} is the pixel side length, M the imaging system magnification factor, and $\langle I(x_i, y_j) \rangle$ is the time-averaged intensity. For convenience, we define χ_{sat} as the proportionality factor:

$$\chi_{sat} = \eta GT \left(\frac{l_{pixel}}{M} \right)^2 \frac{I_{sat}}{\hbar\omega}. \quad (4.15)$$

The value of χ_{sat} can be estimated theoretically using the CCD camera characteristics. For the Andor camera, we can approximate the quantum efficiency to be $\eta \approx 1$ [38], we set the EMCCD gain to $G = 1$, we estimate the optical transmission to be $T \approx 1$. Finally, the pixel length is $l_{pixel} = 13\mu\text{m}$, and the magnification is $M \approx 8.12$, see section 3.2.3. Using this values, we should expect $\chi_{sat} \approx 219.9\mu\text{s}^{-1}$. We'll try to estimate this value experimentally in the following sections.

It is important to note that χ_{sat} depends on both the imaging system and the CCD camera. To estimate the optical density, we consider additional noise sources in the image arising from background light and electronic noise such as dark counts. To reduce these noises, we acquire an additional image of the background with the probe beam turned off, denoted as C^{bg} . Substituting, (4.14) for each of the images in (4.13), we obtain:

$$OD(x_i, y_j) = -\alpha \left(1 + \left(\frac{2\Delta}{\Gamma} \right)^2 \right) \ln \left(\frac{C^{atoms}(x_i, y_j) - C^{bg}(x_i, y_j)}{C^{probe}(x_i, y_j) - C^{bg}(x_i, y_j)} \right) + \frac{C^{probe}(x_i, y_j) - C^{atoms}(x_i, y_j)}{\chi_{sat}\tau}. \quad (4.16)$$

4.2.2. Low Intensity approximation

In the limit of low probe intensity, $I \ll I_{sat}$, equation (4.11) can be approximated as:

$$\frac{dI}{dz} = -\frac{s_0/\alpha}{1 + (2\Delta/\Gamma)^2} \sigma_0 n_{3D} I. \quad (4.17)$$

The optical density then results in:

$$OD(x_i, y_j) = -\alpha \left(1 + \left(\frac{2\Delta}{\Gamma} \right)^2 \right) \ln \left(\frac{C^{atoms}(x_i, y_j) - C^{bg}(x_i, y_j)}{C^{probe}(x_i, y_j) - C^{bg}(x_i, y_j)} \right). \quad (4.18)$$

This approximation has the advantage that the constant χ_{sat} does not appear, meaning that the measured optical density is independent of the imaging system, contrary to the high-intensity regime case. In this approximation, α is the only constant to calibrate. When applying an external bias magnetic field, α depends on the probe polarization and the imaging direction. When driving the D2 σ^- transition between the states $m_J = -1/2$ to $m_{J'} = -3/2$ along the orthogonal direction of the external magnetic field, it can be shown that $\alpha = 2|\sin \theta|^2$, where θ is the angle between the magnetic field, and the probe polarization. The maximum value of α is 2 and happens when the polarization is orthogonal to the magnetic field. To maximize the optical density signal, the value of θ is set to $\pi/2$. Meaning, the probe polarization along the horizontal axis is orthogonal to the magnetic field.

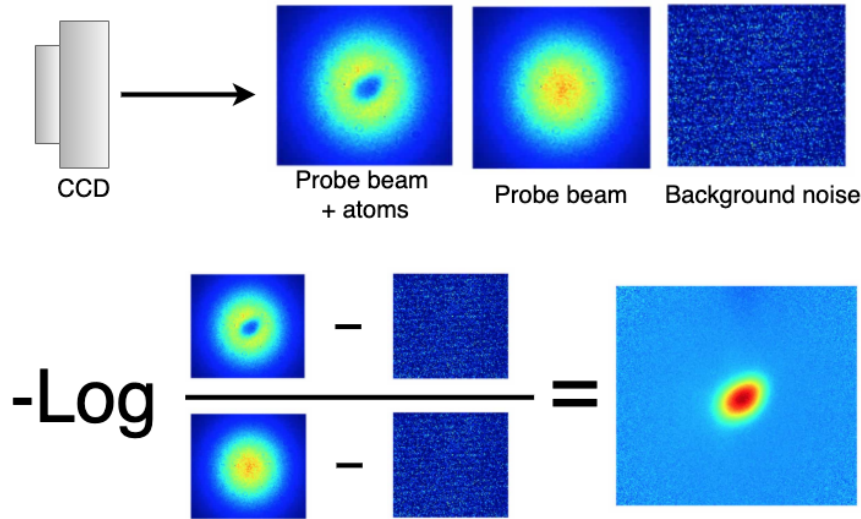


Figure 4.3: Pictorial view of the optical density calculation. The CCD camera acquires the three images required to calculate the optical density: C^{atoms} , C^{probe} and C^{bg} . Finally, to obtain the optical density we apply the relation (4.18). To make visible the background noise visible we amplified it a factor of 500.

4.2.3. High intensity regime

Working on a low-intensity regime is not always possible. The higher the imaging system magnification, the higher the probe intensity required to keep constant the signal to noise ratio (SNR). For this reason, in the high-intensity regime, we need to use the full expression of the optical density obtained in (4.16). To achieve the highest SNR, we'll consider the probe frequency is on resonance, $\Delta = 0$. Therefore, the optical density is:

$$OD(x_i, y_j) = -\alpha \ln \left(\frac{C^{atoms}(x_i, y_j) - C^{bg}(x_i, y_j)}{C^{probe}(x_i, y_j) - C^{bg}(x_i, y_j)} \right) + \frac{C^{probe}(x_i, y_j) - C^{atoms}(x_i, y_j)}{\chi_{sat}\tau}. \quad (4.19)$$

There exist several strategies to calibrate both α and χ_{sat} . The first one is to estimate the value of χ_{sat} acquiring multiple images realized with an intensity equal to the saturation intensity at various pulse length. Using this strategy, it is possible to obtain χ_{sat} using (4.14). This method needs to image the full-beam profile to known with precision the beam waists. Otherwise, this method introduces large errors in the value of χ_{sat} . This method is straightforward along the horizontal axis since we can change the imaging magnification to characterize first the beam profile using the low magnification setup, see section 3.2.2. Once the beam waists are measured, we switch to the magnified imaging system to calibrate the α coefficient using Reinaudi's method [7], as discussed in the following section.

Along the vertical axis, we cannot characterize the beam profile using this method because there is no alternative to the system magnification. Nonetheless, we can rewrite (4.19) to obtain an effective optical density OD^* defined as:

$$OD^*(x_i, y_j) = -\ln \left(\frac{C^{atoms}(x_i, y_j) - C^{bg}(x_i, y_j)}{C^{probe}(x_i, y_j) - C^{bg}(x_i, y_j)} \right) + \frac{C^{probe}(x_i, y_j) - C^{atoms}(x_i, y_j)}{\chi_{sat}^*\tau}, \quad (4.20)$$

where $OD^* = OD/\alpha$ is the effective optical density, and $\chi_{sat}^* = \alpha\chi_{sat}$ an effective calibration constant. Rewriting the optical density in this way enables us to perform the calibration process. The constant χ_{sat}^* is estimated using two different methods: Reinaudi's [7] and Horikoshi's [8] methods. To calibrate α , we compare for the same atomic sample the values of OD^* and OD , along the vertical and horizontal axis, respectively. Along the horizontal axis, we can probe the atomic cloud in the low-

intensity regime where, in principle, the effect of the linear term in (4.19) can be neglected, making easier the calibration along the horizontal axis.

Horizontal axis calibration

To know the probe intensity when acquiring an image, we measure both the probe real power, and beam waists. To measure the probe power, we monitored the transmission through one of the mirrors of the imaging setup using a photodiode, see top section of figure 4.4. Once calibrated the photodiode, we compare the probe beam intensity with the CCD pixel count.

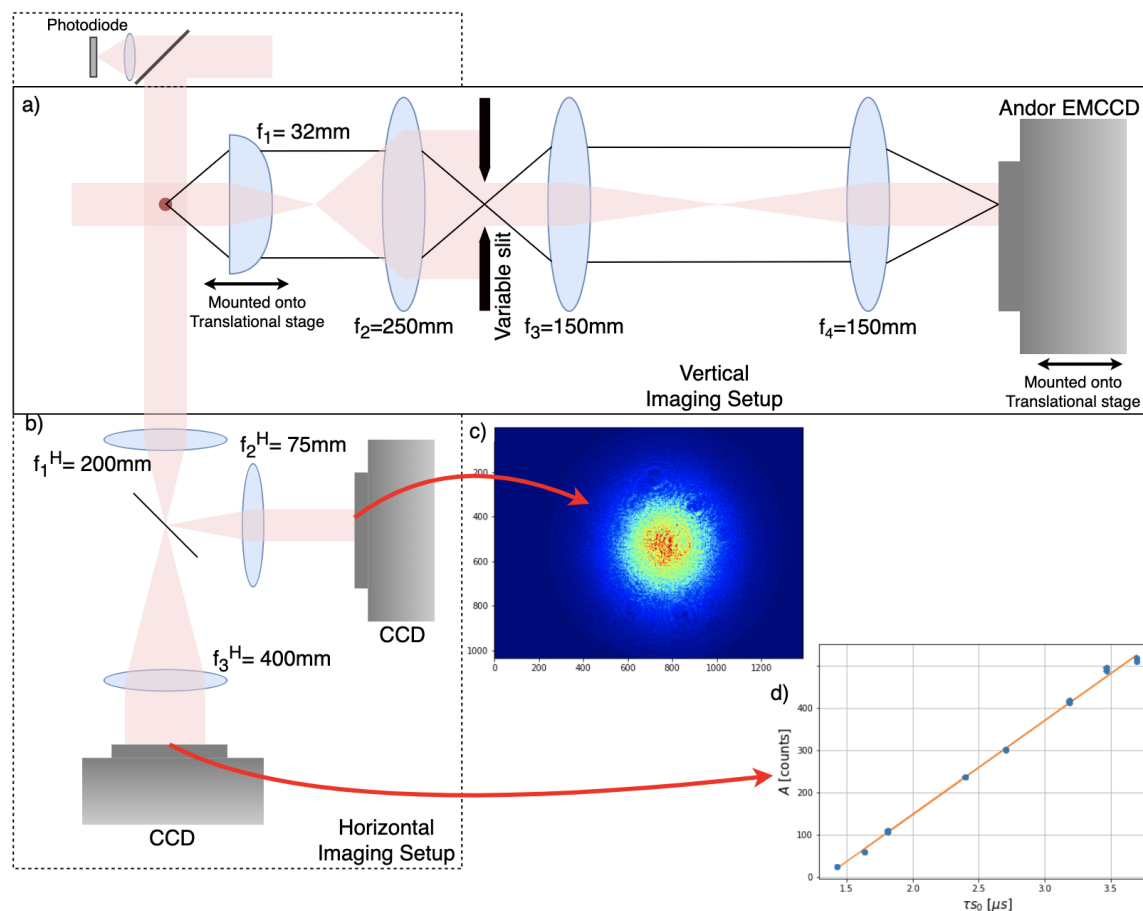


Figure 4.4: a) Vertical imaging setups, delimited by the continuous line. b) horizontal imaging setup, delimited by the dashed line. c) Raw image of the probe beam, from which it is possible to extract the probe waists: $w_x = 6.690(3)\text{mm}$ and $w_y = 7.014(2)\text{mm}$. d) Amplitude of the gaussian beam profile as a function of the probe duration and intensity.

The low-magnification imaging setup has a wide field of view able to image the

complete beam profile, see figure 4.4c. Using a Gaussian function of the form: $Ae^{-2x^2/w_x^2-2y^2/w_y^2}$ to fit the beam profile. The measured beam waists are: $w_x = 6.690(3)\text{mm}$ and $w_y = 7.014(2)\text{mm}$.

Once the beam waists are measured using the low-magnification setup, we switch to the magnified imaging setup and acquire a series of the images of the probe beam. Using the same Gaussian function fit, we related the value of the amplitude, A , to the probe intensity. Using the fact that $A = \chi_{sat}s_0\tau$, see equation (4.14), we obtain:

$$A = \chi_{sat} \frac{2P}{\pi w_x w_y I_{sat}} \tau. \quad (4.21)$$

Since we can control the probe duration, we know the beam waists, and we can measure the probe real power using the photodiode. We plot the values of A against $s_0\tau$ to obtain the calibration constant χ_{sat} , see figure 4.4d. A linear fit reveals the value of χ_{sat} along the horizontal setup: $\chi_{sat}^H \approx 221(2)$ counts/ μs .

Calibration of the α in the horizontal axis: Reinaudi's method

This calibration method uses that equation (4.19) can be divided into two components. The first one has the property that only involves properties of the atomic cloud [7]. The second part depends on the imaging light intensity. Following the suggested method, we define the following functions [7]:

$$\begin{aligned} od_0(x_i, y_j) &\equiv \sigma_0 n_c(x_i, y_j), \\ f(x_i, y_j; A) &\equiv -A \ln \left(\frac{C^{atoms}(x_i, y_j) - C^{bg}(x_i, y_j)}{C^{probe}(x_i, y_j) - C^{bg}(x_i, y_j)} \right) + \frac{C^{probe}(x_i, y_j) - C^{atoms}(x_i, y_j)}{\chi_{sat} \tau}. \end{aligned} \quad (4.22)$$

Using this distinction, equation (4.19) states that $od_0(x_i, y_j) = f(x_i, y_j; \alpha)$, where α is such that the density profile remains constant regardless of the imaging light intensity. In practice, we infer the value of α by minimizing the standard deviation of the density profiles across all images taken under different probe intensities and duration.

The calibration process begins by producing an atomic sample with low atom number fluctuation to maintain $od_0(x, y)$ as constant as possible. Then, we measure

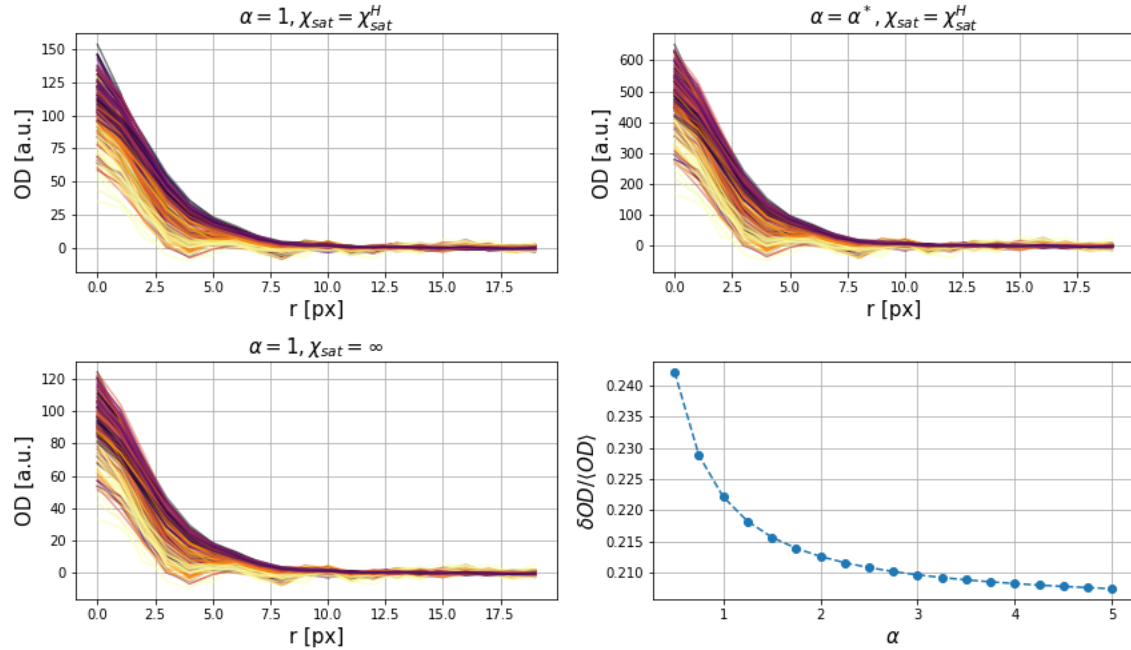


Figure 4.5: Density profiles taken along the horizontal direction at different probe intensities and durations, darker colors signifying lower intensities. Top left: using $\alpha = 1$ and $\chi_{sat} = \chi_{sat}^H = 221$ counts/ μ s, top right: using $\alpha = 5$ and $\chi_{sat}^H = 221$ counts/ μ s, and bottom left: using $\alpha = 1$ and $\chi_{sat} = \infty$ counts/ μ s. The bottom right panel shows the ratio of the standard deviation of the density profiles to the peak optical density. The last panel suggest that the dispersion get lower when increasing α , implying more data needs to be taken, see text.

the atomic profile for different intensities and duration of the probe pulse. Figure 4.5 shows the integrated density profiles, darker colors signifying lower intensities. On the top left, we plot the density profiles using no calibration of α , using the correction term χ_{sat}^H . It is clear that the measured profile decrease in height with higher intensities, requiring calibration of the α parameter. This effect is caused by the saturation of the atomic transition.

To obtain the value of α , we calculate the standard deviation of the density profiles taken at different intensities and durations, as shown in the bottom right panel of figure 4.5. The value of α that reduces the density curves dispersion seems to be the highest tried, $\alpha = 5$. Nonetheless, this value increases significantly the peak OD of the profiles (see both top panels of figure 4.5). This behavior indicates that the linear term in the optical density calculation does not play a significant role. That is made clear by looking at the bottom left panel of figure 4.5, where we calculated the density

profiles without the linear term. We would need to take additional data using higher intensities to make this calibration process. For this reason, we'll use the theoretical value of $\alpha^H = 2$, and $\chi_{sat}^H = \infty$ (low-intensity approximation) for the rest of the data presented.

Calibration of the vertical axis: Reinaudi's method

Analogously to the calibration process of the absorption cross-section along the horizontal axis, along the vertical direction, we define the following functions [7]:

$$od_0^*(x_i, y_j) \equiv \frac{\sigma_0}{\alpha} n_c(x_i, y_j), \quad (4.23)$$

$$f^*(x_i, y_j; \chi) \equiv -\ln \left(\frac{C^{atoms}(x_i, y_j) - C^{bg}(x_i, y_j)}{C^{probe}(x_i, y_j) - C^{bg}(x_i, y_j)} \right) + \frac{C^{probe}(x_i, y_j) - C^{atoms}(x_i, y_j)}{\chi\tau}. \quad (4.24)$$

In this case, the identity (4.20) reads $od_0^*(x_i, y_j) = f^*(x_i, y_j; \chi_{sat}^*)$. Where χ_{sat}^* is such that the density profile remains constant regardless of the probe's intensity. Without any calibration, *i.e.* $\chi = \infty$, we obtain the density profiles shown in the left column of figure 4.6 for probe pulses of 1 μs , and 4 μs . In this case, the effect of the probe's intensity is clearer. For higher intensities, we obtain a lower optical density signal.

To obtain the value of χ_{sat}^* , we proceed as previously described. This time will repeat the analysis separating the profiles by probe duration. Figure 4.7a, shows the standard deviation of the density profiles as a function of the parameter χ for each pulse length. We observe a similar behavior of the curves. For low values of χ_{sat} , the density profile variation increases, while for large values of χ , the deviation saturates to a finite value. This limit corresponds to the low-intensity limit variation, where the linear term of (4.20) vanishes, left column of figure 4.6. For values of χ around 200, the deviations of the profiles for $\tau > 1$ have the same minimum value. We estimated the value to be $\chi_{sat}^V \approx 236(3)$ counts/ μs .

To calibrate the absorption cross-section along the vertical axis, we compare the peak optical densities for the sample atomic sample along the horizontal and vertical axis. The mean peak optical density along the horizontal axis is $OD_{peak}^H = 180.8 \pm 30$, while for the vertical axis is $OD_{peak}^V = 174 \pm 13$. Taking the ratio of both optical

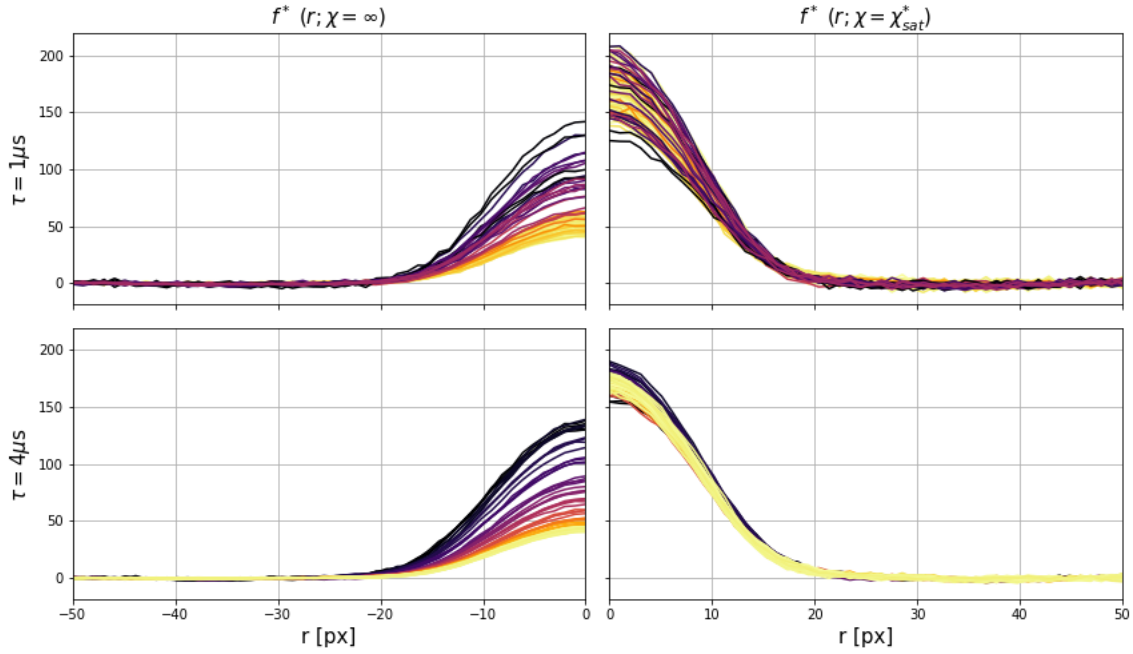


Figure 4.6: Density profiles obtained along the vertical axis at different probe intensities and durations. Darker colors, signifying lower intensities. The top and bottom left column correspond to the non calibrated case $\chi = \infty$, for probe durations of $1 \mu\text{s}$, and $4 \mu\text{s}$, respectively. The top and bottom right column correspond to the calibrated case with $\chi = 236(3)$ counts/ μs .

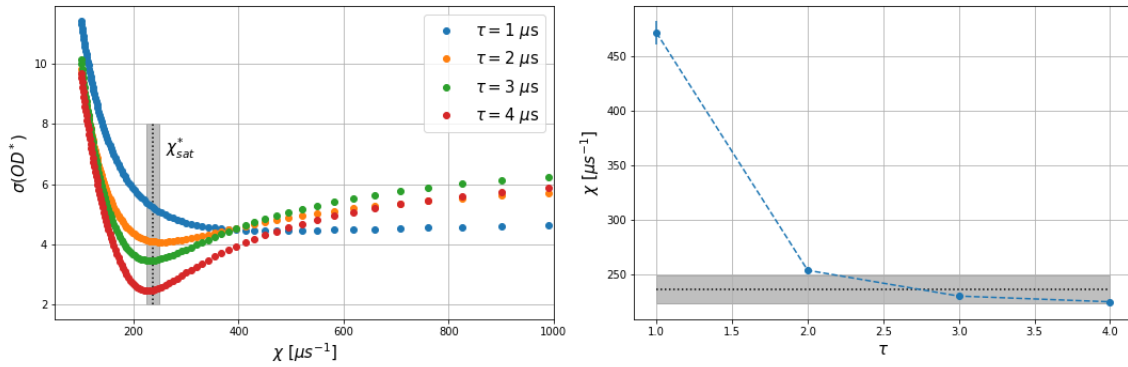


Figure 4.7: Left panel: standard deviation of the density profiles as a function of the parameter χ for multiple probe times. Right panel: the minimum deviation value of the density profiles standard deviation as a function of the pulse time. The dotted line represent $\chi_{sat}^V \approx 236(3)$ counts/ μs with the grey area representing 5 standard deviation.

density's we obtain $\alpha_V = 1.04(8)$.

Calibration of the vertical axis: Horikoshi's method

The second calibration method rewrites the equation (4.20) as a linear relationship between the two quantities C_1 and C_2 defined as follows [8]:

$$C_1(x_i, y_j) = -\ln \left(\frac{C^{atoms}(x_i, y_j) - C^{bg}(x_i, y_j)}{C^{probe}(x_i, y_j) - C^{bg}(x_i, y_j)} \right), \quad (4.25)$$

$$C_2(x_i, y_j) = \frac{C^{probe}(x_i, y_j) - C^{atoms}(x_i, y_j)}{\tau}, \quad (4.26)$$

where C_1 is the optical density in the low-intensity approximation, and C_2 is the correction term for the high-intensity regime. Rewriting equation (4.20) we get:

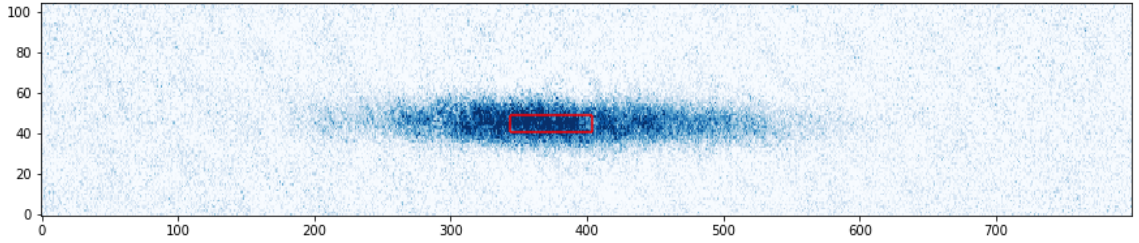


Figure 4.8: Picture of the atomic sample, showing the location of the ROI used in the calibration.

$$C_2(x_i, y_j) = \chi_{sat}^* OD^*(x_i, y_j) - \chi_{sat}^* C_1(x_i, y_j). \quad (4.27)$$

For each image we've taken, we consider a region of interest (ROI) in the center of the cloud, as shown in figure 4.8. The ROI needs to be smaller than the sample radial size to consider the density as a constant. Then, we calculate C_1 and C_2 averaging over the ROI. The unknown value $\chi_{sat}^* OD^*(x_i, y_j) = \chi_{sat} OD(x_i, y_j)$ is supposed to be constant inside the ROI. This fact allows us to perform a linear fit between the values C_1 and C_2 , and recover the constant χ_{sat}^* , see figure 4.9.

Using a linear fit to the data we get $\chi_{sat}^* \approx 238(8)$ counts/ μs . The error of χ_{sat}^* is higher than the value obtained using Reinaudi's method because of the large scattering of the data points. Nevertheless, this result can be improved by combining the analysis of a more dense sample, such as a fully condensed cloud, with a less dense thermal sample to cover a wider range of C_1 and C_2 values, by considering the vertical shift in the optical density.

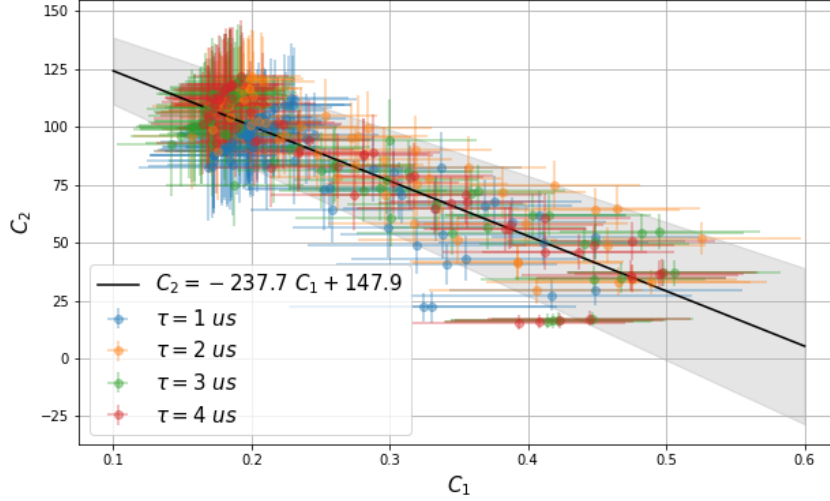


Figure 4.9: Linear fit of C_1 vs C_2 which gives $\chi_{sat}^* = 238(8)$ counts/ μs . The 5σ confidence interval is indicated by the shaded region.

Both calibration methods are consistent with each other. However, Horikoshi's calibration method is more susceptible to errors due to the cloud's size. Figure 4.8 illustrates this problem. The height of the region of interest is comparable with the cloud size, which is not the case along the horizontal direction, causing high dispersion in the data (figure 4.9). This effect introduces higher errors in the determination of the chi parameter. For this reason, we'll keep the calibration parameter obtained by Reinaudi's method. The error from both calibrations is limited mainly to the stability of the experimental setup.

Appropriate imaging conditions: pulse time, intensity, and signal to noise ratio

To have suitable imaging conditions, we need to consider two parameters: the imaging pulse duration τ and the probe's intensity s_0 . Both parameters are needed to be tuned to maximize the signal to noise ratio (SNR) of the optical density. The imaging pulse duration is closely related to the SNR, as can be seen qualitatively in figure 4.6, where the profiles with $\tau = 1\mu\text{s}$ are noisier than ones with $\tau = 4\mu\text{s}$.

To quantify which are the best parameters, we evaluate the SNR as a function of the pulse's duration and intensity. To calculate the SNR, we employ the following definition:

$$SNR = \frac{\langle OD^* \rangle}{\sigma_{OD}}, \quad (4.28)$$

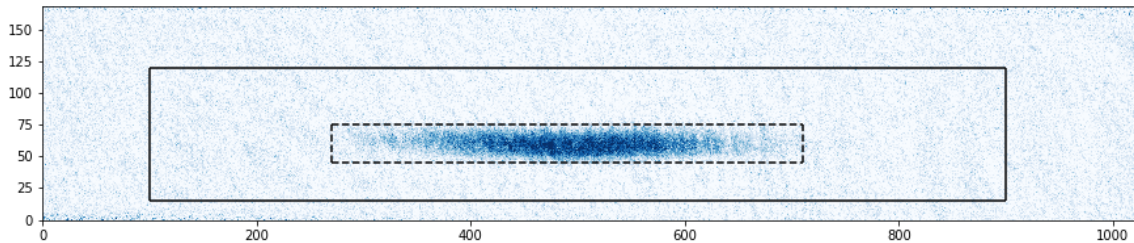


Figure 4.10: Sample image showing the ROI selection: dashed region to measure $\langle OD^* \rangle$, region between the continuous and dashed rectangles to measure the background noise level.

where $\langle OD^* \rangle$ is the mean value of the optical density in a region wherever the atomic cloud is located (dashed lines in figure 4.10), and σ_{OD} is the standard deviation of the background level (the region between the dashed and continuous lines in figure 4.10).

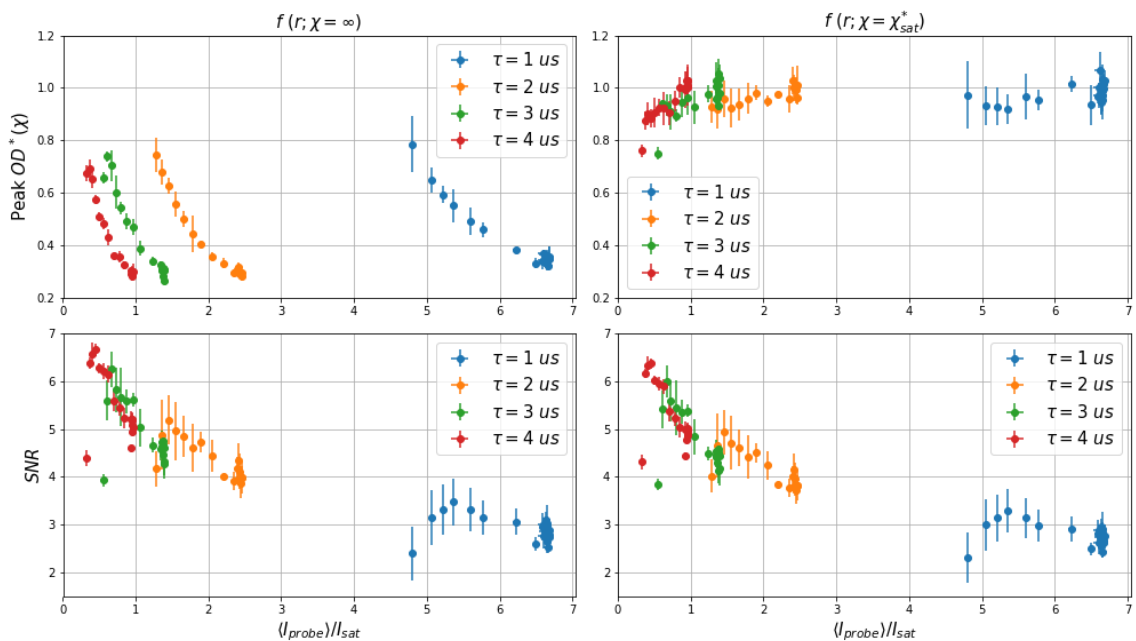


Figure 4.11: Top: peak optical density and bottom: SNR for the low-intensity approximation and the calibrated optical density. As expected for the corrected optical density, the peak OD remains constant for a large range of intensities and pulse length as opposed to the low-intensity approximation. For the SNR, we don't see any significant change between both cases.

Figure 4.11 shows a comparison between the SNR of the uncompensated and compensated optical densities. As expected for the corrected optical density, the peak

OD remains constant for a large range of intensities and pulse length as opposed to the low-intensity approximation. For the SNR, we don't see any significant change between both cases. However, for each probe duration, there is a critical value of intensity for which the SNR is maximum.

In figure 4.12a we plot the $\text{SNR}/\sqrt{\tau}$ as a function of $s_0\tau$. For each pulse length, we offset the horizontal axis to match the maximum value of the $\text{SNR}/\sqrt{\tau}$. Figure 4.12a, shows that the $\text{SNR}/\sqrt{\tau}$ follows the same behavior around the optimum value of intensity I_{opt} .

To analyze in more detail the optimum value of intensity, we draw the appropriate imaging condition region [8]. To measure the optical density using (4.19) properly, we must make sure that the assumptions made remain unchanged during the probe pulse duration. These conditions being a constant resonant condition and a constant density. Additionally, the SNR must be at least greater than unity to be able to detect the sample. We can model these conditions using the following inequalities [8]:

$$\tau < \frac{m\lambda^2 (1 + s_0)^{3/2}}{2\pi h s_0}, \quad (4.29)$$

$$\tau < 3 \left(\frac{m\lambda}{2h} L_{pix} \sqrt{\frac{1 + s_0}{\Gamma s_0}} \right)^{2/3}, \quad (4.30)$$

$$1 < \text{SNR}(\tau, s_0, OD). \quad (4.31)$$

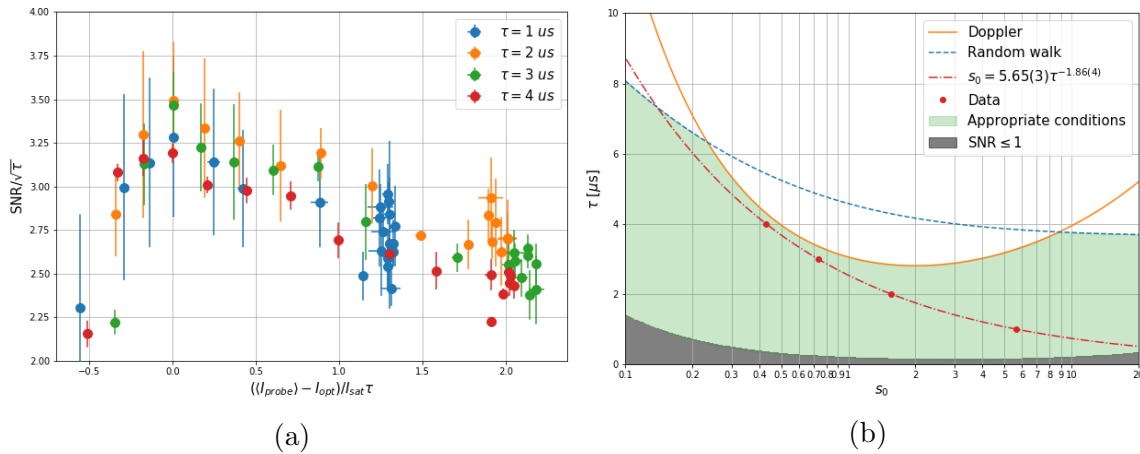


Figure 4.12: a) $\text{SNR}/\sqrt{\tau}$ as a function of $s_0\tau$ for multiple probe pulse duration. b) Appropriate imaging conditions for ${}^6\text{Li}$. Figure inspired from [8].

Condition (4.29) comes from the resonance condition: there is a Doppler shift

caused by the recoil velocity of atoms after absorbing a photon. Since the recoil velocity, $v_{rec} = \hbar k/m$, depends on the atom mass, light atoms are more responsive to the Doppler effect caused by photon recoils, requiring lower pulse duration. Condition (4.30) comes from a random walk condition. This condition ensures that atoms stay within the same pixel area, implying constant density, during the probe pulse. Finally, condition (4.31) is required to have a signal above the noise level. An extra condition may arise when considering the full atomic structure, and potential optical pumping effects. In [45] they exploit the optical pumping effect to produce high signal to noise absorption imaging. For more details on how to calculate the SNR as a function of the intensity, s_0 , the pulse duration τ , and the optical density, see [8]. Figure 4.12b shows these conditions. The Doppler condition, or resonance condition, is more restrictive than the random walk condition since the latter only limits for long probe pulses, $\tau > 6$, or very high intensity, $s_0 > 9$. The SNR condition is very versatile, requiring a probe pulse of at least $2\mu s$ at almost all intensities.

Moreover, in figure 4.12b, we show as red dots the optimum experimental value of intensity I_{opt} as a function of the pulse duration. The optimum intensity follows a simple relation with the probe duration, namely $I_{opt}/I_{sat} = 5.65(3)\tau^{-1.86(4)}$, red dash-dot curve. The relation suggests that for short probing times, we need to increase the probe's intensity to have the same $SNR/\sqrt{\tau}$, and vice versa. The SNR formula proposed by Horikoshi [8] does not recreate the obtained optimum intensity values for which the maximum SNR. This model has almost the same optimum value of intensity, $s_0 \approx 1.5$. Therefore, an adjustment to the model is required.

Our experimental data indicate that our best imaging conditions to acquire an absorption image is using a pulse length of $\tau = 4\mu s$, with an intensity of $I/I_{sat} \approx 0.5$.

4.3. Image quality enhancement

4.3.1. Focusing using shadowgraphy

To understand the defects introduced by a non-focused imaging setup, we'll try to model the atomic signal behavior after propagating in a defocused imaging setup [46]. After passing through the atoms, the probe beam will be attenuated and phase-

shifted. The resultant electric field is:

$$E_{atoms}(\mathbf{x}) = E_0 t(\mathbf{x}) e^{i\phi(\mathbf{x})}, \quad (4.32)$$

where the probe beam intensity before passing through the atoms is $I_0(\mathbf{x}) = \frac{c\epsilon_0}{2} |E_0|^2$, $t(\mathbf{x})$ is the transmittance function, and the phase shift is $\phi(\mathbf{x})$. These functions are derived in section 4.4, and are given by:

$$t(\mathbf{x}) = \exp\left(-\frac{1}{2} \frac{OD(\mathbf{x})}{1 + (2\Delta/\Gamma)^2}\right) \quad (4.33)$$

$$\phi(\mathbf{x}) = -\frac{OD(\mathbf{x})}{2} \frac{2\Delta/\Gamma}{1 + (2\Delta/\Gamma)^2} \quad (4.34)$$

Now, let's assume the imaging setup is not focused, meaning the CCD image plane is not located where the atoms are but is located at a distance D from the atoms. Figure 4.13 sketches this situation. Therefore, the intensity profile measured by the CCD must depend on this difference. To calculate the probe's electric field through the defocused setup, we propagate in free space the probe's field according to the Fresnel propagator defined as [36]:

$$P_D(\mathbf{x}) = \frac{1}{i\lambda D} \exp\left(i\frac{\pi}{\lambda D} |\mathbf{x}|^2\right), \quad (4.35)$$

Finally, we record the resultant intensity pattern at position D in the CCD sensor after a magnification factor. We can express the intensity pattern as the convolution of $E_{atoms}(\mathbf{x})$ and the Fresnel propagator:

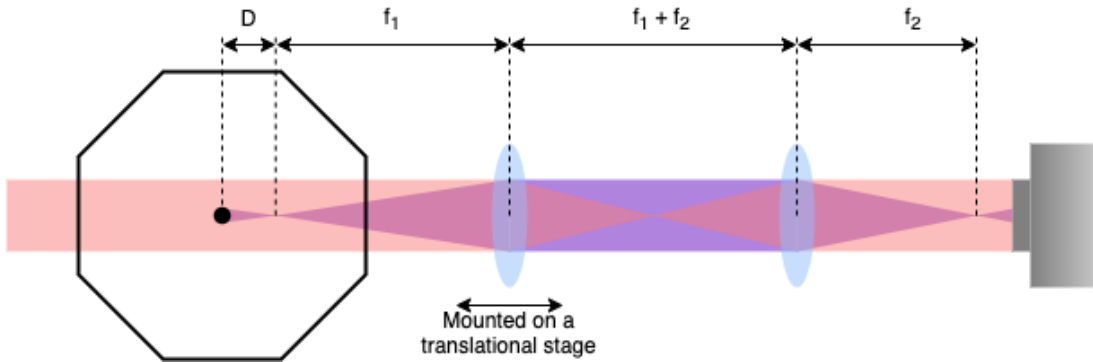


Figure 4.13: Scheme of the shadowgraphy focusing technique. The atoms are located at a distance D from the image plane of the CCD. The first lens of the imaging setup is able to move along the probe's direction to minimize the distance D .

$$I_D(\mathbf{x}) = \frac{c\epsilon_0}{2} |E(\mathbf{x}) \otimes P_D(\mathbf{x})|^2, \quad (4.36)$$

where the symbol \otimes denotes the convolution operator. This propagation becomes simpler when considered in Fourier space. Using the convention $\tilde{g}(\mathbf{f}) = \int g(\mathbf{x}) e^{-2\pi i \mathbf{x} \cdot \mathbf{f}} d\mathbf{x}$, the intensity in Fourier space is:

$$\tilde{I}_D(\mathbf{f}) = \frac{c\epsilon_0}{2} \int E\left(\mathbf{x} - \frac{\lambda D}{2} \mathbf{f}\right) E^*\left(\mathbf{x} + \frac{\lambda D}{2} \mathbf{f}\right) e^{-2\pi i \mathbf{x} \cdot \mathbf{f}} d\mathbf{x}. \quad (4.37)$$

Considering small values of D , the resultant field can be approximated using a Taylor expansion as:

$$E\left(\mathbf{x} \pm \frac{\lambda D}{2} \mathbf{f}\right) \approx E(\mathbf{x}) \pm \frac{\lambda D}{2} \mathbf{f} \cdot \nabla E(\mathbf{x}). \quad (4.38)$$

Using this approximation in (4.36), and taking it's inverse Fourier transform to obtain the intensity field at the CCD position:

$$I_D(\mathbf{x}) = \frac{c\epsilon_0}{2} |E|^2(\mathbf{x}) - \frac{c\epsilon_0}{2} \frac{\lambda D}{2\pi} \nabla \cdot [|E|^2(\mathbf{x}) \nabla \phi(\mathbf{x})], \quad (4.39)$$

hence,

$$I_D(\mathbf{x}) = I_0(\mathbf{x}) t^2(\mathbf{x}) - \frac{\lambda D}{2\pi} [I_0(\mathbf{x}) t^2(\mathbf{x}) \nabla^2 \phi(\mathbf{x}) - \nabla(I_0(\mathbf{x}) t^2(\mathbf{x})) \cdot \nabla \phi(\mathbf{x})]. \quad (4.40)$$

This expression takes into account the absorption effects of the cloud. However, we can ignore these effects performing imaging far from resonance. In this case, the signal is proportional to the second derivative of the phase, hence the column density [46]:

$$I_D(\mathbf{x}) = I_0(\mathbf{x}) \left(1 - \frac{\lambda D}{2\pi} \nabla^2 \phi(\mathbf{x}) \right). \quad (4.41)$$

This dispersive imaging technique is called shadowgraph imaging and can be implemented to achieve non-destructive imaging[14]. As shown in equation (4.41), the signal's contrast is proportional to the defocused distance D . Consequently, the dispersive signal vanishes when the atoms are precisely on focus. Hence, we can use this imaging technique to focus the optical system. This step is crucial for the experiment. The vertical imaging setup depth of field is around $3\mu\text{m}$, meaning we need to position the objective with high precision, and this method allows us to reach such

precision levels. More importantly, focusing the imaging setup allows us to achieve higher resolutions.

Ideally, we would use a far detuned probe beam to acquire the dispersive signal. Nonetheless, the SNR for large detuning is very low. For this reason, we'll use a not so far-detuned probe beam to acquire the dispersive signals. Figures 4.14 a and b show an example of such images taken with a detuning of $\Delta \approx 3\Gamma$. Figures 4.14 a and b show different density profiles (2D and 1D respectively) taken at different objective positions. As shown in figure 4.13 and section 3.2.3, the objective has the ability to be translated along the probe's optical path. In this case, we need to use equation (4.40) instead of (4.41), since there are absorption effects. It is worth notice that for a flat imaging probe beam, *i.e.* $I_0(\mathbf{x}) \approx I_0$, equation (4.40) reads:

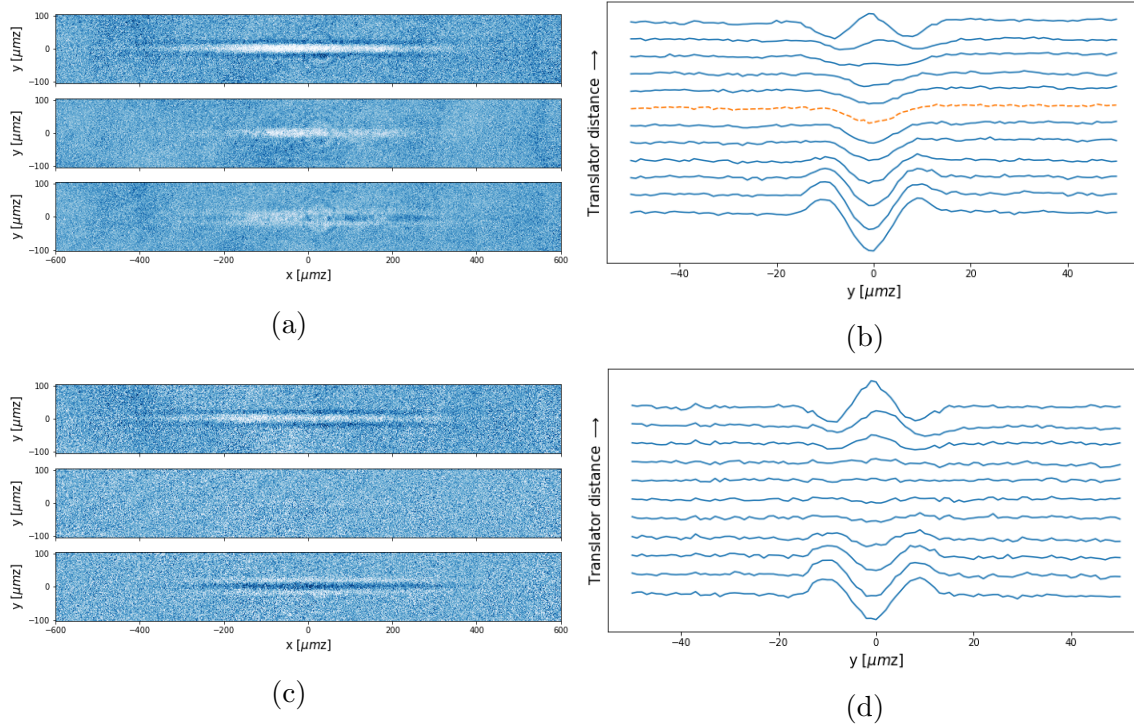


Figure 4.14: a) Non-resonant absorption images acquired before, on, and after the imaging setup focus. b) Integrated radial profiles for various objective positions, see figure 4.13. c) Resultant images after subtracting the focused image. d) Integrated radial profiles of the resultant images.

$$I_D(\mathbf{x})/I_0 = t^2(\mathbf{x}) - \frac{\lambda D}{2\pi} [t^2(\mathbf{x})\nabla^2\phi(\mathbf{x}) - \nabla t^2(\mathbf{x}) \cdot \nabla\phi(\mathbf{x})], \quad (4.42)$$

we can simplify this expression by considering a constant probe detuning and atomic

density for all images:

$$I_D(\mathbf{x})/I_0 = f(\mathbf{x}) - \beta g(\mathbf{x}), \quad (4.43)$$

where, in principle, $f(\mathbf{x})$ and $g(\mathbf{x})$ are the same functions for all images, and $\beta = \frac{\lambda D}{2\pi}$. Additionally, we can reduce the problem's dimensionality by integrating the density profiles along the axial direction, as shown in figure 4.14c and d.

Formulating the not so far-detuned focusing process as suggested by equation (4.43), makes it more practical to implement. In figure 4.14, the orange-dashed profile corresponds to the function $f(\mathbf{x})$, while the rest of the profiles correspond to non-trivial values of β of equation (4.43). Physically, $f(\mathbf{x})$ represents the optical density profile, while $g(\mathbf{x})$ represents the distortions effects caused by the defocused imaging setup.

To find the profile corresponding to $\beta = 0$, we proceed by exhaustive trial and error. We select a candidate profile and subtract it from the rest of the images, see figure 4.14c and d. Next, we check if the resultant profiles are proportional to each other for all positions across the image. If that is the case, we found the corresponding profile with $\beta = 0$. If not, we try with another candidate.

4.3.2. Post-processing: Fringe Removal Algorithm

In the standard procedure of absorption imaging, we take three images in every run of the experiment, figure 4.3. Ideally, both the atomic signal and the probe have the same beam distribution, except where the sample is, including the beam profile, the defects on the beam profile, and the interference fringes from optical elements. However, mechanical vibrations and frequency changes in the probe light can cause additional interference fringes in the optical density calculation. Moreover, the interference fringes in the imaging beam may move a little and change their phase [47–50].

We can take advantage of this effect to improve the SNR of the image in the following fashion. First, we need to generate multiple pairs of absorption and reference images with the same experimental conditions. If a pair of images produces interference fringes in the optical density, then it might be possible that choosing a different reference image from the set may not cause such interference fringes. Effectively, producing a smooth background, hence increasing the SNR of the image. We can extend this idea to create an artificial reference image that almost exactly matches

the absorption image background.

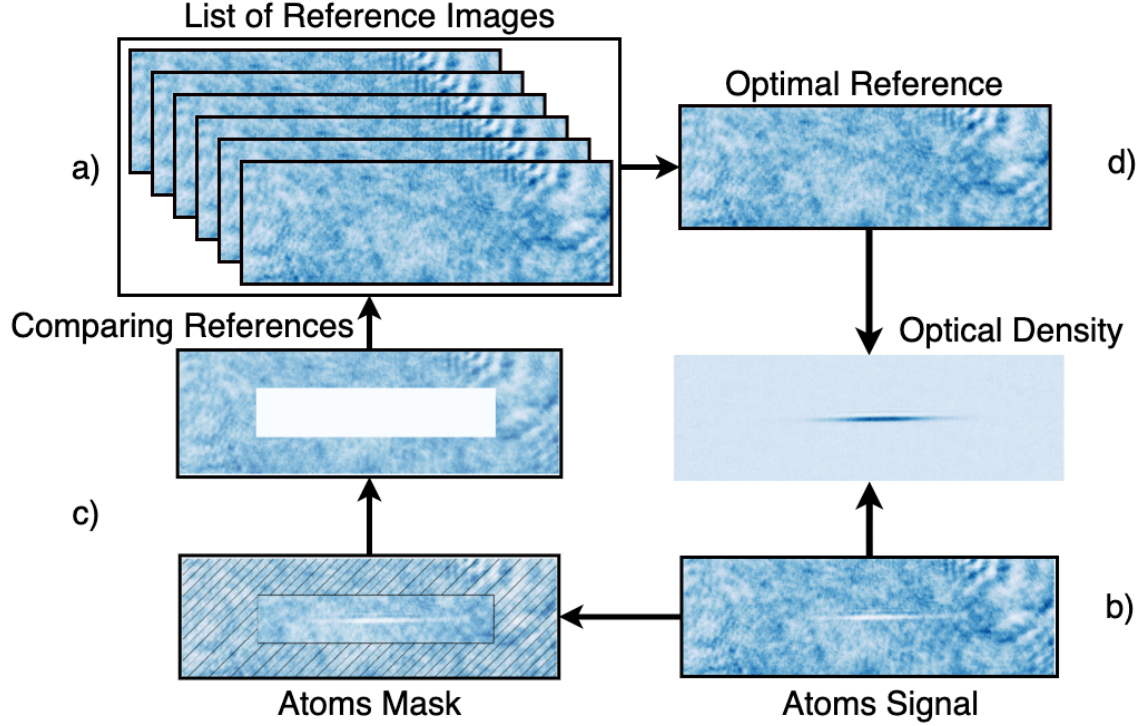


Figure 4.15: Flow diagram of the fringe removal algorithm. a) We generate a set of reference images with the same experimental conditions. b) From the atomic signal, we create the mask where the atoms are. c) We mask the sample region, leaving only the background for the rest of the procedure. d) We create the linear combination projecting the background to the list of reference images.

The idea of the Fringe Removal Algorithm (FRA) is to construct the optimal reference image, C_{opt}^{probe} , for a given absorption image. To generate it, we use a linear combination of reference images taken with identical parameters, denoted as C_k^{probe} , see figure 4.15 a). Therefore,

$$C_{opt}^{probe}(\mathbf{x}) = \sum_k a_k C_k^{probe}(\mathbf{x}), \quad (4.44)$$

where a_k is the weight of the k -th reference image. To obtain the value of a_k , we minimize using the least-squares difference between the absorption background signal and reference images [47]:

$$\sum_{\mathbf{x} \in \mathcal{B}} \left(C^{atoms}(\mathbf{x}) - C_{opt}^{probe}(\mathbf{x}) \right) = \sum_{\mathbf{x}} m_{\mathbf{x}} \left(C^{atoms}(\mathbf{x}) - C_{opt}^{probe}(\mathbf{x}) \right), \quad (4.45)$$

where \mathcal{B} is the background region, and $m_{\mathbf{x}}$ is a mask determining its position, see figure 4.15 c).

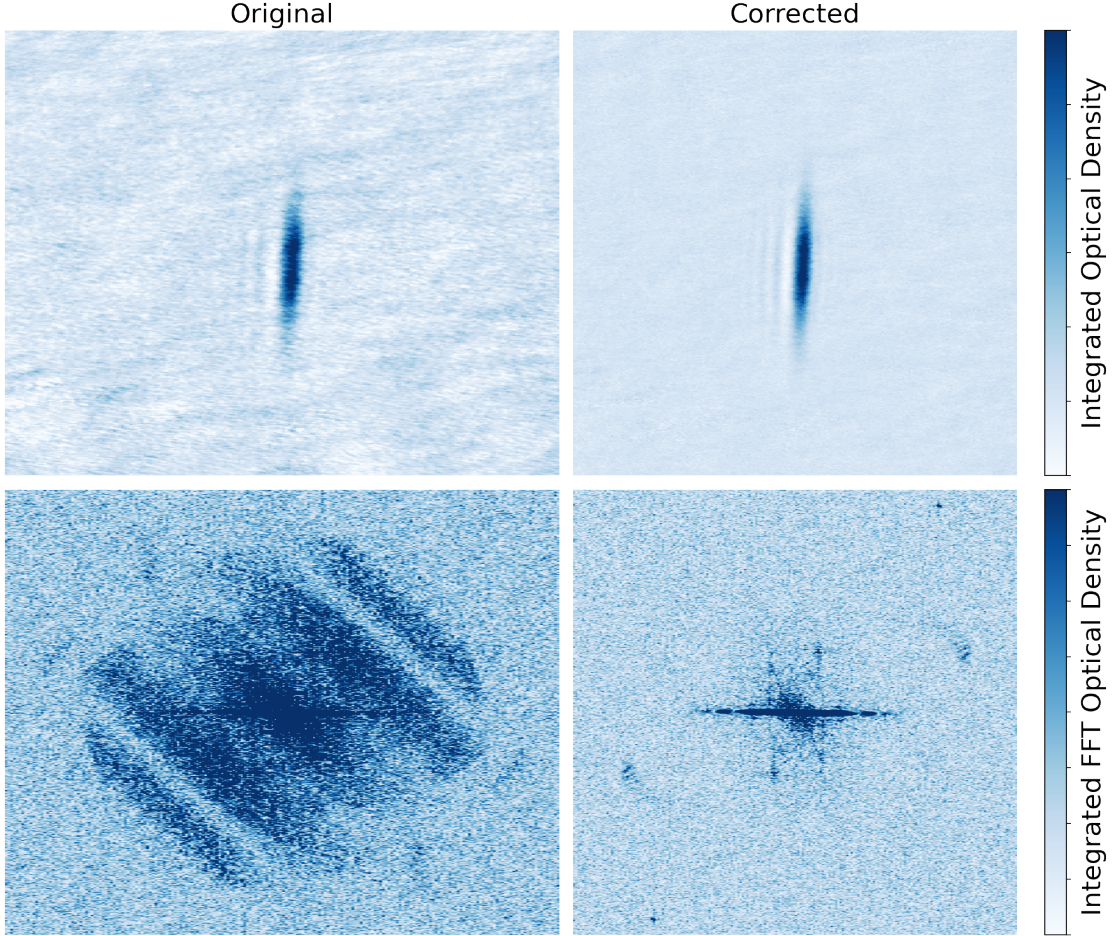


Figure 4.16: A comparison between Left panels: the original optical density, and its Fourier Transform, and Right panels: the optical density calculated using the optimal reference image, and its Fourier Transform.

To obtain the values of a_k we proceed variationally, setting partial derivatives with respect to a_k to zero. In this manner, we obtain the set of linear equations that we must solve [47]:

$$\sum_k a_k B_{k,l} = \sum_{\mathbf{x}} m_{\mathbf{x}} C_l^{probe}(\mathbf{x}) C^{atoms}(\mathbf{x}), \quad (4.46)$$

where the matrix B is defined as:

$$B_{k,l} = \sum_{\mathbf{x}} m_{\mathbf{x}} C_k^{probe}(\mathbf{x}) C_l^{probe}(\mathbf{x}). \quad (4.47)$$

We can solve (4.46) using linear algebra techniques, involving the calculation of the inverse matrix of B . In addition to the inversion of B , the matrix's construction is the most costly computationally since it depends greatly on the number of reference images we use and the number of pixels. Other methods like Gram-Schmidt orthonormalization [50] are used to generate a set of linearly independent pseudo reference images. This method improves the time to calculate the matrix B . Likewise, methods more complex like principal component analysis [48] speed up this significantly. However, the time to compute B in our case is not a problem since the typical number of reference images we use is around 100.

A comparison between the standard optical density (and its Fourier Transform) and the optical density calculated using the optimal reference image is shown in figure 4.16. The difference between these images is dramatic. Almost all high-frequency fluctuations of the background are removed, see the Fourier Transform, increasing the SNR of the image.

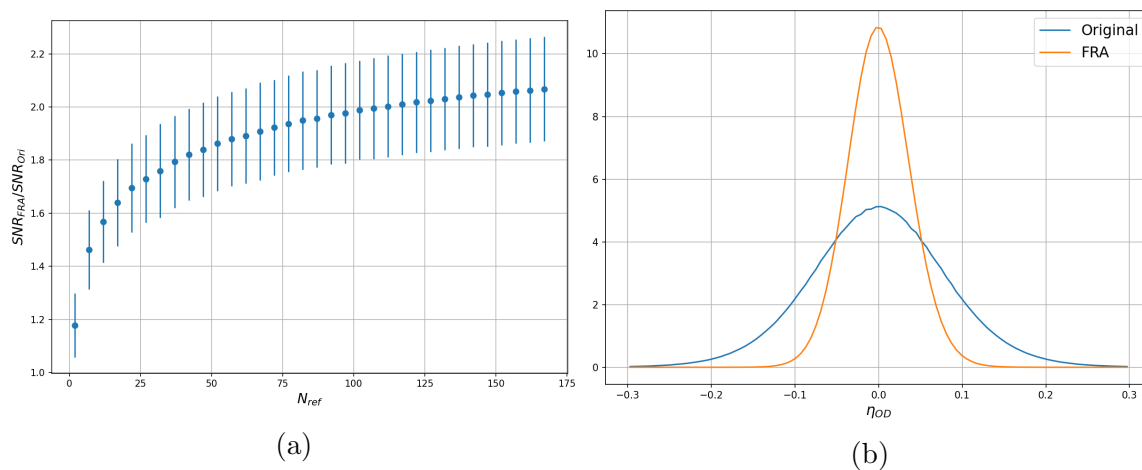


Figure 4.17: a) SNR as a function of the number of reference images in the set. b) Optical density noise distribution before (blue) and after (orange) the FRA correction.

Figure 4.17a shows the SNR increase as a function of the number of images in the reference list. To produce this result, we use N_{ref} random images selected from a sample of 170 images to generate the B matrix. Then, we apply the FRA algorithm to all 170 images. Next, we compare the SNR of the original optical density to the SNR of the optical density using the FRA. The error bars in figure 4.17a correspond to the standard deviation of 10 iterations of this procedure. The SNR improvement increases logarithmically with the number of images in the list. Therefore, to improve

the SNR by a factor of 2 on all 170 images, we only need 75 reference images in the set. Moreover, we estimated the background optical density noise distribution before and after applying the FRA algorithm with all 170 reference images to construct the B matrix. As shown in figure 4.17b, the standard deviation of the noise distribution reduces by a factor of two, according to the increase of the SNR signal.

4.4. Phase contrast imaging

Phase-contrast imaging (PCI) allows us to acquire multiple measurements of the same sample, in situ, in a non-destructive way [2, 5]. This technique has proven to be useful for studying the condensate dynamics, such as vortex arrays [51, 52], the time evolution of a space crystal [53–55]. This imaging method is capable of measuring a high optical density condensate providing information about the thermodynamic properties of cloud [6, 56]. Moreover, it is particularly useful for characterizing imbalanced systems such as strongly interacting imbalanced Fermi gases [57–61].

In absorption imaging, we recorded the cloud’s shadow on the probe beam, from which we extracted the optical density, hence the column density distribution. The method’s working principle is the spontaneous scattering of photons by the atoms. This process causes the atomic sample to heat up significantly. The scattering heating rate can be modeled by (4.10), $\langle \Delta T \rangle_{st} = 2\tau T_{rec} R_\alpha$. The probe beam must be far-detuned from resonance to overcome the heating. However, for nonzero detuning, the real part of the index of refraction of the atoms becomes nonzero, and the cloud behaves like a lens. The lensing effect occurs because the cloud induces a spatial phase shift in the probe beam, making it focus or diverge depending on the detuning’s sign. Detuning the probe beam further decreases the phase shift $\phi \propto 1/\Delta$, with the advantage that the spontaneous scattering $R_\alpha \propto 1/\Delta^2$ vanishes more rapidly. Additionally, increasing the detuning such that the refraction is small, but the phase shift remains measurable is the PCI principle. This technique allows us to measure directly the real part of the index of refraction. PCI can be used to image in a nondestructive way since the number of scattered photons becomes negligible for large detuning.

4.4.1. Imaging the phase

Absorption imaging measures the optical density, meaning it probes the imaginary part of the atomic cloud complex index of refraction \mathcal{N} . In contrast, PCI probes the real part of \mathcal{N} . Currently, this technique is widely used in phase-contrast microscopes, developed by Zernike in 1933 [62] who was later awarded with the Nobel Prize for his invention.

Writing the probe beam electric field as $E_{probe}(\mathbf{x})$, after passing a cloud of atoms, the electric field is:

$$E(\mathbf{x}) = E_{probe}(\mathbf{x}) + E_{atoms}(\mathbf{x}) = E_{probe}(\mathbf{x}) + E_{probe}(\mathbf{x}) (e^{i\phi_{atoms}(\mathbf{x})} - 1), \quad (4.48)$$

where $E_{atoms}(\mathbf{x})$ represents the part diffracted by the atoms and $E_{probe}(\mathbf{x})$ the part not diffracted. The image acquired by a CCD camera is the intensity of this electric field, that is $I = \frac{c\epsilon_0}{2}|E|^2 = I_0 e^{-Im(\phi_{atoms})} = I_0 e^{-OD}$. Using this scheme, the real phase term is lost, making the absorption the only measured quantity. In resemblance with Zernike's phase-contrast microscope [62], the accumulated phase is converted into an intensity profile by phase-shifting the non-diffracted light. The non-diffracted light can be phase-shifted by placing a transparent object with a different optical path than where the diffracted beam passes. This object will be called a phase spot, more clearly seen in figure 4.18. The phase spot consists of a Fused Silica wafer with a dimple located at the center, fabricated by SILIOS. The dimple has a diameter of $200\mu\text{m}$ with $368(5)\text{nm}$ depth. Light propagating through the dimple accumulates an effective phase-shift of $\pi/2$ with respect to the light propagating through the rest of the plate. Hence, the non-diffracted light accumulates a phase θ , changing the electric field arriving at the CCD camera:

$$E(\mathbf{x}) = E_{probe}(\mathbf{x})e^{i\theta} + E_{probe}(\mathbf{x}) (e^{i\phi_{atoms}(\mathbf{x})} - 1). \quad (4.49)$$

The intensity in this case is:

$$I(\mathbf{x}) = I_0(\mathbf{x}) [2 + t^2(\mathbf{x}) + 2t(\mathbf{x}) \cos(\theta - \phi(\mathbf{x})) - 2 \cos \theta - 2t(\mathbf{x}) \cos \phi(\mathbf{x})]. \quad (4.50)$$

where $t(\mathbf{x})$ and $\phi(\mathbf{x})$ are the transmittance and the phase shift functions, defined in terms of the complex phase ϕ_{atoms} as:

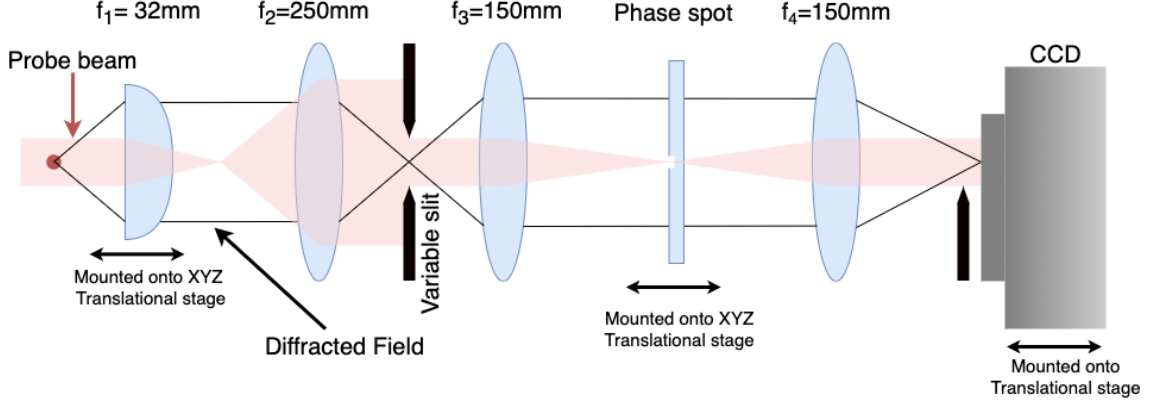


Figure 4.18: Scheme of the PCI setup. The phase spot is aligned in the focal plane of the non-diffracted probe beam. Light propagating through the dimple accumulates an effective phase-shift of $\pi/2$ with respect to the light propagating through the rest of the plate.

$$\begin{aligned}
 t(\mathbf{x}) &= \exp(-\text{Im } \phi_{atoms}(\mathbf{x})), \\
 \phi(\mathbf{x}) &= \text{Re } \phi_{atoms}(\mathbf{x}).
 \end{aligned}
 \tag{4.51}$$

For our phase spot, the phase-shift between the probe field and the diffracted field is $\theta = \pi/2$. Hence the intensity is:

$$I(\mathbf{x}) = I_0(\mathbf{x}) \left[2 + t^2(\mathbf{x}) + 2\sqrt{2}t(\mathbf{x}) \sin\left(\phi(\mathbf{x}) - \frac{\pi}{4}\right) \right].
 \tag{4.52}$$

Considering the case when the probe beam is far-detuned, meaning no noticeable absorption effects ($t(\mathbf{x}) \approx 1$), and for small phase-shift, the PCI signal is:

$$I(\mathbf{x}) \approx I_0(\mathbf{x})(1 + 2\phi(\mathbf{x}) + \phi^2(\mathbf{x})) \approx I_0(\mathbf{x})(1 + \phi(\mathbf{x}))^2.
 \tag{4.53}$$

Therefore, we can either approximate the phase-shift to first or second order:

$$\phi^{(1)}(\mathbf{x}) \approx \frac{1}{2} \left(\frac{I(\mathbf{x})}{I_0(\mathbf{x})} - 1 \right),
 \tag{4.54}$$

$$\phi^{(2)}(\mathbf{x}) \approx \sqrt{\frac{I(\mathbf{x})}{I_0(\mathbf{x})}} - 1.
 \tag{4.55}$$

Figure 4.19a shows the comparison between the real phase-shift caused by the

atoms as a function of the probe detuning (see (4.62)), and both approximations to the phase-shift from a simulated PCI image.

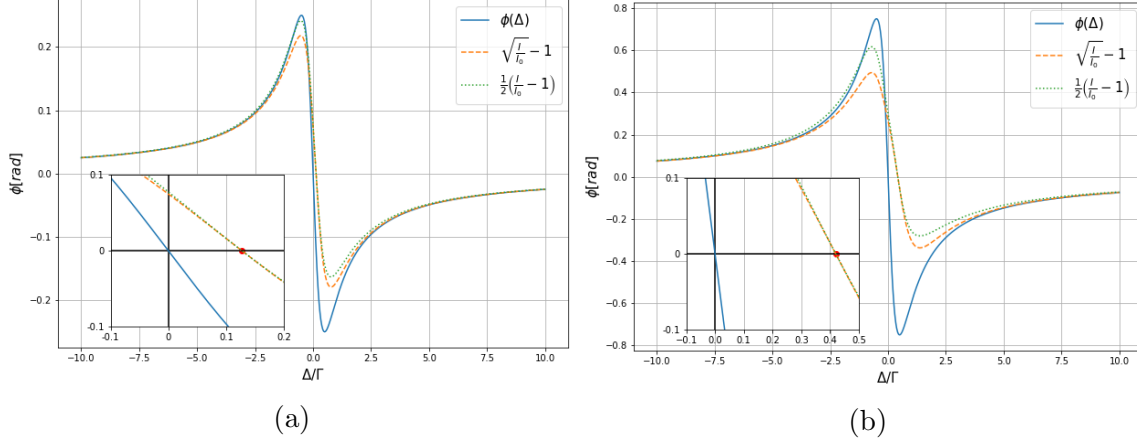


Figure 4.19: a) Comparison between (continuous blue) the real phase-shift caused by a cloud with $OD = 1$, see (4.62). (dashed orange) Phase calculated with (4.54), and (dotted green) Phase calculated with (4.55). Inset: Close up in the resonance region, there is a shift in the zero-shift position of $\approx 0.127\Gamma$ marked by the red dot.

b) Same as a) but with $OD = 3$, in this case the zero-shift position is $\approx 0.42\Gamma$.

As shown in figure 4.19a, for a cloud with an optical density equal to 1, the approximation to first-order (4.55) reproduce more faithfully the real phase-shift for negative detunings than the calculated with (4.54). In contrast, for positive detuning, the second-order approximation is closer to the real phase-shift. However, both approximations are notably far from the truth phase value. This discrepancy arises from the assumption that no absorption effects are present. Figure 4.19b shows the same calculation as figure 4.19a but for a cloud with an optical density equal to 3. In this case, the deviation is much greater near resonance. For large detunings, $\Delta > 2.5\Gamma$ ($OD = 1$) and $\Delta > 6\Gamma$ ($OD = 3$), both approximations reproduce the phase value, since for those regions, there are no absorption effects.

To relate the phase-shift to the atomic density, we require to express the atom's polarizability as a function of the probe properties. We consider the low-intensity limit where the atom's polarizability is given by [63]:

$$\alpha = \frac{\epsilon_0 \sigma_0 c}{\omega} \left(\frac{i}{1 + (2\Delta/\Gamma)^2} - \frac{2\Delta/\Gamma}{1 + (2\Delta/\Gamma)^2} \right). \quad (4.56)$$

Figure 4.20a shows the real and imaginary parts of α as a function of the detuning Δ . The real part of the polarizability is zero at resonance, where the imaginary part

has its maximum value. Notice the decay of both functions for large detuning: $\text{Re } \alpha \approx 1/\Delta$, while $\text{Im } \alpha \approx 1/\Delta^2$.

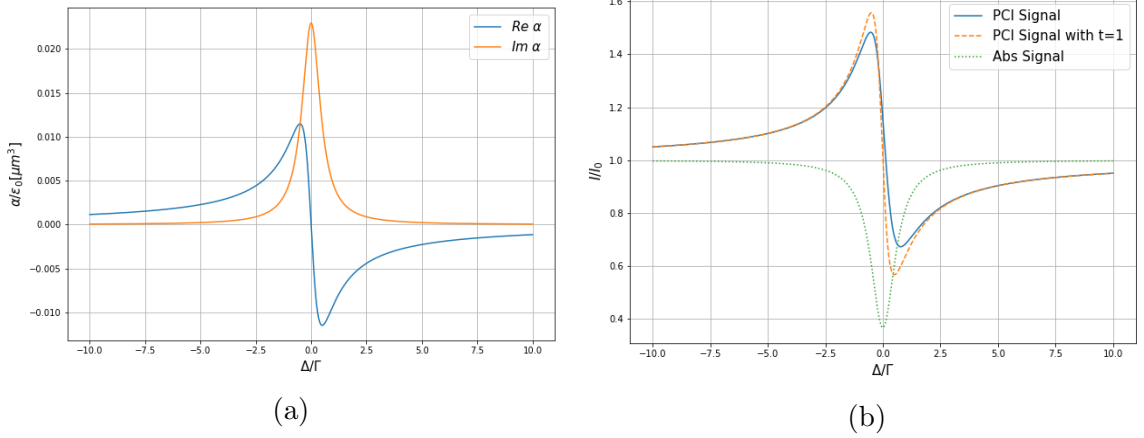


Figure 4.20: a) Real and imaginary parts of the polarizability. b) I/I_0 signals with an optical density equal to 1. PCI signal (4.52) (continuous blue), PCI signal assuming no absorption effects (dashed orange), relation (4.52) using $t=1$; and the low-intensity approximation of the absorption signal (4.18) (dotted green). The curve without absorption effects closely matches the curve with absorption effects for detunings $|\Delta| > 2.5\Gamma$.

Finally, the complex index of refraction \mathcal{N} is given by [30]:

$$\mathcal{N}^2 = 1 + \frac{n\alpha}{\epsilon_0}, \quad (4.57)$$

where n is the atomic density. The index of refraction (4.57) is only valid for low densities. For higher densities, like in a BEC, the atom's dipole moment is influenced by the surrounding atom's dipole moments. To account for this effect, we use the Lorentz-Lorenz equation [64]. Hence the modification of the refractive index is [65]:

$$\mathcal{N}^2 = 1 + \frac{n\alpha}{\epsilon_0} \frac{1}{1 - \frac{1}{3}n\alpha/\epsilon_0}. \quad (4.58)$$

The complex phase and the column density are related to the complex index of refraction. This relation is explicit when considering the probe beam passing through the atomic cloud with an index of refraction \mathcal{N} . The probe beam accumulates a complex phase given by:

$$\phi_a(x, y) = k \int (\mathcal{N}(x, y, z) - 1) dz, \quad (4.59)$$

where $k = 2\pi/\lambda$. Under normal experimental conditions, the ratio $n\alpha/\epsilon_0$ is very small, in the order of 10^{-3} . Therefore, we approximate the index of refraction as:

$$\mathcal{N}(x, y, z) \approx 1 + \frac{n(x, y, z)\alpha}{2\epsilon_0} = 1 + \frac{\sigma_0 n \lambda}{4\pi} \left(\frac{i}{1 + (2\Delta/\Gamma)^2} - \frac{2\Delta/\Gamma}{1 + (2\Delta/\Gamma)^2} \right). \quad (4.60)$$

Now, the complex phase induced the probe beam is written as:

$$\phi_a(x, y) = \frac{k\alpha}{2\epsilon_0} n_c(x, y) = \frac{\sigma_0 n_c(x, y)}{2} \left(\frac{i}{1 + (2\Delta/\Gamma)^2} - \frac{2\Delta/\Gamma}{1 + (2\Delta/\Gamma)^2} \right), \quad (4.61)$$

where $n_c(x, y)$ is the column density. Using the complex phase (4.61), we can calculate the phase-shift and the transmittance functions (4.51):

$$\begin{aligned} t(\mathbf{x}) &= e^{-\frac{\sigma_0 n_c}{2} \frac{1}{1 + (2\Delta/\Gamma)^2}}, \\ \phi(\mathbf{x}) &= -\frac{\sigma_0 n_c}{2} \frac{2\Delta/\Gamma}{1 + (2\Delta/\Gamma)^2}. \end{aligned} \quad (4.62)$$

We recall these functions from the previous section.

Figure 4.20b shows the comparison between the PCI signal, the approximation of the PCI signal where no absorption effects are present, and the low-intensity absorption imaging signal. As expected, the absorption signal is a narrow peak centered at resonance. For large detunings, no absorption is noticeable, making the absorption imaging technique useless in this region. In contrast, we still appreciate the PCI signal for detunings greater than 5Γ . The assumption of no absorption effects is valid for large detunings, $|\Delta| > 2.5\Gamma$.

For the quantum gases of ${}^6\text{Li}$, we usually use a mixture of states $|1\rangle$ and $|2\rangle$ (and possibly $|3\rangle$). For this reason, we consider the mixture's phase-shift and the transmittance functions defined as:

$$\begin{aligned} t(\mathbf{x}) &= t_{|1\rangle}(\mathbf{x}) t_{|2\rangle}(\mathbf{x}) = e^{-\frac{\sigma_0 n_c^{(1)}}{2} \frac{1}{1 + (2\Delta^{(1)}/\Gamma)^2}} e^{-\frac{\sigma_0 n_c^{(2)}}{2} \frac{1}{1 + (2\Delta^{(2)}/\Gamma)^2}}, \\ \phi(\mathbf{x}) &= \phi_{|1\rangle}(\mathbf{x}) + \phi_{|2\rangle}(\mathbf{x}) = -\frac{\sigma_0 n_c^{(1)}}{2} \frac{2\Delta^{(1)}/\Gamma}{1 + (2\Delta^{(1)}/\Gamma)^2} - \frac{\sigma_0 n_c^{(2)}}{2} \frac{2\Delta^{(2)}/\Gamma}{1 + (2\Delta^{(2)}/\Gamma)^2}, \end{aligned} \quad (4.63)$$

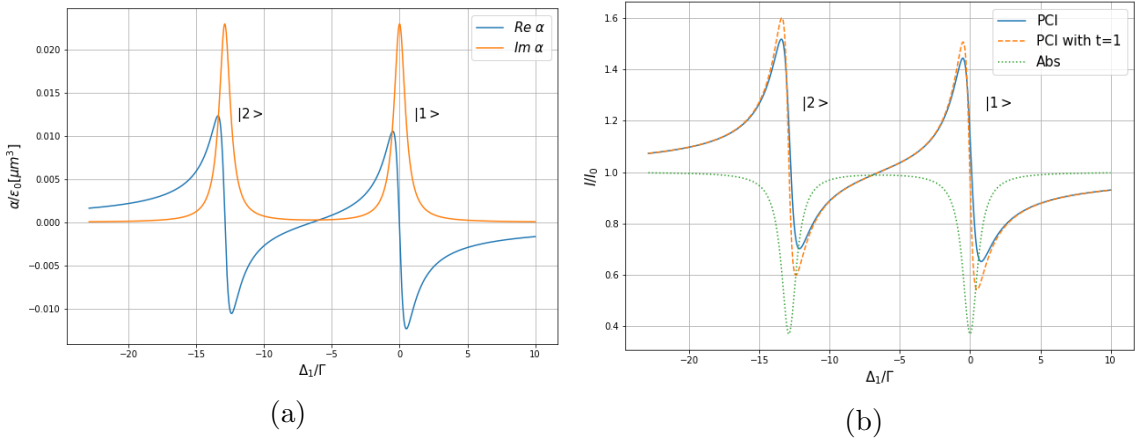
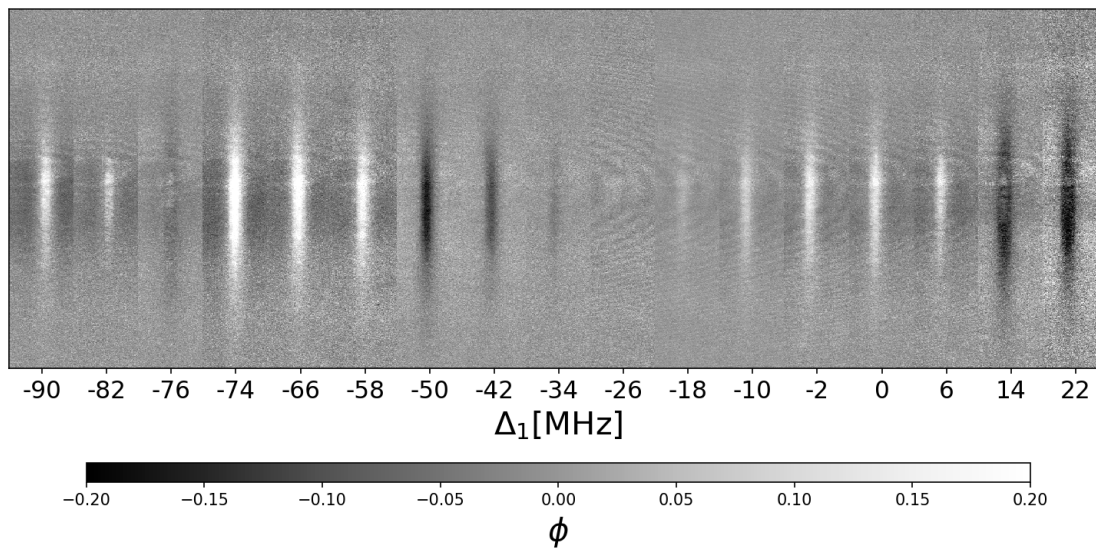


Figure 4.21: a) Real and imaginary parts of the polarizability and b) I/I_0 signals for a balanced mixture of states $|1\rangle$ and $|2\rangle$ with optical density per state equal to 1. PCI signal (continuous blue), PCI signal assuming no absorption effects (dashed orange), and the low-intensity approximation of the absorption signal (dotted green).

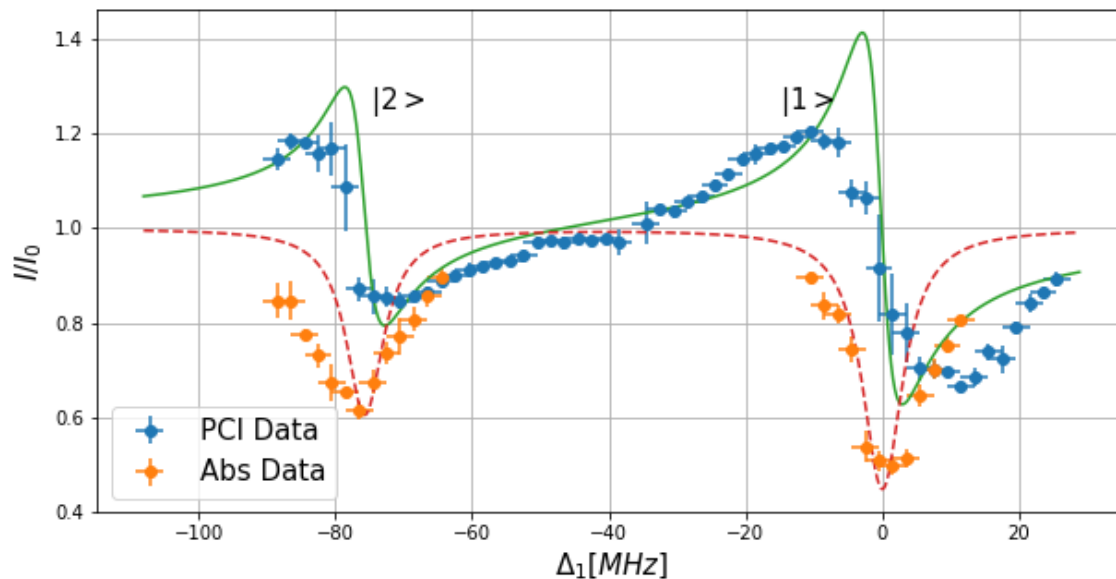
where $\hbar\Delta_{|2\rangle-|1\rangle} = \hbar(\Delta_{|2\rangle} - \Delta_{|1\rangle})$ is the energy difference between the states $|1\rangle$ and $|2\rangle$. For magnetic fields above 100G, well within the Paschen Back regime where the hyperfine splitting is nearly constant, we can approximate $\Delta_{|2\rangle-|1\rangle} \approx 12.89\Gamma = 2\pi \times 75.66$ MHz. Figure 4.21a shows the polarizability of an equal mixture of states $|1\rangle$ and $|2\rangle$. The imaginary part of the polarizability, responsible for the absorption effects, has two clear peaks located at the resonance of either state $|1\rangle$ or $|2\rangle$. The real part of the polarizability behaves similarly to the one-state polarizability, except between both states. For a balanced mixture, the real part of the polarizability reaches zero when $\Delta_1 = -\Delta_2 = \frac{1}{2}\Delta_{|2\rangle-|1\rangle}$. For this detuning, the phase signal is lost completely. The phase-shift induced by each state into the probe beam balance out. This result is more clear in figure 4.21b, where the PCI signal becomes unity.

Figure 4.21b, shows the same comparison as figure 4.20b. In this case, we show that the region between both states is well described by the assumption that no absorption effects are present. If we realize the imaging in this region, we can distinguish both states by their PCI signal. For instance, state $|1\rangle$ will appear brighter than the background, while state $|2\rangle$ will appear darker, as shown in figure 4.22a.

Figure 4.22a shows some examples of PCI images as a function of the imaging frequency. As expected, close to the resonance of both $|1\rangle$ and $|2\rangle$ states the signal is the highest, while the signal where $\Delta_1 = -\Delta_2 = \frac{1}{2}\Delta_{|2\rangle-|1\rangle}$ is close to zero. To



(a)



(b)

Figure 4.22: a) Phase-contrast images obtained at different frequencies. The detuning is shown with respect to state $|1\rangle$. From left to right, we see an oscillation in the signal sign. This effect corresponds to the phase sign. b) Comparison between absorption and phase-contrast experimental data. The data points correspond to experimental data, while the continuous and dashed curves correspond to the expected PCI signal using (4.63), and the expected absorption signal, for an imbalance mixture of $OD_{|1\rangle} = 1$ and $OD_{|2\rangle} = 0.8$.

characterize the PCI signal, we realize a gaussian fit and plotted the amplitude results as a function of the imaging frequency in figure 4.22b. Figure 4.22b, shows the comparison between the absorption and phase-contrast imaging techniques. For comparison, we plotted the curves of figure 4.21b for an imbalance mixture of $OD_{|1\rangle} = 1$ and $OD_{|2\rangle} = 0.8$. The shape of the profiles is broader than the expected lineshapes, this may be caused by intensity broadening during the imaging process. Although, we see a qualitative agreement between experiment and theory.

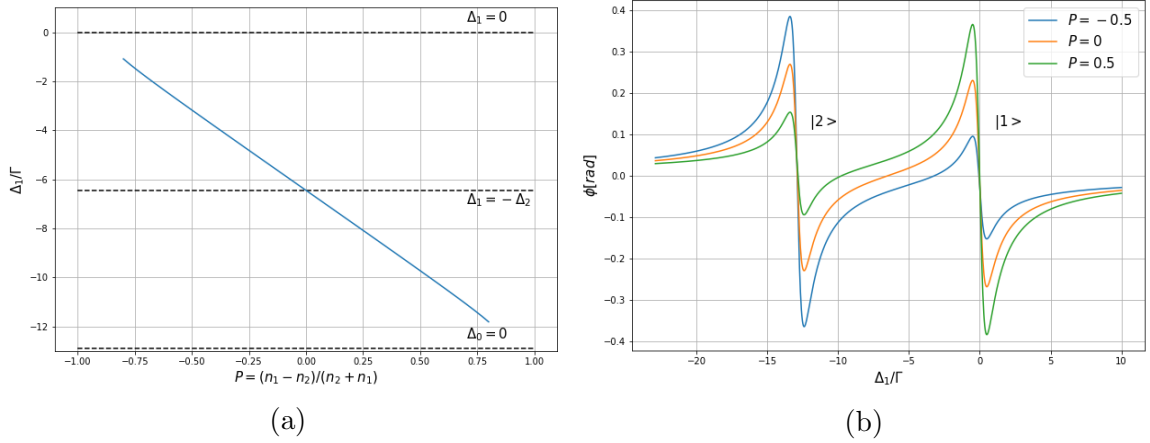


Figure 4.23: a) Detuning where the net phase-shift becomes zero as a function of the polarization of the mixture, $P = (n_1 - n_2)/(n_2 + n_1)$. b) Examples of the phase-shift for different mixture polarization's.

The frequency where the net phase-shift becomes zero can be calculated as a function of the mixture polarization defined as:

$$P = \frac{n_{|1\rangle} - n_{|2\rangle}}{n_{|2\rangle} + n_{|1\rangle}}, \quad (4.64)$$

where $n_{|i\rangle}$ is the density of state i . Figure 4.23a, shows the crossing frequency as a function of the mixture polarization. As shown, for polarization above $|P| > 0.8$ this method cannot be reliably used, since the crossing point gets close to the states resonance frequency. A linear fit reveals the crossing detuning is $\Delta_{crossing}/\Gamma = -6.445(2) - 6.577(4)P = -\frac{1}{2}\Delta_{|1\rangle-|2\rangle} - 6.577(4)P$.

4.4.2. Large phase distortions

The phase-contrast imaging technique allows us to perform non-destructive imaging under some particular conditions, the two most important being the probe's in-

tensity and detuning. Large detuning and low-intensity are crucial to prevent heating during the probe pulse.

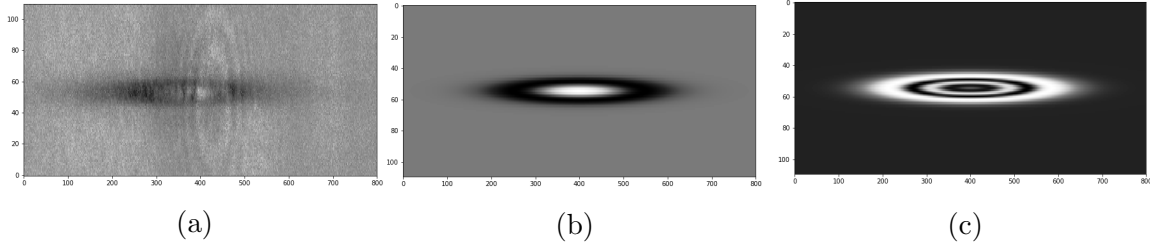


Figure 4.24: PCI large phase distortions. a) Example of the non-linear effects caused by the non-linear nature of the PCI signal, taken with a detuning $\Delta = 2.3\Gamma$. b) Theoretical PCI signal using a sample with $OD = 1$. c) Theoretical example of a severe distortion caused by a high density sample.

Nonetheless, the phase-contrast imaging signal is a non-linear function of the atomic phase, see equation (4.52). Up to this point, we neglected these non-linear effects, approximating the induced phase to be small. However, close to resonance or imaging high optical density samples, we must consider these non-linear effects. In [6], they make use of these non-linear effects to study the thermodynamic properties of a BEC. Figures 4.24a and 4.24b show an example of a PCI image close to resonance, $\Delta = 2.3\Gamma$, and the corresponding theoretical profile using a sample with $OD = 1$. The high density at the trap's center shifts by more than π the probe phase. The periodicity of the PCI signal makes this region appear brighter than the cloud's outer layers. For more dense clouds, the phase shift can be higher than 2π , making the signal oscillate multiple times, as shown in figure 4.24c.

4.4.3. How non-destructive is this imaging technique?

The simple model we obtained in section 4.1 is necessary to evaluate how destructive is this imaging technique. The heating rate we obtained was:

$$\langle \Delta T \rangle_{st} = 2\tau T_{rec} R_\alpha = \tau T_{rec} \Gamma \frac{s_0/\alpha}{1 + s_0/\alpha + (2\Delta/\Gamma)^2}. \quad (4.65)$$

Considering this technique non-destructive would mean that the induced heating

is small compared to the cloud's temperature, $\langle \Delta T \rangle_{st} / T \ll 1$. Therefore:

$$\frac{\langle \Delta T \rangle_{st}}{T} = \frac{T_{rec}}{T} \frac{\tau \Gamma s_0 / \alpha}{1 + s_0 / \alpha + (2\Delta / \Gamma)^2} \ll 1. \quad (4.66)$$

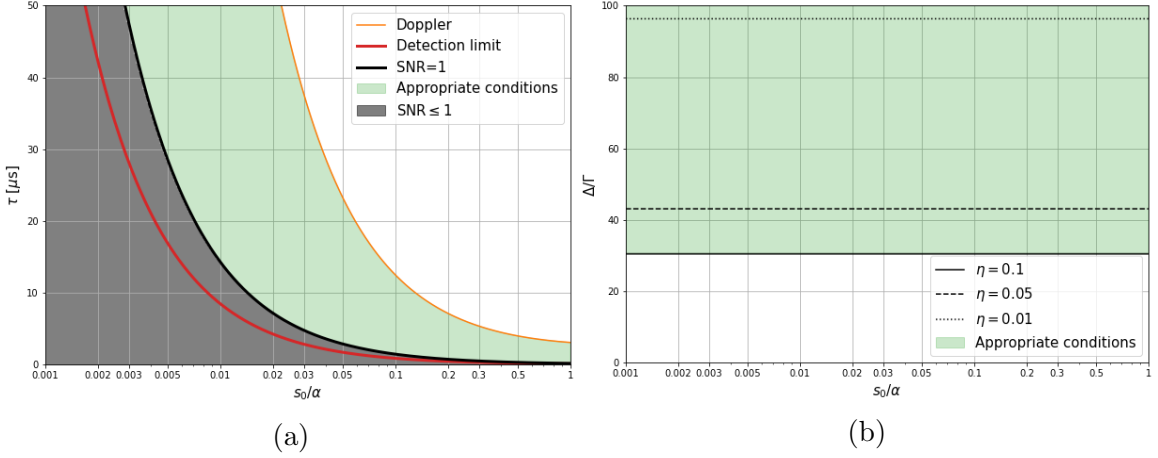


Figure 4.25: a) Appropriate conditions to perform phase-contrast imaging for the probe length τ and the effective saturation parameter s_0/α . b) Appropriate conditions to perform phase-contrast imaging for the detuning Δ/Γ as a function of the effective saturation parameter s_0/α for a sample with temperature $T = 50\text{nK}$. The continuous lines corresponds to $\eta = 0.1$, and the dashed lines to $\eta = 0.05$.

This imposes a condition in the detuning used for imaging. Rearranging the terms in (4.66), and defining $\frac{\langle \Delta T \rangle_{st}}{T} = \eta \ll 1$, we get:

$$\frac{\Delta}{\Gamma} \gg \frac{1}{2} \sqrt{\left(\frac{T_{rec} \tau \Gamma}{\eta T} - 1 \right) s_0 / \alpha - 1}. \quad (4.67)$$

A second condition to meet regards the the fact that the CCD camera must be able to distinguish the probe from background noise. This condition can be stated as:

$$C^{probe} = \chi_{sat} s_0 \tau = \chi_{sat}^* \frac{s_0}{\alpha} \tau > C^{bg}, \quad (4.68)$$

where χ_{sat}^* is the measured constant from sections 4.2.3 and 4.2.3 ($\chi_{sat}^* \approx 236(3)$ counts/ μs). This condition limits the lowest value of s_0/α to:

$$s_0 / \alpha > \frac{C^{bg}}{\chi_{sat}^* \tau}, \quad (4.69)$$

called the detection limit. A third condition to consider regards the SNR, needing to be greater than unity. Finally, in analogy to the absorption imaging a Doppler condition must be constraint, see section 4.2.3.

Figure 4.25 shows the appropriate condition to perform phase-contrast imaging. The first condition to consider is for the effective saturation parameter s_0/α . Lower intensities require longer probing times to obtain the same SNR, as shown in 4.25a. The detection limit, as expected, is always below the SNR condition. Performing imaging below the detection limit is not feasible due to its high count noise in the image.

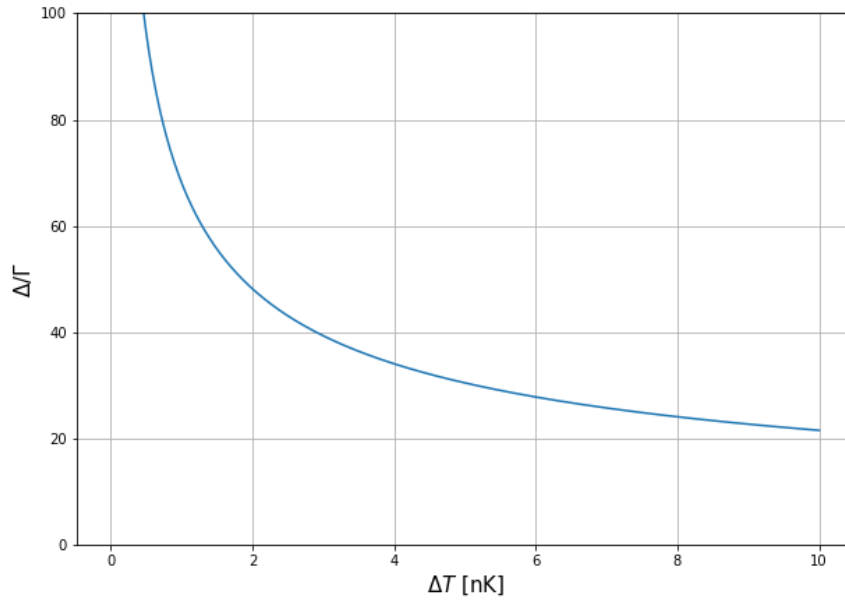


Figure 4.26: Minimum detuning for performing non-destructive imaging as a function of the temperature increase on the cloud using the intensity and probe length from the $SNR = 1$ limit

To determine the range of values for the probe detuning, we'll consider the equality in (4.67). To map the SNR limit, black curve in figure 4.25a, we parametrize the minimum probe duration as a function of the effective saturation parameter. After substitution in equation (4.67) we get the curves shown in figure 4.25b, for different values of η . This curves appear to be independent of the effective saturation parameter, taking into account the corresponding probing time. The curves shown in figure 4.25b show the detuning required to perform phase-contrast imaging with an intensity $I_{sat}s_0/\alpha$ that produce an increase the temperature of ηT .

Taking advantage of the independence of the detuning as a function of the limit

$SNR = 1$. In figure 4.26, we plotted the minimum detuning for imaging as a function of the temperature increase. For high temperature clouds, we can perform non-destructive imaging using lower detunings, since we can allow a higher increasing in temperature. This is not the case for the colder clouds.

Using the current imaging setup along the vertical axis, to perform a high resolution non-destructive phase-contrast imaging we would need to use a probe intensity $I = 0.02I_{sat} \approx 0.05 \text{ mW/cm}^2$, a probe duration of $\tau \gtrsim 8\mu\text{s}$, and a detuning $\Delta = 30.46\Gamma \approx 2\pi \times 178.8 \text{ MHz}$. Using these parameters the cloud's temperature would increase around 5–10% per image taken. This would imply we can perform at most 5 images before the cloud's temperature increases by half the initial temperature.

One way to increase the number of images would be to perform the phase-contrast imaging along the ODT propagation axis. This particular axis has the advantage of having the highest column density, therefore a higher phase-contrast signal. However, imaging along that axis is not yet implemented. The only disadvantage of imaging along that axis, is that only low magnification and low resolution setups can be implemented.

Chapter 5

Conclusions and perspective

5.1. Conclusions

My thesis centered on the experimental implementation and characterization of both destructive and non-destructive imaging techniques for ultracold quantum gases. I developed a new optical setup capable of imaging the atoms with high-resolution ($\approx 2\mu\text{m}$). A crucial step during the imaging procedure is the characterization of the atomic signal. I developed the tools necessary for the correct determination of the cloud properties using the absorption imaging technique. I established a method to obtain the calibration constants along both imaging axes by linking their respective atomic signal.

Additionally, I implemented the non-destructive phase-contrast imaging technique. This technique measures the atomic density by connecting the induced phase on the probe beam to the cloud's density. Since we work with a mixture of two distinct spin components, we can measure the density difference between both states by selecting the appropriate detuning. The optical system is suitable for performing multiple high-resolution images of the same atomic sample, allowing studying the dynamic properties of quantum gases.

Finally, to further increase the quality of the acquired density profiles, I developed an algorithm capable of removing high-frequency artifacts from the images without altering the density profile. Hence, increasing the signal-to-noise ratio a factor of two.

The diagnostic tools I developed during this work will enable the Laboratory of Ultracold Matter at UNAM to explore new and exciting phenomena.

5.2. Future perspectives

Quantum turbulence One of the main goals of the laboratory is to study fermionic superfluid turbulence in quantum gases. Only recently, there has been experimental progress in the understanding of turbulent cascades in weakly interacting bosonic superfluids [66]. It is not the case for fermionic superfluids, where there are no prior experimental attempts to study the emergence of such turbulent cascades [67]. Fermionic superfluids offer the opportunity to characterize a wide range of interaction regimes using the Feshbach resonances. This versatility is not necessarily present in bosonic superfluids due to its collapse for attractive interactions [1, 2] and three-body losses for strong interactions [1, 26].

Recent papers have tried to comprehend the transition between different collective excitation regimes to a turbulent one. One of these proposals is the unfolding of Faraday-waves-like excitations [68, 69].

Faraday waves In 1831, Faraday studied the emergence of parametric surface waves that originated from an oscillatory vertical motion [70]. Such parametric surface waves show the non-linear behavior of fluids, where the vertical motion couples to the horizontal surface generating time-dependent spatial patterns [71]. These patterns appear and disappear at half the driving frequency. This kind of parametric excitations is an example of growing instability in a non-linear system [71].

Previous experiments confirmed the emergence of Faraday waves-like patterns in cigar-shaped ultracold bosonic gases [53, 55, 72, 73]. They reveal that this phenomenon can be linked to discrete-time crystals, making the whole system behaves like a space-time crystal [55, 72]. In particular, this phenomenon allows us to study pattern formation in quantum gases. The degree of non-linearity in the system determines the emergent properties of such patterns, such as the spatial and time periodicity, growth rate, and symmetry. For these reasons, it is worth studying the emergence of Faraday waves across the BEC-BCS crossover. This work allowed us to study such collective excitations. To follow the dynamics of this type of excitation, we required to probe the sample multiple times with sufficient resolution to distinguish spatial patterns. The development of phase-contrast imaging is therefore needed.

To excite the Faraday waves, we drive the radial trapping frequency by modulating

the ODT intensity sinusoidally:

$$P(t) = P_0(1 + \alpha \sin \Omega t) \implies \omega_r(t) = \omega_{r_0} \sqrt{1 + \alpha \sin \Omega t}. \quad (5.1)$$

The driving of the trapping potential will induce a driving in the density distribution of the cloud. Due to the non-linear behavior of ultracold quantum gases, this temporal drive will couple to a variety of excitation modes of the gas, for instance the breathing mode, the scissor, and Faraday waves. The result from all the excitation modes is a spatial density modulation along the axial axis of the trapped cloud known as Faraday waves. These waves have the characteristic behavior that the spatial density modulation oscillates in time with half the driving frequency. In particular, driving the system at the breathing mode frequency will produce a resonant coupling between the breathing mode and the Faraday waves, accelerating the emergence of the density modulation.

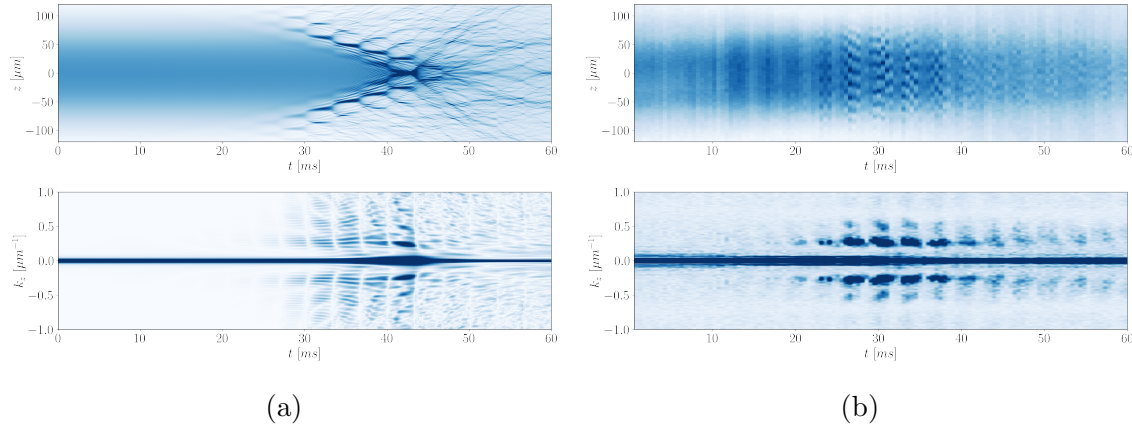


Figure 5.1: Time evolution of Faraday waves in the BEC-side of the Feshbach resonance. We present on top the axial density and the corresponding Fourier Transform for a) the result from the time evolution of the Gross-Pitaevskii equation, and b) the experimental time evolution.

Figure 5.1 show the emergence of the Faraday waves in the BEC-side of the Feshbach resonance, driving at $\Omega = \omega_{Breathing} \approx 2\omega_r$. Figure 5.1a results from the numerical simulation of the Gross-Pitaevskii equation (GPE), while 5.1b is the experimental realization. The GPE equation is a non-linear Schrödinger equation:

$$i\hbar \frac{\partial \psi}{\partial t} = -\frac{\hbar^2}{2M} \nabla^2 \psi + V(\mathbf{x}, t) \psi + g_M |\psi|^2 \psi, \quad (5.2)$$

where ψ represents the molecular pair wavefunction in the BEC-side, the mass being $M = 2m_{Li}$, the time dependent potential $V(\mathbf{x}, t) = \frac{1}{2}M(\omega_z^2 z^2 + \omega_r^2(t)r^2)$, and $g_M = 4\pi\hbar^2 a_M/M$ is the interaction constant depending on the molecular scattering length $a_M \approx 0.6a_s$ with a_s the atomic scattering length.

Since the time dependence of the potential is periodic, it is possible to get an insight into the solution to the GPE without solving it. This is possible using Floquet and linear stability analysis. Using both tools to analyze the GPE with the radial driving, we arrive at a Mathieu-like equation for the equilibrium solution perturbations. The Mathieu equation is given by:

$$\frac{\partial^2 u(\tau)}{\partial \tau^2} + (a - 2q \cos 2\tau)u(\tau) = 0. \quad (5.3)$$

This result enables us to predict the wavevector of the spatial modulation as a function of the driving frequency and the interaction regime, meaning $k_{FW}(1/k_F a_s, \Omega)$. The solution to the Mathieu equation gives a rich stability diagram showing the unstable regions in a parameter-space. A useful parameter-space is formed by the axial wavevector, k_z , and the driving amplitude α . The particular interest in this parameter space is that it is accessible experimentally. Preliminary results from our Faraday waves experiments are shown in figure 5.2a.

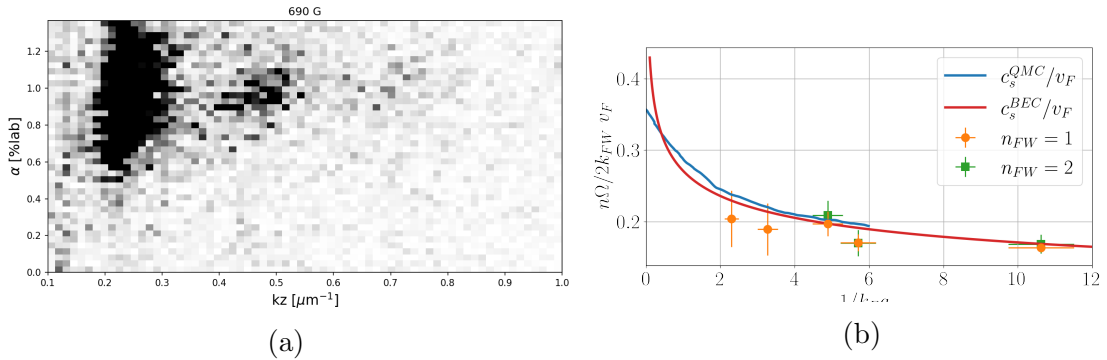


Figure 5.2: a) Experimental stability diagram of Faraday waves on the BEC-side. b) Faraday waves phase velocity compared to the speed of sound in the quantum gas.

The darker areas in figure 5.2a show the unstable regions obtained experimentally. These regions are associated with the Mathieu equation solutions in the already mentioned parameter-space.

The Faraday waves excitation can be interpreted as the interference of two counter-propagating phonons with the same wavevector. This interpretation leads to the

conclusion that the phase velocity of the Faraday waves, $\Omega n/k_{FW}$, can be linked to the speed of sound in the quantum gas. Particularly on the BEC-side, this relation is given by:

$$\left(\frac{1}{v_{Fermi}} \frac{\Omega n}{k_{FW}} \right) \approx 2 \frac{c_s^0}{v_{Fermi}}. \quad (5.4)$$

Figure 5.2b shows preliminary results on the speed of sound measurement using the Faraday waves in the BEC-side.

Further analysis and experiments must be carried out to uncover the connection between Faraday waves and quantum turbulence across the whole BEC-BCS crossover.

Appendix A

${}^6\text{Li}$ D-lines properties

The properties of the D₁ and D₂ lines of ${}^6\text{Li}$ are:

Property	Symbol	Value
Wavelength (vacuum)	λ	670.992421 nm
Wavenumber (vacuum)	$k/2\pi$	14903.298 cm ⁻¹
Frequency	ν	446.289634 THz
Lifetime	τ	27.102 ns
Natural Linewidth	Γ	5.8724 MHz
Saturation intensity	I_{sat}	7.59 mW/cm
Recoil velocity	v_{rec}	9.886554 cm/s
Recoil temperature	T_{rec}	3.53565356 μK

Table A.1: Optical properties of the D₁ line [28].

Property	Symbol	Value
Wavelength (vacuum)	λ	670.977338 nm
Wavenumber (vacuum)	$k/2\pi$	14903.633 cm ⁻¹
Frequency	ν	446.799677 THz
Lifetime	τ	27.102 ns
Natural Linewidth	Γ	5.8724 MHz
Saturation intensity	I_{sat}	2.54 mW/cm
Recoil velocity	v_{rec}	9.886776 cm/s
Recoil temperature	T_{rec}	3.53581152 μK

Table A.2: Optical properties of the D₂ line [28].

Bibliography

- [1] W. Ketterle and M. W. Zwierlein. “Making, probing and understanding ultracold Fermi gases”. In: *Nuovo Cimento Rivista Serie* 31.5-6 (May 2008), pp. 247–422. DOI: 10.1393/ncr/i2008-10033-1. arXiv: 0801.2500 [cond-mat.other].
- [2] W. Ketterle, D. S. Durfee, and D. M. Stamper-Kurn. “Making, probing and understanding Bose-Einstein condensates”. In: *arXiv e-prints*, cond-mat/9904034 (Apr. 1999), cond-mat/9904034. arXiv: cond-mat/9904034 [cond-mat].
- [3] Stefano Giorgini, Lev P. Pitaevskii, and Sandro Stringari. “Theory of ultracold atomic Fermi gases”. In: *Reviews of Modern Physics* 80.4 (Oct. 2008), pp. 1215–1274. DOI: 10.1103/revmodphys.80.1215. URL: <https://doi.org/10.1103/revmodphys.80.1215>.
- [4] M. R. Andrews et al. “Direct, Nondestructive Observation of a Bose Condensate”. In: *Science* 273.5271 (July 1996), pp. 84–87. DOI: 10.1126/science.273.5271.84. URL: <https://doi.org/10.1126/science.273.5271.84>.
- [5] C. C. Bradley, C. A. Sackett, and R. G. Hulet. “Bose-Einstein Condensation of Lithium: Observation of Limited Condensate Number”. In: *Physical Review Letters* 78.6 (Feb. 1997), pp. 985–989. DOI: 10.1103/physrevlett.78.985. URL: <https://doi.org/10.1103/physrevlett.78.985>.
- [6] R. Meppelink et al. “Thermodynamics of Bose-Einstein-condensed clouds using phase-contrast imaging”. In: *Physical Review A* 81.5 (May 2010). DOI: 10.1103/physreva.81.053632. URL: <https://doi.org/10.1103/physreva.81.053632>.
- [7] G. Reinaudi et al. “Strong saturation absorption imaging of dense clouds of ultracold atoms”. In: *Optics Letters* 32.21 (Oct. 2007), p. 3143. DOI: 10.1364/ol.32.003143. URL: <https://doi.org/10.1364/ol.32.003143>.

- [8] Munekazu Horikoshi et al. “Appropriate Probe Condition for Absorption Imaging of Ultracold 6 Li Atoms”. In: *Journal of the Physical Society of Japan* 86.10 (Oct. 2017), p. 104301. DOI: 10.7566/jpsj.86.104301. URL: <https://doi.org/10.7566/jpsj.86.104301>.
- [9] Miroslav Gajdacz et al. “Non-destructive Faraday imaging of dynamically controlled ultracold atoms”. In: *Review of Scientific Instruments* 84.8 (Aug. 2013), p. 083105. DOI: 10.1063/1.4818913. URL: <https://doi.org/10.1063/1.4818913>.
- [10] J. Smits, A. P. Mosk, and P. van der Straten. “Imaging trapped quantum gases by off-axis holography”. In: *Optics Letters* 45.4 (Feb. 2020), p. 981. DOI: 10.1364/ol.384120. URL: <https://doi.org/10.1364/ol.384120>.
- [11] Joon Hyun Kim, Deokhwa Hong, and Y. Shin. “Observation of two sound modes in a binary superfluid gas”. In: *Physical Review A* 101.6 (June 2020). DOI: 10.1103/physreva.101.061601. URL: <https://doi.org/10.1103/physreva.101.061601>.
- [12] M. R. Andrews et al. “Propagation of Sound in a Bose-Einstein Condensate”. In: *Physical Review Letters* 79.4 (July 1997), pp. 553–556. DOI: 10.1103/physrevlett.79.553. URL: <https://doi.org/10.1103/physrevlett.79.553>.
- [13] R. Meppelink, S. B. Koller, and P. van der Straten. “Sound propagation in a Bose-Einstein condensate at finite temperatures”. In: *Physical Review A* 80.4 (Oct. 2009). DOI: 10.1103/physreva.80.043605. URL: <https://doi.org/10.1103/physreva.80.043605>.
- [14] P. B. Wigley et al. “Non-destructive shadowgraph imaging of ultra-cold atoms”. In: *Optics Letters* 41.20 (Oct. 2016), p. 4795. DOI: 10.1364/ol.41.004795. URL: <https://doi.org/10.1364/ol.41.004795>.
- [15] Anand Ramanathan et al. “Partial-transfer absorption imaging: A versatile technique for optimal imaging of ultracold gases”. In: *Review of Scientific Instruments* 83.8 (Aug. 2012), p. 083119. DOI: 10.1063/1.4747163. URL: <https://doi.org/10.1063/1.4747163>.

- [16] Erin Marshall Seroka et al. “Repeated measurements with minimally destructive partial-transfer absorption imaging”. In: *Optics Express* 27.25 (Dec. 2019), p. 36611. DOI: 10.1364/oe.27.036611. URL: <https://doi.org/10.1364/oe.27.036611>.
- [17] D. Hernandez-Rajkov et al. “Experimental setup for the production of ultracold strongly correlated fermionic superfluids of 6 Li”. In: *Revista Mexicana de Física* 66.4 Jul-Aug (July 2020), p. 388. DOI: 10.31349/revmexfis.66.388. URL: <https://doi.org/10.31349/revmexfis.66.388>.
- [18] C. H. Schunck et al. “Feshbach resonances in fermionic Li 6”. In: *Physical Review A* 71.4 (Apr. 2005). DOI: 10.1103/physreva.71.045601. URL: <https://doi.org/10.1103/physreva.71.045601>.
- [19] G. Valtolina et al. “Josephson effect in fermionic superfluids across the BEC-BCS crossover”. In: *Science* 350.6267 (Dec. 2015), pp. 1505–1508. DOI: 10.1126/science.aac9725. URL: <https://doi.org/10.1126/science.aac9725>.
- [20] K Khani et al. “Dynamical phase diagram of ultracold Josephson junctions”. In: *New Journal of Physics* 22.12 (Dec. 2020), p. 123006. DOI: 10.1088/1367-2630/abc8e4. URL: <https://doi.org/10.1088/1367-2630/abc8e4>.
- [21] W. J. Kwon et al. “Strongly correlated superfluid order parameters from dc Josephson supercurrents”. In: *Science* 369.6499 (July 2020), pp. 84–88. DOI: 10.1126/science.aaz2463. URL: <https://doi.org/10.1126/science.aaz2463>.
- [22] H. Smith C. J. Pethick. *Bose-Einstein Condensation in Dilute Gases*. 2008.
- [23] B. DeMarco et al. “Measurement of p-Wave Threshold Law Using Evaporatively Cooled Fermionic Atoms”. In: *Physical Review Letters* 82.21 (May 1999), pp. 4208–4211. DOI: 10.1103/physrevlett.82.4208. URL: <https://doi.org/10.1103/physrevlett.82.4208>.
- [24] Cheng Chin et al. “Feshbach resonances in ultracold gases”. In: *Reviews of Modern Physics* 82.2 (Apr. 2010), pp. 1225–1286. DOI: 10.1103/revmodphys.82.1225. URL: <https://doi.org/10.1103/revmodphys.82.1225>.
- [25] R.A. Duine and H.T.C. Stoof. “Atom-molecule coherence in Bose gases”. In: *Physics Reports* 396.3 (June 2004), pp. 115–195. DOI: 10.1016/j.physrep.2004.03.003. URL: <https://doi.org/10.1016/j.physrep.2004.03.003>.

- [26] Wilhelm Zwerger, ed. *The BCS-BEC Crossover and the Unitary Fermi Gas*. Springer Berlin Heidelberg, 2012. DOI: 10.1007/978-3-642-21978-8. URL: <https://doi.org/10.1007/978-3-642-21978-8>.
- [27] C. A. R. Sá de Melo, Mohit Randeria, and Jan R. Engelbrecht. “Crossover from BCS to Bose superconductivity: Transition temperature and time-dependent Ginzburg-Landau theory”. In: *Physical Review Letters* 71.19 (Nov. 1993), pp. 3202–3205. DOI: 10.1103/physrevlett.71.3202. URL: <https://doi.org/10.1103/physrevlett.71.3202>.
- [28] Michael E. Gehm. “Preparation of an Optically-Trapped Degenerate Fermi Gas of 6 Li: Finding the Route to Degeneracy.” PhD thesis. Duke University, 2003.
- [29] C.J.Foot. *Atomic Physics*. Oxford master series, 2005.
- [30] Peter van der Straten Harold J. Metcalf. *Laser cooling and trapping*. Springer, 1999.
- [31] E. Ibarra García Padilla. *Diseño de los sistemas de ultra-alto vacío y de control para experimentos con gases ultrafríos de Litio*. Bachelor thesis at Facultad de Ciencias, UNAM. 2016.
- [32] J. E. Carro Martinez. *Diseño y proyección de trampas magnéticas y ópticas para experimentos con gases ultrafríos de Litio*. Bachelor thesis at Facultad de Ciencias, UNAM. 2016.
- [33] D. Hernández Rajkov. *Enfriamiento Doppler y sub-Doppler de un gas atómico de 6 Li*. Bachelor thesis at Facultad de Ciencias, UNAM. 2018.
- [34] E. Padilla. “Time-averaged optical potentials for trapping and manipulating ultracold quantum ^6Li gases”. MA thesis. Instituto de Física, UNAM, 2020.
- [35] Richard Roy et al. “Rapid cooling to quantum degeneracy in dynamically shaped atom traps”. In: *Physical Review A* 93.4 (Apr. 2016). DOI: 10.1103/physreva.93.043403. URL: <https://doi.org/10.1103/physreva.93.043403>.
- [36] Joseph Goodman. *Introduction to Fourier Optics*. Roberts and Company Publishers, 2004. ISBN: 0974707724. URL: <https://www.xarg.org/ref/a/0974707724/>.
- [37] Andrea Morales. “High resolution imaging and production of thin barriers for ultracold 6 Li Fermi gases”. PhD thesis. Sapienza Università di Roma, 2013.

- [38] *User's guide to: Andor Technology SDK*.
- [39] A. Burchianti et al. "Efficient all-optical production of Li 6 quantum gases D1 gray-molasses cooling". In: *Physical Review A* 90.4 (Oct. 2014). DOI: 10.1103/physreva.90.043408. URL: <https://doi.org/10.1103/physreva.90.043408>.
- [40] Manuel Gerken. "Gray Molasses Cooling of Lithium-6 Towards a Degenerate Fermi Gas". MA thesis. University of Heidelberg, 2016.
- [41] Rudolf Grimm, Matthias Weidemüller, and Yurii B. Ovchinnikov. "Optical Dipole Traps for Neutral Atoms". In: *Advances in Atomic Molecular and Optical Physics* 42 (Jan. 2000), pp. 95–170. DOI: 10.1016/S1049-250X(08)60186-X. arXiv: physics/9902072 [physics.atom-ph].
- [42] Claude Cohen-Tannoudji, Jacques Dupont-Roc, and Gilbert Grynberg. *Atom-photon interactions: basic processes and applications*. eng. New York: Wiley, 1992. ISBN: 9780471625568 9780471293361.
- [43] Gael Reinaudi. "Manipulation et refroidissement par évaporation forcée d'ensembles atomiques ultra-froids pour la production d'un jet intense dans le régime de dégénérescence quantique : vers l'obtention d'un laser à atomes continu". PhD thesis. Université de Paris 6, 2008.
- [44] Carmelo Mordini. "Measurement of the density profile of quantized vortices and of the equation of state in a 3D interacting Bose gas". PhD thesis. 2019.
- [45] Maurus Hans et al. "High signal to noise absorption imaging of alkali atoms at moderate magnetic fields". In: *Review of Scientific Instruments* 92.2 (Feb. 2021), p. 023203. DOI: 10.1063/5.0040677. URL: <https://doi.org/10.1063/5.0040677>.
- [46] Max Langer et al. "Quantitative comparison of direct phase retrieval algorithms in in-line phase tomography". In: *Medical Physics* 35.10 (Sept. 2008), pp. 4556–4566. DOI: 10.1118/1.2975224. URL: <https://doi.org/10.1118/1.2975224>.
- [47] C. F. Ockeloen et al. "Detection of small atom numbers through image processing". In: *Physical Review A* 82.6 (Dec. 2010). DOI: 10.1103/physreva.82.061606. URL: <https://doi.org/10.1103/physreva.82.061606>.
- [48] Linxiao Niu et al. "Optimized fringe removal algorithm for absorption images". In: *Applied Physics Letters* 113.14 (Oct. 2018), p. 144103. DOI: 10.1063/1.5040669. URL: <https://doi.org/10.1063/1.5040669>.

- [49] Xiaolin Li et al. “Reduction of interference fringes in absorption imaging of cold atom cloud using eigenface method”. In: *Chin. Opt. Lett.* 5.3 (2007), pp. 128–130. URL: <http://col.osa.org/abstract.cfm?URI=col-5-3-128>.
- [50] Jochen Kronjager. “Coherent Dynamics of Spinor Bose-Einstein Condensates”. PhD thesis. Departments Physik, Universitat Hamburg, 2007.
- [51] M. R. Matthews et al. “Vortices in a Bose-Einstein Condensate”. In: *Physical Review Letters* 83.13 (Sept. 1999), pp. 2498–2501. DOI: 10.1103/physrevlett.83.2498. URL: <https://doi.org/10.1103/physrevlett.83.2498>.
- [52] Paul C. Haljan. “Vortices in a Bose-Einstein Condensate”. PhD thesis. University of Alberta, 1997.
- [53] J. Smits et al. “Observation of a Space-Time Crystal in a Superfluid Quantum Gas”. In: *Physical Review Letters* 121.18 (Oct. 2018). DOI: 10.1103/physrevlett.121.185301. URL: <https://doi.org/10.1103/physrevlett.121.185301>.
- [54] L. Liao et al. “Dynamics of a space-time crystal in an atomic Bose-Einstein condensate”. In: *Physical Review A* 99.1 (Jan. 2019). DOI: 10.1103/physreva.99.013625. URL: <https://doi.org/10.1103/physreva.99.013625>.
- [55] J Smits, H T C Stoof, and P van der Straten. “On the long-term stability of space-time crystals”. In: *New Journal of Physics* 22.10 (Oct. 2020), p. 105001. DOI: 10.1088/1367-2630/abbae9. URL: <https://doi.org/10.1088/1367-2630/abbae9>.
- [56] Robert Meppelink. “Hydrodynamic Excitations in a Bose-Einstein Condensate”. PhD thesis. Universiteit Utrecht, 2009.
- [57] Guthrie B. Partridge et al. “Pairing and Phase Separation in a Polarized Fermi Gas”. In: *Science* 311.5760 (Jan. 2006), pp. 503–505. DOI: 10.1126/science.1122876. URL: <https://doi.org/10.1126/science.1122876>.
- [58] Y. Shin et al. “Observation of Phase Separation in a Strongly Interacting Imbalanced Fermi Gas”. In: *Physical Review Letters* 97.3 (July 2006). DOI: 10.1103/physrevlett.97.030401. URL: <https://doi.org/10.1103/physrevlett.97.030401>.
- [59] Melissa C. Revelle et al. “1D to 3D Crossover of a Spin-Imbalanced Fermi Gas”. In: *Physical Review Letters* 117.23 (Nov. 2016). DOI: 10.1103/physrevlett.117.235301. URL: <https://doi.org/10.1103/physrevlett.117.235301>.

- [60] Yong il Shin et al. “Phase diagram of a two-component Fermi gas with resonant interactions”. In: *Nature* 451.7179 (Feb. 2008), pp. 689–693. DOI: 10.1038/nature06473. URL: <https://doi.org/10.1038/nature06473>.
- [61] C. H. Schunck et al. “Pairing Without Superfluidity: The Ground State of an Imbalanced Fermi Mixture”. In: *Science* 316.5826 (May 2007), pp. 867–870. DOI: 10.1126/science.1140749. URL: <https://doi.org/10.1126/science.1140749>.
- [62] F. Zernike. “Phase contrast, a new method for the microscopic observation of transparent objects”. In: *Physica* 9.7 (July 1942), pp. 686–698. DOI: 10.1016/s0031-8914(42)80035-x. URL: [https://doi.org/10.1016/s0031-8914\(42\)80035-x](https://doi.org/10.1016/s0031-8914(42)80035-x).
- [63] G. Nienhuis, P. van der Straten, and S-Q. Shang. “Operator description of laser cooling below the Doppler limit”. In: *Physical Review A* 44.1 (July 1991), pp. 462–474. DOI: 10.1103/physreva.44.462. URL: <https://doi.org/10.1103/physreva.44.462>.
- [64] John David Jackson. *Classical Electrodynamics Third Edition*. Wiley, 1998. ISBN: 9780471309321. URL: <https://www.xarg.org/ref/a/047130932X/>.
- [65] Olivier Morice, Yvan Castin, and Jean Dalibard. “Refractive index of a dilute Bose gas”. In: *Physical Review A* 51.5 (May 1995), pp. 3896–3901. DOI: 10.1103/physreva.51.3896. URL: <https://doi.org/10.1103/physreva.51.3896>.
- [66] Nir Navon et al. “Emergence of a turbulent cascade in a quantum gas”. In: 539.7627 (Nov. 2016), pp. 72–75. DOI: 10.1038/nature20114. URL: <https://doi.org/10.1038/nature20114>.
- [67] L. Madeira et al. “Quantum turbulence in Bose–Einstein condensates: Present status and new challenges ahead”. In: *AVS Quantum Science* 2.3 (Oct. 2020), p. 035901. DOI: 10.1116/5.0016751. URL: <https://doi.org/10.1116/5.0016751>.
- [68] Kasumi Okazaki, Junsik Han, and Makoto Tsubota. “Faraday waves in Bose–Einstein condensate: From instability to nonlinear dynamics”. In: *arXiv e-prints*, arXiv:2012.02391 (Dec. 2020), arXiv:2012.02391. arXiv: 2012.02391 [cond-mat.quant-gas].

- [69] J. H. V. Nguyen et al. “Parametric Excitation of a Bose-Einstein Condensate: From Faraday Waves to Granulation”. In: *Phys. Rev. X* 9 (1 2019), p. 011052. DOI: 10.1103/PhysRevX.9.011052. URL: <https://link.aps.org/doi/10.1103/PhysRevX.9.011052>.
- [70] M. Faraday. “XVII. On a peculiar class of acoustical figures and on certain forms assumed by groups of particles upon vibrating elastic surfaces”. In: *Philosophical Transactions of the Royal Society of London* 121 (Dec. 1831), pp. 299–340. DOI: 10.1098/rstl.1831.0018. URL: <https://doi.org/10.1098/rstl.1831.0018>.
- [71] M. C. Cross and P. C. Hohenberg. “Pattern formation outside of equilibrium”. In: *Reviews of Modern Physics* 65.3 (July 1993), pp. 851–1112. DOI: 10.1103/revmodphys.65.851. URL: <https://doi.org/10.1103/revmodphys.65.851>.
- [72] P. Engels, C. Atherton, and M. A. Hoefer. “Observation of Faraday Waves in a Bose-Einstein Condensate”. In: *Physical Review Letters* 98.9 (Feb. 2007). DOI: 10.1103/physrevlett.98.095301. URL: <https://doi.org/10.1103/physrevlett.98.095301>.
- [73] S. E. Pollack et al. “Collective excitation of a Bose-Einstein condensate by modulation of the atomic scattering length”. In: *Physical Review A* 81.5 (May 2010). DOI: 10.1103/physreva.81.053627. URL: <https://doi.org/10.1103/physreva.81.053627>.